GEORG-AUGUST-UNIVERSITÄT GÖTTINGEN

Faculty for Physics

Institute for the Dynamics of Complex Systems

MAX PLANCK INSTITUT FOR DYNAMICS AND SELF-ORGANISATION

Master thesis

Kontrollierbare Polymerosome als Mikro-Carrier zur Beeinflussung von Wundenheilung.

Switchable polymeric microcarriers for remodeling of wound healing.

---

prepared by

Vanessa Scheller

19.12.2020, Göttingen

Contents

1. Introduction: Wound Healing and Possible Synthetic Applications

This thesis describes the work towards creating a hybrid tissue, using polymeric microcapsules produced through droplet-based microfluidics as a means to influence cells' wound closing behaviour. This further leads to the possibility of influencing scar tissue formation or even scar tissue remodelling. The importance of creating a synthetic foam becomes clear by considering the impact of accompanied morphological and phenotypical changes to the tissue and its functionality upon wounding and subsequent healing. Scarring, or fibrosis, occurs as a natural part of the wound healing process in every recovered wound to some degree. Only a small number of animals, like the planarian flatworm, starfish or salamanders, are exempt from that rule due to their ability to completely regenerate tissue by regrowing it without forming excess tissue. This scar tissue becomes a problem because of its poor mechanical properties in skeletal muscle in comparison to undamaged tissue due to a change in, for example strongly reduced excitability due to reduced gap junction density in the heart muscle, as well as collagen fibre orientation. For a typical dermal wound the resistance to ultraviolet radiation is significantly lessened and additionally, hair follicles and sweat glands fail to regrow. While the impact on dermal wounds is still relatively small, it becomes vital when considering internal organs. Continued scarring of the liver tissue, for example, as it occurs due to many liver diseases like hepatitis, excessive alcohol consumption or some medications, can lead to liver cirrhosis. Untreated, cirrhosis takes a self-amplifying course as more scar tissue forms with further progression making it difficult for the liver to function. Another dangerous example of scar tissue is found in the heart as remnant of a myocardial infarction, or "heart attack". The infarction causes scar formation in the heart muscle and while the skeletal muscles' mechanical properties lead to a loss in muscular strength and possibly heart failure, the structural change can also alter the electrical excitation in the myocardium. As the scar tissue itself is almost unexcitable and the surrounding tissue is modified in its electrophysiological properties, the electrical excitation signal, usually a t-wave, can form a three-dimensional spiral wave instead. As such, conductivity is slowed down in this area and the duration of the action potential increased due to remodeling of ion channels. This leads to the creation of additional spiral waves that cancel each other out or induce fibrillation leading to arrhythmia and anchor around the scar area. Some arrhythmias have no symptoms, but others promote stroke, heart failure or result in sudden death. While most arrhythmias can be effectively treated this progression showcases just how significantly scarring influences tissue functionality.

This motivates the question how exactly scar tissue differs from normal tissue and what influences this transition, as one might take targeted actions to remodel wounds

or affect closing efficiency. In this work we concentrate on the role the transforming growth factor (TGF) βplays in the 3T3 fibroblast transition to myofibroblasts and the associated impact on the wound closing behaviour of the cells, and investigate carrier systems to deliver such change to the system. This two track approach allows us to focus first on the development and characterisation of a carrier system and second on the wound healing behaviour of the fibroblasts under different TGF-β conditions. As such, the more complex situation of both aspects joined is easier analysed after ensuring a controlled and separately characterised model system. For this, we develop a simple polymeric carrier system using droplet-based microfluidics on one hand, which responds to a thermal stimulus and allows for a controlled release of the cargo.
Successful implementation and characterisation of this synthetic and controllable carrier-system together with cells might open up an easy access-point for targeted manipulation of wound healing parameters in cell-culture experiments.

2. Theoretical Background

A significant feature of this work is the interplay of two major topics: synthetic microfluidics on one hand, and electric cell impedance measurements on the other. As such, there are several points that need at least a short mention in order to make sense as a whole. In the following section we will, therefore, give a brief introduction of droplet microfluidics and subsequent polymerisation mechanisms, we will briefly discuss cells' wound healing behaviour from a biochemical, as well as physical point of view and subsequently look at the underlying principles of electric cell-substrate impedance sensing (ECIS).

2.1. Fibroblasts and Wound Healing

The process of wound healing is a universal response to inflammation following injury of tissue until at least partial restoration of the injured tissue is achieved. This process consists of several consecutive partially overlapping events, including

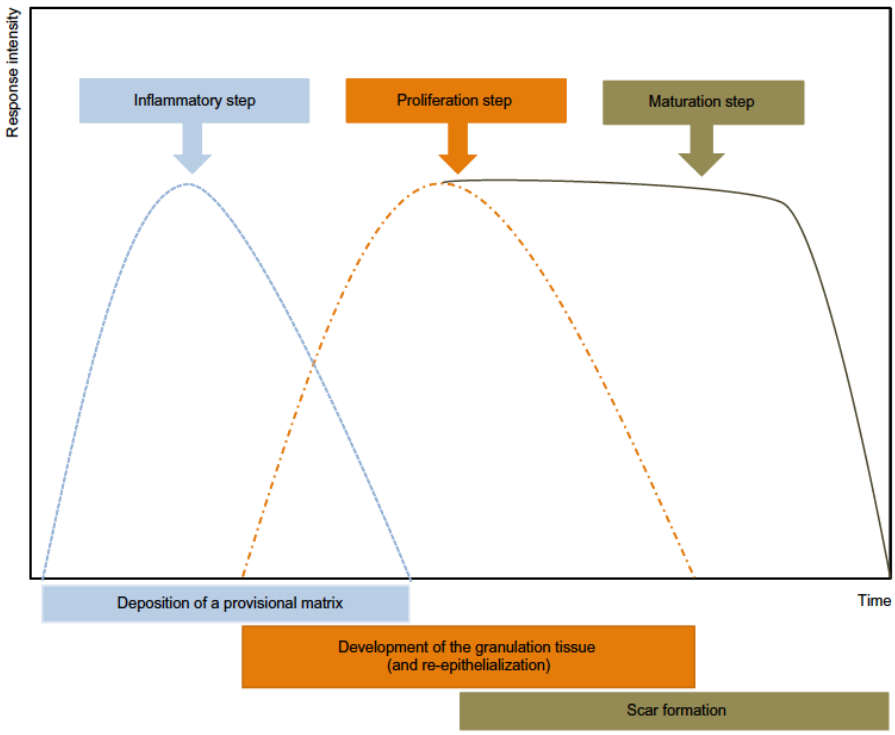

Figure 2.1.: The plot illustrates exemplary time scales over which a healing process can happen and how the distinctive phases temporally overlap and contribute. The image was adapted from [1] and [2].

cell proliferation, often activated by growth factors, migration, fibrogenesis (extracellular matrix overproduction and deposition), resolution and remodeling of the injured or scarred tissue.
Overall, one can distinguish between three interrelated and dynamic phases as shown in Figure 2.1. Firstly, the 'inflammatory phase' starts with damage of capillaries, triggering the formation of a blood clot consisting of fibrin and fibronectin [1].
This provisional matrix not only allows cells needed for the wound healing process to migrate into the wound, but also provides various chemokines released by platelets, monocytes and other cellular blood constituents. Such chemocytes like growth factors stimulate inflammatory cells, neutrophils and macrophages, but also the transformation, migration and proliferation of fibroblasts, which are considered in this thesis, to the wound site to reconstitute various connective tissue components [3]. This initiates the second, 'proliferative phase'. Macroscopically, this step can be considered as the actual start of the healing process, following as universal response to inflammation, which includes cell proliferation In-vivo, the last 'regeneration phase' includes maturation of the new tissue, as well as scar formation and re-cellularization. Shortly after wounding 'normal' fibroblasts are activated and migrate towards the fibronectin-fibrin wound interface, where they proliferate and synthesise a granulation tissue, see Figure 2.2. This connective tissue is a collagen-containing matrix, that acts as provisional wound matrix together with the corresponding transformed cells.
Around the same time wound contraction starts. Once the wound defect is replaced the fibroblast population stops dividing while in parallel extracellular matrix remodelling occurs.

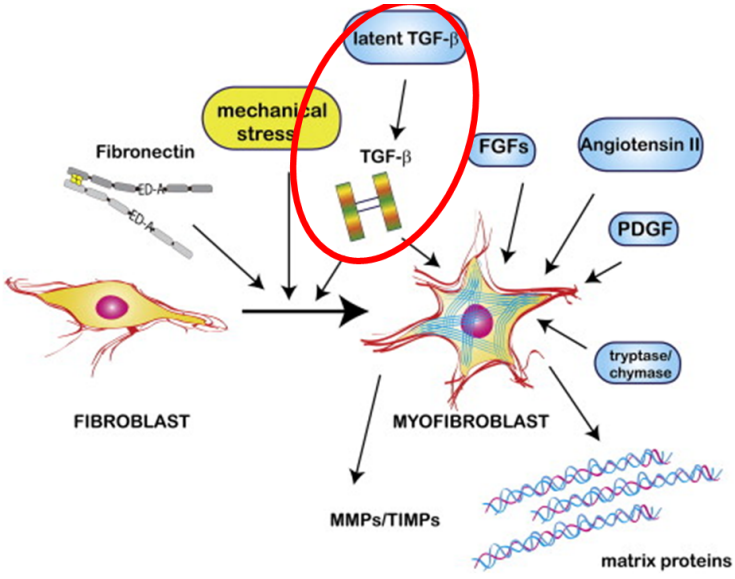

Figure 2.2.: The image shows schematically an extract of the recovery of cardiac fibroblasts after an infarction. During the recovery cardiac fibroblasts are transitioned to cardiac myofibroblasts to supply important ECM proteins or migrate into the wounded area. Several important molecules are denoted, but most significantly for this work is the contribution of TGF-β [4].

This process is highly complex and, therefore, difficult to break down, for example as it involves different mechanotransducers and signaling mechnisms. Here, we will focus on an in-vitro model approach containing components of especially phase one and two, during which fibroblasts are activated and proliferate and develop a first cell layer similar to new connective tissue.

2.1.1. Cell movement and adhesion

Cell movement is a complex process of several components and plays a critical role in various physiological and pathological processes like immune respones, outgrowth and metastasis of cancer cells and wound healing. Of course, there are different ways in which cells can move, like swimming by using flagella, but crawling is the common way of locomotion for most motile eukaryotic cells. To close a wound cells migrate into the open area, relying on the different ways in which a cell can move and the underlying dynamics of the actin network which is the primary driving force for this phenomenon [5]. Three main contributions to cell movement can be identified:
1) protrusion of the leading edge of the cell and attachement of the leading edge,
2) cytoskeletal contraction pulling the cell forward and
3) detachment of the back and cell body.
The existence of a leading edge further implies directional movement for which a cell needs to continuously receive and process signals portraying environmental conditions via signalling cascades in intracellular processes, translating them into cell polarisation and subsequently a directional protrusion. Two typical cell propulsions can be described:
A *lamellipodium*,which is a thin plate of cytoplasm extending across the substrate and is produced and supported by a quasi-two dimensional actin mesh. The formation of lamellipodia is controlled by Rac, a member of the Rho family small G protein.

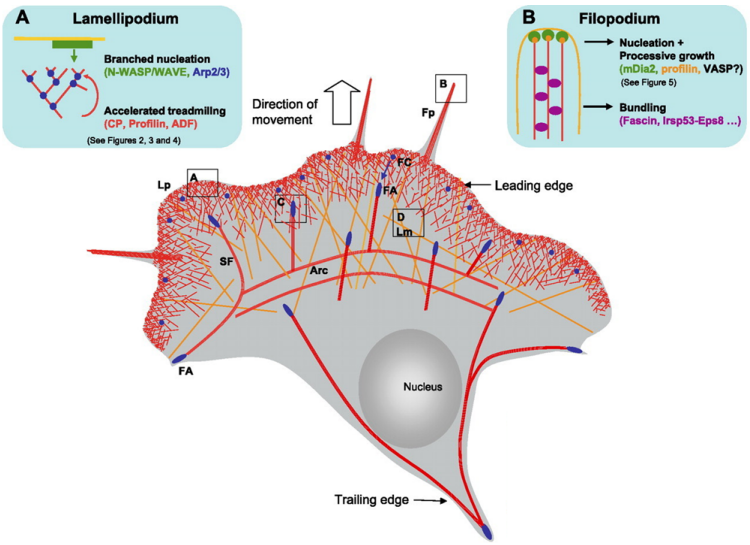

Figure 2.3.: The image shows a schematic of a migrating cell with lamellipodia and filopodia protrusions. The actin cytoskeleton is visualised in red. Image adapted from [6].

From these lamellipodia several small microspikes, or *filopodia*, extend beyond the protruding edge in order to sense chemotactic as well as mechanical cues.

Transforming growth factor β

Transforming growth factor (TGF) β is actually a large family of TGF proteins synthesised in a variety of tissues. It is a multifunctional peptide with a potential role in embryonal development, cellular differentiation, hormone secretion and immune function as wound healing [7]. Especially noteworthy is the often synergistic reaction with TGF-α inducing a transformation of cells. TGF-β is important for fibroblasts during wound healing in their transition to myofibroblasts and it was shown to significantly enhance their ability to contract a collagen matrix citeMontesano1988. Due to this stimulated contraction of a provisional ECM matrix, TGF-beta is suggested to accelerate wound healing when released in the proximity of the injury. The TGF-β family can be split into several subgroups but the most frequently studied peptides of this family are TGF-β1, TGF-β2 and TGF-β3 that all function through the same receptor signalling system. We will only consider TGF-β1, and the influence of its concentration on fibroblast transformation to myofibroblasts during wound healing. TGF-β has shown to have many influences on inflammatory cells and fibroblasts, like the increased production of collagen and fibronectin, both main constituents of the ECM, but also an enhanced contractility on a collagen matrix. On the other hand, there were also contradictory assessments on how TGF-β might also act as a key determinant of carcinoma cell behaviour in a way, where its signalling pathway can act as a tumor suppressor and promoter of tumor progression and invasion. As such, there are many contributions and factors to consider and judging from the range molecules involved it would be difficult to study them independently. Therefore, we will concentrate in this work on the overall influence of TGF-β on wound closing dynamics and tissue properties of the cells that repopulated the gap. This might not explain how TGF-β exactly influences fibroblasts during wound closure in-vivo, but serve as an in-vitro minimalistic model explaining the question of how TGF-β influences wound healing efficiency and thus dynamics.

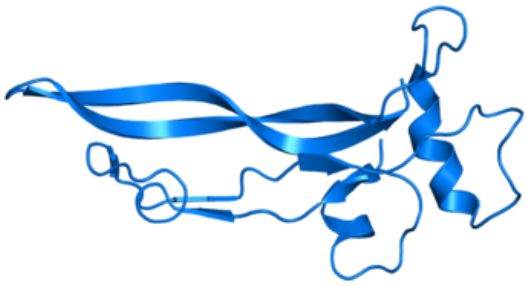

Figure 2.4.: The image shows a single molecule chain of the transforming growth factor β, as recorded by the Protein Data Bank in Europe Knowledge Base [8].

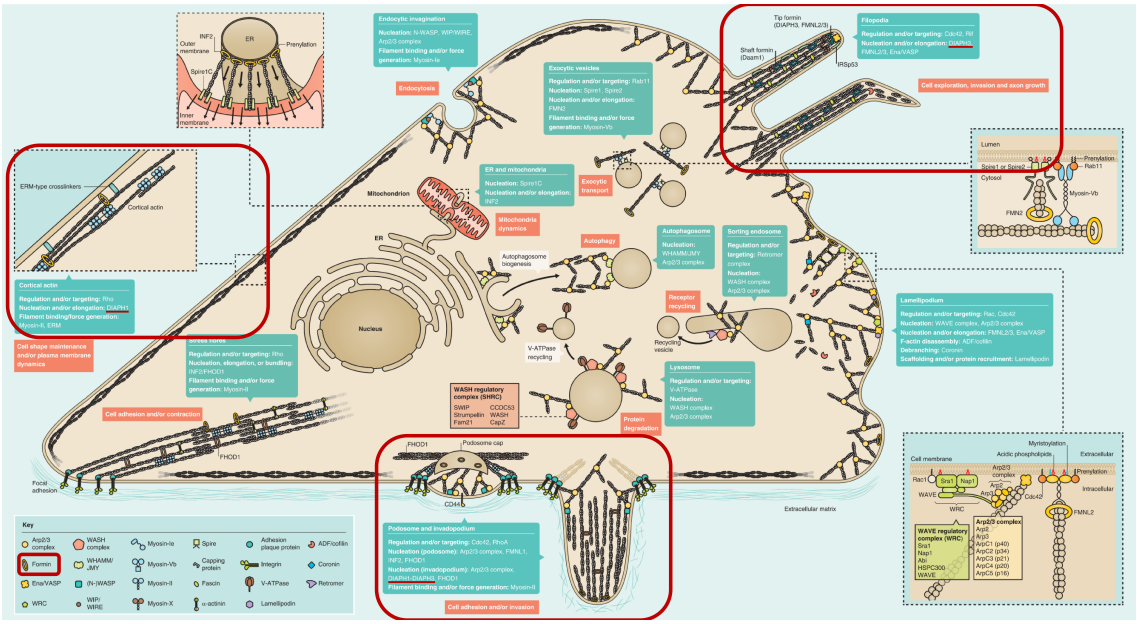

Figure 2.5.: The schematic gives a comprehensive summery over actin assembly mechanisms and the involved biomolecules. Further, the mechanisms are highlighted (red) for which mDia-related formin 1 and three play a significant role: in cortical actin nucleation (mDia1) to maintain cell shape and/or membrane dynamics, in filopodia formation (mDia3) for environmental exploration and both mDia1 and -3 formins for cell adhesion and invasion trough invadopodia formation. Reprinted and modified with permission from [9].

Formins

On another note, we also study the influence of different formins on wound closure using ECIS method. Formins are a family of cellular proteins that are part of many cellular processes by regulating the cytoskeleton, but also actin nucleation, cytokinesis and especially the formation of parallel actin bundles in filopodia during cell migration or in contractile uropods. Especially the dynamics of cell migration are interesting for this thesis as it directly influences wound closing efficiency. In this context genetically modified 3T3-fibroblasts were studied in which either the gene to produce mDia1 or mDia3 was inhibited or a double knock out mutant with both mDia1 and mDia3 inhibited. Filopodia are dynamic structures made up mostly of actin filaments mDia1 has been found to be the key formin driving filopodial protrusion. This might be especially relevant in the context of analysing what method of movement is mainly used to close a wound and possibly identify varying wound closure dynamics.
Figure 2.5 shows a comprehensive summary over actin assembly mechanisms in a cell [9] and with mDia-related formin 1 and 3 highlighted (red), the importance of these formins as actin nucleators for a cells interaction with and response to the environment becomes apparent. As such, both formins mDia1 and -3 are essential for actin nucleation for invadopodia formation, while mDia1 is vital for cortical actin nucleation and elongation targeting Rho in order to maintain and regulate cortical

tension and membrane dynamics, thus maintaining cell shape.
MDia3 on the other hand has been shown to be important for actin nucleation and elongation in filopodia targeting the cell division control protein Cdc42 and Rif GTPase, though Rif mainly in the brain. This makes mDia formin 3 especially relevant for cell exploration and invasion and thus the response of a cell to environmental cues and directed cell movement.

2.1.2. Wound Healing Assays

Wound healing behaviour is a very broad and heavily studied topic. Naturally, speeding up a healing process or positively influencing scar tissue formation is a desirable aspiration, not only in the obvious benefit for wound closure itself but just as much in far-reaching positive consequences for many serious diseases. It has been shown that wound closure is strongly dependent on wound shape, size and a pressure on cells adjacent to the wound exerted by the remaining cell body [10]. Therefore, it is desirable to have a material which acts as synthetic scaffold inside the wounded area and realising this in the form of a carrier system enables one in addition to controllably add a cytokine to the system to influence cell behaviour. But in order to study the behaviour of cells during wound closure, first of all, one needs a wound. There are many different methods used to create model wounds but in general one can distinguish between two major categories: 1) wounds due to cell death and 2) "wounds" without cell death. While open surfaces inside a cell monolayer created without the destruction of cells, but rather an excluding barrier or coating, are not actual wounds, they are considered "model wounds" in many studies.
The destruction of a monolayer, and therefore manifold cell death, leads to a complex signalling cascade involving adjacent cells while presenting a traumatic stress for surviving border cells. Even not considering apoptotic signalling, this situation still presents a variety of different factors that interplay and affect the healing process to a greater or lesser extent. Upon wounding, these removed cells release their content into the culture medium and while that is typically exchanged hereupon, it can not be definitely said how much debris and cell content remains. Additionally, a sudden medium influx may occur for border cells as they may become partially permeable due to the violent tearing off of adhesive junctions [11]. Due to these unclear dynamics, efforts were made to study wound healing behaviour uncoupled from apoptotic influences like cell damage and permeabilisation by using barrier assays, excluding the confusing element of death. While they were shown to provide valuable "model wounds", especially for geometry dependent migration studies, the significance for in vivo wound healing behaviour of conclusions drawn from barrier experiments are controversial.
In the following section we will introduce some of the most important in vitro wound healing assays to better put the ECIS method, that we used, into context. Another distinction one can make is the dimensionality. Normally one studies a two dimension cell monolayer, as is the case for all methods introduced hereinafter. Nonetheless, in vivo wound healing is not a two dimensional process, but rather characterised by three dimensional cell migration in all directions [12]. Cells in a

three dimensional matrix environment exhibit not only a different morphology, but also different signalling and migration behaviours as well as metabolic functions [13] As such, there are several ways to implement a three dimensional wounding assay, typically by seeding cells either on top of or together with some scaffold material, or adapting models for dermatological testing have for wound healing studies [14]. Most of these models however represent dermal wound structures and are typically constructed of a bilayer combining dermal and epidermal components. The scaffold of the dermis combined with fibroblasts can be reconstructed with hydrogels like collagen, glycosaminoglycans, but also synthetic polymers, above which an epidermis-like cell layer is cultured [12]. Such models are another example of the importance of the planned polymerosomes' possible function as scaffold, albeit for a different application.
Generally, wound healing assays follow a common general procedure in their deliberate destruction or prevention of a confluent monolayer:

1) **Cell injury.** This is either done literally or by the removal of a barrier, to obtain a cell free surface.
2) **Data acquisition.** The healing process is monitored for the duration of the wound closure and corresponding data collected by microscope, impedance, etc. measurements.
3) **Data evaluation.** Finally, the collected data is evaluated and interpreted.

In the following part, we will introduce individual methods more specifically.

Scratch assay

The scratch assay is the most established wound healing assay, due to its easy to use and applicability to widely available culture conditions and equipment. For this, a confluent monolayer is scratched with a sharp object varying from special cell scrapers, metallic microindenters over pipette tips to toothpicks, and the subsequent healing process imaged as micrograph data. While automation of scratching supposed to provide better reproducibility and with that comparability, and higher throughput, the main problem of the scratch assay becomes apparent in its irregularity. Even when using the same scratching tool, scratches may vary in size, shape and applied scratching velocity and pressure, which even vary for a single scratch. This further affects the remaining coating, or the amount remaining, as a scratch in most cases destroys the absorbed proteins and ECM at the basal cell level. Additionally, destroyed cells may accumulate on the edge of the scratch, which might influence cells' proliferation and migration and even impede data analysis [12]. These considerations show, that while the scratch assay is a well established simple tool for wound healing studies, it does not provide a controlled environment, neither of the remaining border cells, nor of possible ECM-remains or substrate composition of the cell-free surface.

Stamping

As the name suggests, a stamp, typically a rubber or polydimethylsiloxane (PDMS) mold that can take any shape is pressed on a monolayer, either manually or automated, destroying the cells between surface and stamp. In contrast to the rough proportions of a scratched wound, the stamp applies pressure to a well defined area, of any shape

the stamp can take. This way the debris can either be removed by shifting the stamp laterally, or stay in the wounded area in order to monitor the influence of debris on migration. With this treatment, the ECM developed by the cells previously occupying the wounded area, stays intact and, therefore, presents a more realistic healing environment. The reproducibility of this assay, however, varies strongly with the degree of automation of the process. Regular smaller patterns are easily produced with especially molded stamps, ensuring a high throughput, but if the stamp is manually applied to the cell layer, there are irregularities in the applied pressure lowering comparability between experiments. Often, stamping is combined with a heat stimulus to study differences between thermo-mechanical and mechanical damage, as many wounds result from a combination of these parameters. Such experiments show a low reproducibility as well, as there is no account for possible heat transfer to cells beyond the wounded area [12].

Electrical wounding

While the scratch assay and stamping destroy cells mechanically, ECIS assays employ an electrical approach. A high voltage pulse is applied to a well defined, restricted area, electroporating and heating the cells strongly and thereby, killing them. As mentioned for the temperature-controlled stamp, heat development may be a questionable influence on surrounding cells. During a measurement the wound condition is monitored continuously in real-time, therefore recording the healing as well as the wounding process. This way it can be ensured, that all cells covering the electrode are destroyed, even with some cell types, like fibroblasts, being more difficult to detach than others. In contrast to the previously introduced methods, ECIS measurements provide quantitative and highly reproducible measurements with good control over the substrate coating, while keeping the ECM intact [12]. On the downside, one needs specialised equipment, with lower throughput and higher cost compared to the quick and easy implementation of a scratch or stamp assay.

Barrier assay

A barrier assay provides a "model wound" without actually afflicting damage to the cell sheet. This is done by masking the surface before the cells are seeded and during monolayer growth with a mold of desired shape. Different variants of this assay include agar blocks, silicone sheets, PDMS microstencils or micropillars as barriers. Upon removal of the barrier a free surface is presented to the cells, the properties of which can be controlled but missing a previously produced ECM. This is an advantage as much as a disadvantage considering the controversial relevance for in vivo wound healing behaviour. Nevertheless, the combination of high throughput and microfabrication by photolithography provides good reproducability of initial conditions for a "model wound" and allows the uncoupled study of possible contributions to wound closure dynamics [15].

"Electric fence"

Complementary to electrical wounding, an ECIS setup allows for a barrier-type measuring mode, called the "electric fence". In this case, continuously high current pulses on the working electrode act as a barrier preventing cells from attaching or migrating to the electrode surface. This ensures on one hand, the control of the electrode surface composition up to full recovery, and on the other had, eliminates all influences of cell death like apoptotic signals [16]. As such, the "electric fence" provides a good supplementary measurement mode to electrical wounding in order to measure influences of different coatings on cell migration due to the absence of ECM in the "wounded" area.

Boyden chamber assay

Although a Boyden chamber assay is not a wound healing assay per se, it is a common tool to study cell migration and invasion due to a chemoattractant. This is accomplished by seeding cells atop a polycarbonate membrane with defined pore size inside a culture well plate together with serum-free culture medium. The "chamber" below this membrane contains a culture medium with serum and similar chemoattractants, prompting cells to migrate through the pores, which allows for them to be counted later on using, for example, a plate reader or a stained fluorescent signal [17].

2.1.3. Wound Closure Dynamics

Myofibroblasts have been found in many tissues, usually as a marker of scarring and fibrosis. What distinguishes them from normal quiescent fibroblasts are prominent microfilament bundles in their cytoplasm together with the formation of tight junctions, for cardiomyofibroblasts adherents and gap junctions, too, between neighbouring cells, something fibroblasts do not exhibit [1]. With growing evidence of myofibroblasts importance for wound closure, but at the same time their prominent role in fibrotic diseases and likely influencing tumor growth, it is important to study and understand the transition of fibroblasts to myofibroblasts and how to possibly influence it [18]. Myofibroblasts differ in their phenotype significantly from fibroblasts, as they are closer to muscle cells due to the expression of α-SM actinin in microfilament bundles or fibres. This is especially important to enhance their contractile abilities during the formation and maturation of granulation tissue.
Although this work studies the behaviour of fibroblasts, it is essential to get to know established models for wound closure dynamics. There have been several approaches to model cell wound closure, however, epithelial wound closure is perhaps the most studied model wound. One such model has been introduced and further developed by Silberzan et al.in 2007 [11]. In the following section I will give a brief introduction and overview of the basic theory and assumption in order to create a basis for comparison to later wound healing experiments and results. In doing so I will follow the original publications, which are suggested for greater detailed reading and an introduction of different cell environmental properties [11] [15] [19]. As aforementioned, there are two main mechanisms cells apply to close a physical void:

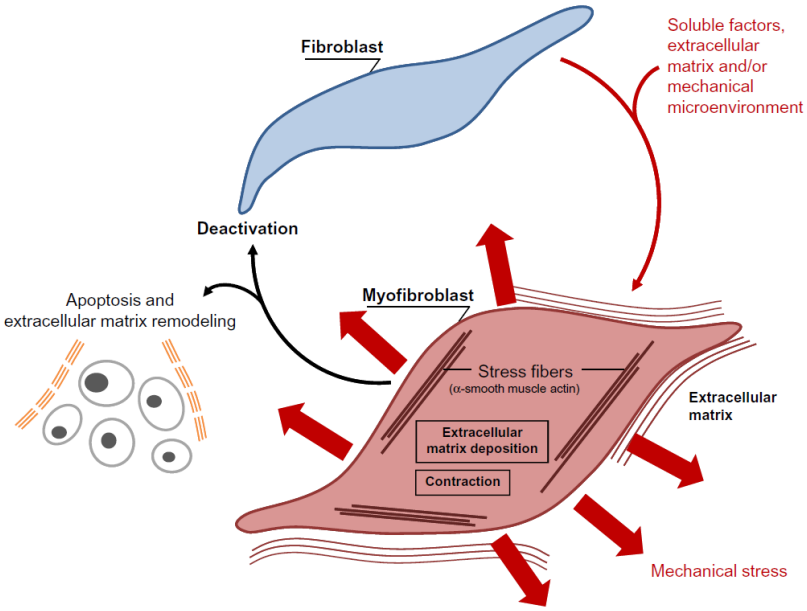

Figure 2.6.: **Schematic of fibroblast to myofibroblast transition.** In contrast to fibroblasts, myofibroblasts develop significantly more stress fibres. They continue to evolve into differentiated myofibroblasts with stress fibres containing α-smooth muscle actin. This differentiation, however, does not necessarily always take place, but a deactivation or retransition has not been seen in vivo. Adapted from citeDarby2014.

"purse-string" contraction via a pluricellular actomyosin cable at the free edge, and cell crawling into the open space through lamellipodia mediated protrusions. While "purse-string" closure dynamics seem to dominate in vivo studies, in vitro wound closure was dominated by cell crawling. It is assumed, that for successful in-vitro purse-string closure active epithelial fluctuations are required to cover non-adherent areas larger than a single cell.

The following section will focus on epithelial wound healing. While that is different than internal tissue healing, especially cardiac tissue healing, the theories and mechanisms explained provide a good foundation for possible dynamics in other cases. That is further reinfoced by the fact, that epithelization is not just important in skin wound healing, but embryonic morphogenesis, regeneration and cancer dynamics. Several studies could show, that the type of cell closure does not only depend on wound size and geometry, but also cell type. The geometrical aspect could be shown to be especially important through visualisation of complex force fields that develop around the free edge of the monolayer. These force fields varied depending on size and shape of the free area. However, these first measurements were done with a scratch assay, meaning a wound is inflicted on a cell monolayer by scratching it with a sharp edge. It is important to mention at this point, that while it is a cheap and simple method, the resulting wound parameters are not easy or precise to control. Additionally, there are influences that may alter cell behaviour. As the scratch destroys cells, those removed cells release their content into the medium, leading to a non-controlled and no longer clearly-defined environment. For the surviving

border cells this is a traumatic stress, and they may become partially permeable due to the violent tearing off of adhesive junctions and cell-cell contacts. This can lead to sudden medium influx, which in itself might trigger migration.
By not using a scratch-assay and instead non-invasive blocks that leave open spaces without having to kill cells, influences of the surface release are can be studied uncoupled from all damage and permeablilisation influences. The release of available surface thus leads to collective motility which shows a certain duality in contributions from individual and collective cell movement. This was shown to be independent of cell proliferation, but related to the fraction of surface initially covered. As mentioned above, very long range velocity fields could be observed, implying the interplay of a large number of cells. In contrast to this collective behaviour, individual active "leader cells" were observed that destabilize the border through fingering instabilities. These "fingers" posses a pluricellular actin belt at their sides that is assumed to act as origin for mechanic signaling. Now, cells are typically motile as response to a given stimulus. As such, they either dissociate, explore the surrounding individually, or collectively invade a free surface while maintaining cell-cell contacts. This last behaviour, especially, plays a big part in wound healing, and the progression provides important information on the motile phenotype of cells. The two main mechanism of closing a wound were briefly mentioned above. Firstly, there is "purse-string" closure:
This is especially effective for relatively small wounds, not very much larger than cell size. In this case a pluricellular continuous actin beld along the wound border in contracted via myosin motors, and thus, the wound closed. Secondly, there is closure through cell crawling:
This case describes the collective motility of the border cells moving into the open space to close the void while maintaining the integrity of the epithelium including cell-cell contacts with the respective cadherins. It should be mentioned that while it is clear, that this motility is acquired, the trigger is not completely clear. In most cases these two mechanisms are not exclusive but rather work together.
Additionally to crawling, active development of coactive "cryptic" lamellipodia have been observed for MDCK cells that form under other cells away from the border cells. The onset was shown to be dependent on initial cell density, rather than cell division rate. Marginal protrusions along borders, on the other hand can take the appearance of so called "leader cells". "Leader cells" are very active cells that loose some of their epithelial characteristics. As such, they develop a Rho-dependent active lamellipodium by draging some cells after them. To determine what might induce such a behaviour or if it might be intrinsic to the acquired motility, the group studied "wounds" created by PDMS microstencils. From this they could conclude, that a free surface is sufficient to trigger migration, as cells were progressively motile perpendicular to the free edge after just a few hours of removing the microstencils. Overall they could show that the velocity of closure progressed non-linearly and for a wound size above 150µm independent of the width. For wound sizes of about 100µm, or approximately 8 cell diameters, the progression slowed down and showed different dynamics, as presumably the small distance does not allow borders to act independently.
For further investigations the group introduced a simple stochastic model based on

three determining contributions: firstly purse-string contractility, secondly tissue fluctuations and thirdly effective friction. It has been suggested that in-vivo tissue fusion adapts to the environment by coordinating lamellipodia protrusions and purse-string contractions. But it could be seen that border protrusive activity drives epithalization despite a contractile actomyosin cable at the wound periphery. This leads to the need to define an "epithelisation coefficient" defined by the ratio of protrusive stress over tissue-substrate friction. This coefficient allows the model to be adapted to the classification of different cell phenotypes. In this continuum-mechanics model, only closed-contour wounds were considered and further assumed to be circular and all parameters can be estimated from experiments. There are additional variants derived including a minimal model and characteristic migration phenotypes.
Basic quantities to be defined were experimental values, like the *circularity* $c(t)$:

$$c(t) = \frac{4\pi S(t)}{P(t)^2}, \qquad \begin{matrix} S(t) : \text{area of wound} \\ P(t) : \text{perimeter of wound} \end{matrix} \tag{2.1}$$

As such, $c = 1$ for a circle, $c = \frac{\pi}{4}$ for a square and in general $0 \leq c \leq 1$ for a closed curve. Similarly a radial wound closure velocity component was defined proportional to $\frac{1}{r}$ with an effective radius $R(t)$

$$R(t) = \sqrt{\frac{S(t)}{\pi}} \tag{2.2}$$

, which eventually allows the relation to a margin velocity. Throughout the closure, is radial component is directed towards the initial center of the wound, implying an incompressibility of the monolayer.
The closing behaviour for different sized wounds was studied and different behaviours found depending on the wound size. Larger wounds (R_w =100µm to 250µm), rapidly lost their circular shape due to the formation of leader cells around the margin and subsequent "fingers" that eventually merged within the wound, leaving smaller secondary holes. This behaviour is identical to large rectangular wounds that were studied before with a scratch assay. In contrast to this, smaller wounds (R_w =100µm) closed without obvious leader cells and with only minor distortions to their shape.
Upon closer examination of the underlying force-generation mechanisms of wound closure, lamellipodia at the margin were found to be variable in number and size with a preferential orientation, in contrast to cryptic lamellipodia in the tissue, that showed no preference in orientation. The continuous actomyosin cable formed just minutes after the pillars were removed and was under tension, as it exerts a centripetal force on the closing epithelium.
For a quantitative description one describes the wounded tissue as an epithelial space outside of a disk-like wound with radius $R(t)$ with initial radius $R_0 = R(t = 0)$. Lamellipodia exert a constant protrusive stress σ_p and the force of friction between epithelium and substrate that is proportional to closure velocity, is defined by a *friction coefficient* ξ.

In summary, there are four distinct properties to be preserved in the model: (i) the cell number density n is uniform $n = n_0 \approx const$, which means that cell division and death are negligible as the number of cells is conserved:

$$\partial_t n + \partial_\alpha (n v_\alpha) = n (k_d - k_a) . \tag{2.3}$$

Here, v_α denotes the tissue velocity field, $k_{d,a}$ the respective rates of cell division and apoptosis.
(ii) there is no orientational order in the tissue. This rotational invariance is expressed in the writing of the velocity field as $\vec{v} = v_r(r,t)\vec{e}_r$, depending on the distance r relative to the origin. (iii) the wound remains approximately circular. This is ensured by considering the above mentioned radii. (iv) the tissue is considered as an incompressible flow, using the boundary condition:

$$\vec{\nabla} \cdot \vec{v} = \partial_\alpha v_\alpha = 0 \tag{2.4}$$

This further means that mechanical forces are locally balanced:

$$\partial_\beta \sigma_{\alpha\beta} = -f_\alpha^{ext} \tag{2.5}$$

, with the stress tensor $\sigma_{\alpha\beta}$ and exterior forces $f_\alpha^{ext} = -\xi v_\alpha$ due to friction. To solve these equations for deformations and the cell flow field one implements a constitutive equation, that can further be used to describe different epithelial rheologies

$$\sigma_{\alpha\beta} = \sigma \partial_{\alpha\beta} + \tilde{\sigma}_{\alpha\beta}, \qquad \tilde{\sigma}_{\alpha\alpha} = 0. \tag{2.6}$$

If one now considers a model wound with initial radius R_0 created at $t_0 = 0$, centered around the origin O. The forces exerted at the margin during closure provide another boundary condition including contributions from both protrusive stress σ_p and tension γ due to purse-string forces:

$$\sigma_{rr}|_{R(t)} = \sigma_p + \frac{\gamma}{R}. \tag{2.7}$$

By defining a length scale $R_\gamma = \frac{\gamma}{\sigma_p}$ two distinct dynamic regimes can be distinguished. For $R < R_\gamma$ purse-string closure dominates the dynamics, for $R > R_\gamma$ protrusive forces dominate the closure dynamics.
If one further assumes an inviscid fluid, the stresses are purely isotropic $\sigma = -P$, and this isotropic part becomes a Lagrange multiplier: $\sigma_{\alpha\beta} = -P\delta_{\alpha\beta}$, with the pressure field P at the ephithelial scale. Together with the assumptions (ii)-(iv) from above, this yields the following force balance equation

$$\partial_r P = -\frac{\xi R \dot{R}}{r} \tag{2.8}$$

$$\tag{2.9}$$

R_{max} denotes a defined long-range cut-off radius, as $r \to \infty$ is ill defined, and thus

$P(r)|_{R_{max}} \to 0$. Including now the stress boundary condition yields

$$\xi R \ln \frac{R}{R_{max}} \dot{R} = \sigma_p + \frac{\gamma}{R}. \tag{2.10}$$

Normalising this by the characteristic length scale R_γ provides

$$\mathrm{d}t = \frac{\xi}{\sigma_p} \frac{R^2}{R + R_\gamma} \ln \frac{R}{R_{max}} \mathrm{d}R. \tag{2.11}$$

Integration of this equation together with the definition of a "diffusion coefficient" $D = \frac{\sigma_p}{\xi}$ and the use of the dilogarithmic function $\mathrm{Li}_2(x) = \sum_{k=1}^{\infty} \frac{x^k}{k^2}$, yields the result of

$$\begin{aligned} 4D\tilde{t}(R) = &- R^2 \left(1 + 2 \ln \frac{R_{max}}{R}\right) + 4R_\gamma R \left(1 + \ln \frac{R_{max}}{R}\right) \\ &+ 4R_\gamma^2 \left(\mathrm{Li}_2\left(-\frac{R}{R_\gamma}\right) - \ln \frac{R_{max}}{R} \ln \frac{R + R_\gamma}{R_\gamma}\right). \end{aligned} \tag{2.12}$$

Solving this equation for the initial condition of starting at $t(R_0) = 0$ further gives us a finite closure time. A simplified solution is further found when assuming that force contributions from the acto-myosin cable can be neglected ($R_\gamma \to 0$) for the time progression $t(R)$ and a specific closure time $t_c(R_0)$:

$$t(R) \approx \frac{R_0^2}{4D} \left(1 + 2 \ln \frac{R_{max}}{R}\right) - \frac{R^2}{4D} \left(1 + 2 \ln \frac{R_{max}}{R}\right), \tag{2.13}$$

$$t_c(R_0) \approx \frac{R_0^2}{4D} \left(1 + 2 \ln \frac{R_{max}}{R_0}\right). \tag{2.14}$$

2.2. Electric Cell-Substrate Impedance Sensing (ECIS)

Electric-cell-substrate impedance (ECIS) measurements are a well established means to monitor cell movement and vitality since the 1980s, especially quantitatively after a comprehensive model was introduced by Giaver and Keese in 1991 [20]. ECIS has been widely used in a variety of different forms of analyses since the 1930s [21]. Away from the life sciences, Impedance Spectroscopy is a powerful tool to study electrical properties of materials and their interfaces, especially when rather than a time/concentration dependency, one is interested in frequency related phenomena [22]. This is especially interesting when considering the increasing use of ionic, semiconducting, mixed electronic-ionic and dielectic materials in almost all areas of modern life. Applications of such techniques in the life sciences field can range from basic cell biology research [23] and cancer research [24], over drug screening [25] to environmental pollution [26] and food safety detection [27]. Cell-substrate impedance measurements in particular is used to gain insight into important parameters determining cells' passive electrical, cell shape dependent properties determining the vital status [21], as well as adhesive and migratory properties since first introduced by Giaever and Keese in 1984 [28]. A main upside to this method is the possibility to monitor real time cell behaviour with nanometer accuracy and without being invasive to the system. In comparison to microscopic approaches, that rely on invasive fluorescence labelling and often cell counting, ECIS is a less time consuming mean to study for example wound healing behaviour in an in-vitro system. Wound closing behaviour is strongly influenced by cell shape, stiffness and the pressure due to cells migrating into the created wound. This method further offers the possibility to quantitatively monitor multiple culture samples, with up to 96 in the case of the commercially available product by applied biophysics used in the present study, in one measurement.
Properties are derived from a systems response to a frequency dependent excitation signal, typically a small alternating current in the range of 10Hz to 100kHz. The system response is measured as electrical impedance, the resistance of an electric circuit to a current under applied voltage

$$Z(\omega) = \frac{U(\omega)}{I(\omega)} = \frac{u(t)}{i(t)} \tag{2.15}$$

and, therefore, corresponds to an ohmic Resistance without the idealising assumption of not containing any capacitive or inductive parts [29]. Real and imaginary component of this complex impedance are written to represent a characteristic resistance R and reactance X

$$\underline{Z} = |\underline{Z}|\, e^{j\phi_x} = \mathrm{Re}\,(\underline{Z}) + j\mathrm{Im}\,(\underline{Z}) \tag{2.16}$$

$$= R + jX. \tag{2.17}$$

Assuming an ideal capacitor with a non-vanishing imaginary reactive impedance only, in contrast to an ideal resistor with an entirely real resistive impedance, an

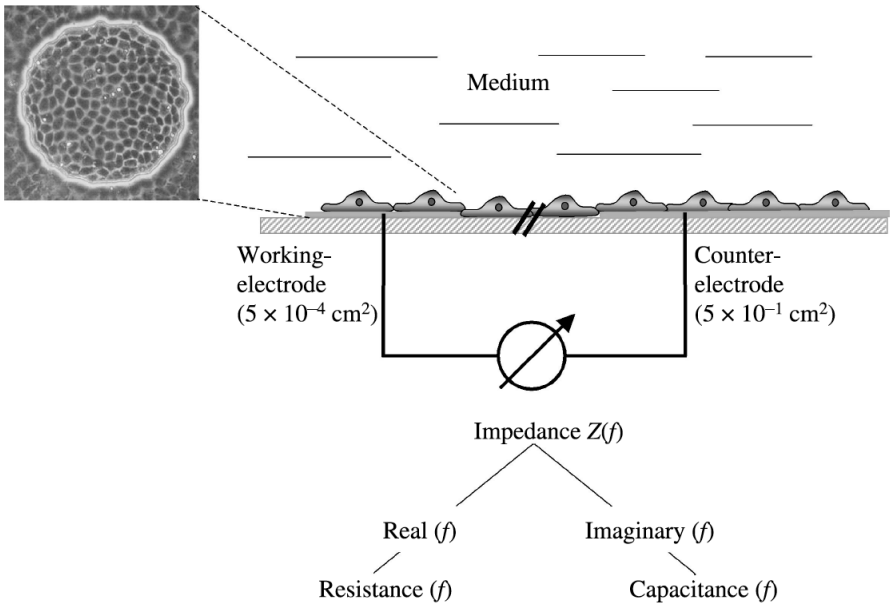

Figure 2.7.: **Schematic electrode set-up of an ECIS measurment.** The impedance is measured between a counter-electrode and a significantly smaller working-electrode. This resulting signal of the cell covered electrode is further analysed for cell behaviour, such as adhesion, migration and cell-cell contacts strength after separation in real and imaginary part.

expression for the capacitance as function of the impedance can be derived

$$\underline{Z}_{imag} = jX = \frac{-j}{\omega C} \tag{2.18}$$

$$\Rightarrow \qquad C = \frac{1}{2\pi f X}. \tag{2.19}$$

This response signal is measured between a counter-electrode and a significantly smaller working electrode as depicted in Figure 2.7. Due to difference in size which is usually around the factor 10^3 that part of the impedance signal contributed by the smaller working electrode dominates the response, thus allowing for the high sensitivity up to nm height changes provoked by single cell movement [30]. This indicates how working electrode size is the most critical parameter determining measuring sensitivity, limited by the constriction resistance.
On another note, an ECIS measurement is generally done over several orders of frequencies as the response signal contains different information depending on the excitation signal frequency. In consequence there are two main frequency regimes to be considered:
Firstly the lower regime with frequencies below 1kHz and secondly the higher frequencies above 4kHz. This distinction is based on a change in the current flow relative to a cell body. At lower frequencies and low current amplitudes a cell body acts as an insulating particle forcing currents to flow below and around the cell body and "through" the pores formed in between the cell-cell contact-cleft. As a result,

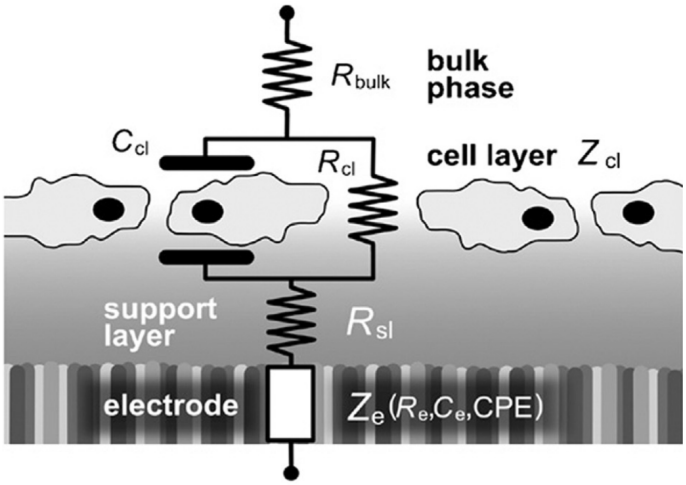

Figure 2.8.: **Electrical circuit cell model.** This simple model of a cell as an electric capacitor connected by the extracellular matrix and medium to an electrode it is spread on provides a quantitative means for analysis of an impedance signal in regard to cell spreading and intercellular contact. A current has different options to pass a cell monolayer, coupling either capacitively through a cell body or passing underneath and between cells through the closest cell-cell junction. This contributes to differing informational content of a resulting impedance signal depending on the excitation signal frequency.

the greatest contribution to the impedance signal stems from the cell-substrate adherence zone and contact area between neighbouring cells, making this frequency band especially sensitive to cell-cell contacts and cell shape in general. In contrast, frequencies above 4kHz and high current amplitudes are especially useful for adhesive studies because a current will mainly flow through a cell body and only to an insignificant extent around it. A current in this regime capacitively couples through a cell body as a displacement current, allowing a cell to be modelled as a capacitor and extract both membrane capacitance as well as electrode coverage.
As such, there are different circuit models to describe the flow of a current from a cell covered electrode to another depending not only on cell type but just as much, as is often the case with theoretical models, on the degree of abstraction. One of the simpler but very efficient models describes a cell as shown in Figure 2.8 as a capacitor with an inductor in parallel. The intrinsic characteristic of an electrode is taken into account, as well as the bulk resistance of the cell medium, which acts as conducting electrolyte, in the form of another inductor, differing from the one acting as transition to the bulk phase. What is indicated as support layer in Figure 2.8 is comprised of a substratum and the adjoining junction to a cell. The substratum is an often necessary coating of an electrode enabling cells to spread and adhere to a surface resembling the extracellular matrix. The ECM is a network connecting cells with membrane proteins to the substratum and forming another small $10 - 200$nm protein layer between membrane and substrate. This ECM is neglected in this model as such a differentiation provides no new information during later analysis of wound

closure. Cell proliferation and viability can be inferred from different factors like shape fluctuations and tightness of cell-cell junctions and the area over which a cell is spread, as this directly relates to the cell shape [21] [31].
We will now look at the origins and foundation of these considerations of a cell as electric capacitor comprised in an electric circuit with the electrodes, substrate and cell medium. This explanation should be able to provide the interested reader with a starting point for further reading. The interpretation of an impedance signal being equivalent to that of a capacitor and resistor in series was first done by Warburg in 1901 [32]. The "Warburg impedance" is used to describe an electrochemical system. For this Warburg impedance it is assumed that transport between electrode surface and solution, or substrate in our case, happens only through linear diffusion and, with that, is independent of other processes. In that case the diffusion flux J_k relates to the transmitted current I according to the continuity equation. The Nernst-diffusion layer, or electrical double layer, itself describes a double layer that forms around a solid surface in contact with a fluid, i.e. an electrode submerged in an electrolyte. The first layer of this double layer refers to the surface charge distribution of the solid, while the second layer is comprised of molecules of the opposite charge in the fluid that arrange along the surface due to Coulomb interactions. This second layer shields the surface of e.g. an electrode to a certain degree from the remaining fluid, depending on the "Debye screening length". This characteristic thickness of the double layer is reciprocally proportional to the concentration of particles in the solution. Considering now the flow of charged particles from the electrode through the fluid by diffusion one needs to account for possible perturbations to the system due to the flow. This perturbation carries on through the solution as a damped wave and growing smaller in amplitude over the length of the penetration depth into the solution. This penetration depth grows longer with smaller frequencies, but as long as it remains small in comparison to the thickness of the Nernst diffusion layer, perturbations due to flows in the solution, i.e due to convection, can be neglected [33].
From these considerations a circuit model can be formulated to interpret a measured impedance signal which is an expression of how a current flows through a system. Straight forward, a current flows from an electrode through a cell substrate, necessary for cells to adhere to the electrode, the extra-cellular matrix, the whole cell body and cell medium. In this case the cell medium works as an electrolyte enabling a current flux in the first place. The cell body itself with its membrane acts as a capacitor.
This ensures that the presence of cells is not overshadowed by the resistance of the medium, as the impedance signal from this electrode-electrolyte surface is inversely proportional to the electrode area. By making the diameter sufficiently small, the impedance signal, especially the real part which corresponds to the faradaic resistance can be assured to dominate the constriction resistance and with that clearly reveal adherent cells and their behaviour [20]. In principle, this works by applying a frequency-dependent excitation, AC signal, $U(\omega)$ to a system and measuring the resulting response.
These higher frequencies capacitively couple through cells, passing through the ventral and dorsal membrane in the form of a displacement current. As the current

does not go around the cell body to a significant extent, cells are modelled as capacitors. This especially provides insight into cell adherence to the substrate and vitality as the current passes through the entire cell body with organelles charged molecules and more. Such capacitive behaviour is reflected in the *resistance*, the real part of the impedance signal.
As illustrated in Figure 2.7 the impedance signal $Z(\omega)$ measured between working and counter electrode can be written in terms of an imaginary part, the *reactance* or capacitance, and a real part with resistance as characteristic quantities of the system. This is easily seen when writing the impedance as a resistance following Ohms law. These considerations show the diverse applicability of the ECIS method and with it the need for different models describing the system depending on the situation, i.e. the frequency or cell type, and information wanted from the measurement. It was mentioned before, that the basis for such models is the formulation of the cell as a capacitor. The simplest case to consider for this is a single-shell model as introduced in [20] and illustrated in the upper right corner in Figure 2.9b, which shows the cell as a spherical shell capacitor. The cell membrane acting as shell with finite thickness d and overall cell radius R separates the surrounding culture medium with characteristic electric permittivity ϵ_m and conductivity σ_m from the inner cell with cytoplasm, organelles and other molecules that are summarised as ϵ_i and σ_i. As the membrane has a finite thickness it is not neglected but considered as ϵ_{mem} and σ_{mem}. The limits of this model are soon apparent when regarding different cell types. Especially looking at a colony of typical 3T3 fibroblasts as shown in Figure 2.9a, the assumption of a spherical cell is inadequate. Fibroblasts have the tendency to align with each other which inhibits motion through the contact as they are a rather quiescent cell type. This means that the transcellular resistance is so small that it is difficult to measure and fit accurately during analysis, unless this significance difference in electrode size is deployed.
Alternatively Lo and Ferrier introduced a more complex model of a cell as flat rectangular box with a half disk on each end as shown in Figure 2.9b [34]. From this assumption the impedance can be calculated as a sum of the two shaped contributions of a sphere and a rectangle and leads to the overall expression for the impedance of a cell-covered electrode Z_c

$$\frac{1}{Z_c} = \frac{1}{Z_n + Z_m} \left\{ \begin{array}{l} 1 + \left(\frac{LW}{LW + \frac{\pi W^2}{4}} \right) \frac{\frac{2Z_m}{Z_n}}{\gamma W \quad \coth\left(\frac{\gamma W}{2}\right) + 2R_b^{rec}\left(\frac{1}{Z_n} + \frac{1}{Z_m}\right)} \\ + \left(\frac{\frac{\pi W^2}{4}}{LW + \frac{\pi W^2}{4}} \right) \frac{\frac{2Z_m}{Z_n}}{\frac{\gamma W}{2} \frac{I_0(\gamma W/2)}{I_1(\gamma W/2)} + 2R_b^{disk}\left(\frac{1}{Z_n} + \frac{1}{Z_m}\right)}. \end{array} \right. \tag{2.20}$$

W and L are cell width and length respectively, while ρ represents the resistivity of the bulk culture medium. I_0 and I_1 are the zeroth and first order modified Bessel functions of the first kind. The parameter γ abbreviates

$$\gamma = \left[\frac{\rho}{h} \left(\frac{1}{Z_n} + \frac{1}{Z_m} \right) \right]^{\frac{1}{2}}, \tag{2.21}$$

with Z_n the specific impedance of the cell-free electrode modeled CPE (constant phase element, impedance at the electrode-medium interface) and Z_m the specific

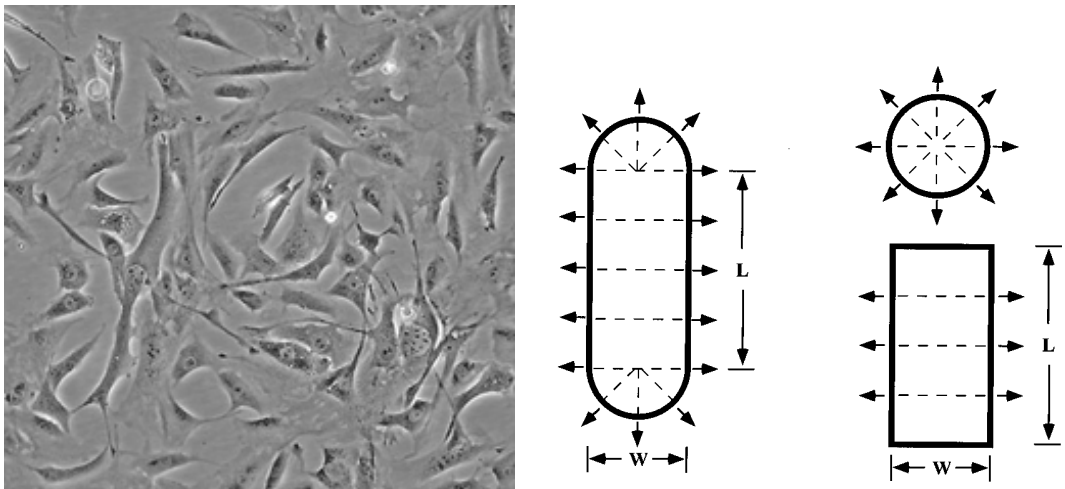

(a) The image shows a culture of fibroblasts imaged using light microscopy [35]. The elongated shape makes obvious, that a circular approximation of this cell type is not an appropriate fit.

(b) In their model for impedance analysis of cells from 1998 Lo and Ferrier introduced the cell as a sum of a rectangular contribution with a half sphere at each end [34].

Figure 2.9.: Bringing into agreement a modelled fibroblast with the shape observed in a bright field image.

membrane impedance of the cell:

$$Z_m = \frac{1}{\mathrm{i}\omega C_m}. \tag{2.22}$$

C_m describes the average capacitance of both apical and basal cell membranes and, as such, can provide important information about cell vitality. This provides us with different quantities one can analyse to draw conclusions about cell behaviour during wound healing.

2.2.1. Surface Coverage

We will focus on the fit parameters R_b, α and C_m on one hand and on cell spreading behaviour on the other hand. The most direct approach in order to make a statement about the spreading behaviour, is to analyse the capacitance C_{total}, which corresponds to the imaginary part of the impedance signal

$$C_{total} = \frac{1}{2\pi f \cdot X_{total}}, \tag{2.23}$$

with X_{total} the ratio of cell-covered to cell-free electrode. The capacitance signal of an electrode completely covered by cells $C_{cell-covered}$ is derived from the monolayer formed approximately 24hrs after seeding the cells. This includes contributions to the capacitance from the electrode and the basal and dorsal membranes in contrast to

the cell-free capacitance that boils down to the capacitance of the electrode $C_{electrode}$.

$$\frac{1}{C_{total,Z_M}} = \frac{1}{C_{cell-covered}} = \frac{1}{C_{electrode}} + \frac{1}{C_{membrane1}} + \frac{1}{C_{membrane2}} \tag{2.24}$$

$$C_{total,Z_N} = C_{electrode} \tag{2.25}$$

From this, the capacitance C_{total} can be related to all in between stages of coverage by adding the capacitance of the cell-free electrode $C_{electrode}$ according to the ratio of coverage $x_{coverage}$

$$C_{total} = (1 - x_{coverage}) \cdot C_{cell-free} + x_{coverage} \cdot C_{cell-covered}, \tag{2.26}$$

$$\text{with } x_{coverage} = \frac{cell - coveredArea}{totalelectrodeArea}. \tag{2.27}$$

This can be especially informative when related to the spreading rate s which corresponds to the slope of the recovery curve when plotting the measured capacitance over time.

2.2.2. Fitparameters

R_b, α, C_m are important parameters used to fit this model to experimental data and gain information depending on the cellular behaviour. As can be seen in Equation 2.28, α directly relates to height of the basal membrane above the substrate and gives insight into adhesive and spreading behaviour of a cell. An explicit derivation of these parameters can be found in the paper by Lo and Ferrier introducing this model [34]. A very important further result that is gleaned from this is the parameter R_b, the junctional resistance between cells calculated from R_b^{rec} and R_b^{disk} as contributions from the rectangle and disk respectively

$$\alpha = \frac{\gamma W}{2}\left(\frac{1}{Z_n} + \frac{1}{Z_m}\right)^{-\frac{1}{2}} = \frac{1}{2}W\left(\frac{\rho}{h}\right)^{\frac{1}{2}}, \tag{2.28}$$

$$R_b^{rec} = \frac{\frac{4L}{W} + 2\pi}{\frac{4L}{W} + \pi} R_b, \tag{2.29}$$

$$R_b^{disk} = \frac{\frac{2L}{W} + \pi}{\frac{4L}{W} + \pi} R_b. \tag{2.30}$$

This junctional resistance R_b is proportional to the medium resistivity ρ. From this one can draw conclusions about the cells metabolic activities because those affect the area over which a cell spreads, the closeness between adhering cells and the tightness of cell-cell junctions, as well as their fluctuations. Cell-cell junctions also not only tell us in what adherent stage cells are and how close they are bound to their neighbours but further what cell-type one is regarding. This might seem trivial at first, but for this work it is an important point, as especially the transformation from fibroblast to myofibroblasts was to be studied. That is possible because of the diffusion barrier of a cell layer. As such, fibroblasts do not form tight-junctions between neighbouring cells in contrast to myofibroblasts. During apoptosis, however cells shrink and with that loose contact to their neighbours. Further, blebbing of nuclear and plasma

membranes can occur, while during necrosis the plasma membrane directly looses its integrity; both occur upon wounding.
All these factors together and by themselves change cells' morphology significantly, making such a change quantitatively detectable during an ECIS measurement. From this we can calculate the differences between cellular monolayers before and at certain points after wounding as cells have closed the wounded area. But one also needs to allow for higher cell concentrations in the culture well than are typical in natural environment. Such a high cell concentration is used to reduce proliferation influences and allows us to assume homogeneous coverage.

2.2.3. Recovery Rate

Quantitative conclusions can not only be drawn from fit parameters using the model Lo and Ferrier introduced [34] but also from the recovery curve recorded. Both from the real, as well as the imaginary part of a recovery curve, as shown in Figure 2.10, a recovery rate s can be calculated, from the intervall between the wounding and the recovery of the previous monolayer signal. In this interval we fit a sigmoidal function and determine a specific recovery rate and half time [16]. Applied on an averaged dataset, the appropriate errors are calculated according to the Gaussian propagation of uncertainty.

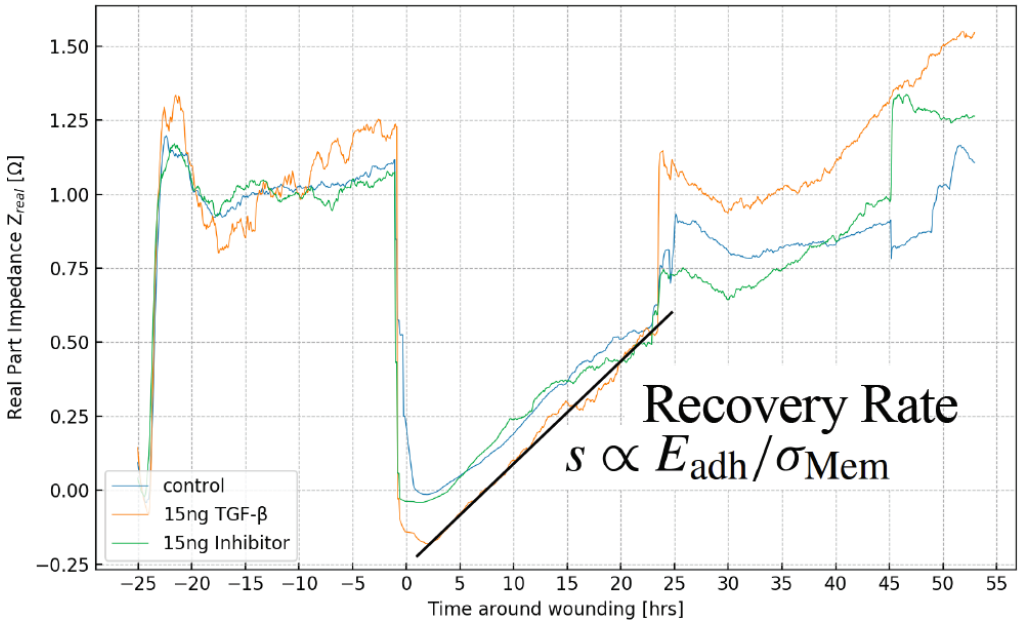

Figure 2.10.: Example for an ECIS recovery curve. This curve shows exemplary the real part of the impedance signal of three ECIS recovery curves of 3T3 fibroblasts with varying TGF-βconcentrations. The black line illustrates a possible approximation of the recovery rate.

2.3. Microfluidics

Microfluidics is a powerful and well established tool for flow experiments and droplet creation. Due to its straightforward nature in application and high-throughput yield microfluidic devices have become a standard means to create artificial compartments. For this end, the natural dripping motion of a liquid flow occurring under certain conditions presents itself as an easily controllable way to create monodispersed droplets. This further showcases how there is a second, surrounding, fluid phase needed that provides the necessary interface between the two immiscible fluids. Of course, polydispersed droplets are formed just as easily by shear or impact with the fluids surface, but this will not be further examined in this work. There are different microfluidic flow setups one can use to create monodispersed droplets, but to understand the underlying principles of droplet formation, firstly the basis of co-flow dripping will be explained.

2.3.1. Co-Flow Principles

A co-flow setup consists of two immiscible fluid phases of which one flows around the other creating an interface between two regimes of different properties. The ratio of these both intrinsic and controllable properties between both phases, determines the flow behaviour of the inner fluid. Two characteristic parameters to describe such flow dependencies are the *capillary number Ca* and *Weber number We*:

$$Ca = \frac{\text{viscous shear force}}{\text{surface tension force}} = \frac{\eta \cdot u}{\gamma}\ , \tag{2.31}$$

$$We = \frac{\text{inertia force}}{\text{surface tension force}} = \frac{\rho \cdot u^2 d}{\gamma}. \tag{2.32}$$

In this case u denotes a flow velocity, d a characteristic length scale with η viscosity and γ surface tension. These two quantities further define the *Reynoldnumber Re* typically used to describe a flow behaviour:

$$Re = \frac{We}{Ca} = \frac{\rho \cdot ud}{\eta}. \tag{2.33}$$

While both Ca and We can be calculated for inner and outer fluid, the system is sufficiently described by Ca_{out} and We_{in} as can be seen in Figure 2.11. It is essential to note that for length scales smaller than the capillary length L_c gravity does not affect the droplet and surface tension dominates shear force by viscous drag for small droplets. This makes droplet formation by pinching of the main stream possible and relates droplet size directly to fluid properties and velocity:

$$d_{drop} \sim d_{tip} \cdot \frac{\gamma}{\eta_{out} u_{out}} = d_{tip} \cdot \frac{1}{Ca}. \tag{2.34}$$

The dependence on d_{tip} is a necessary material constant stemming from the syringe tip diameter. Looking at this relation from Equation 2.34 in Figure 2.12 it becomes clear that drop diameter only depends on the outer fluid. With η and γ being

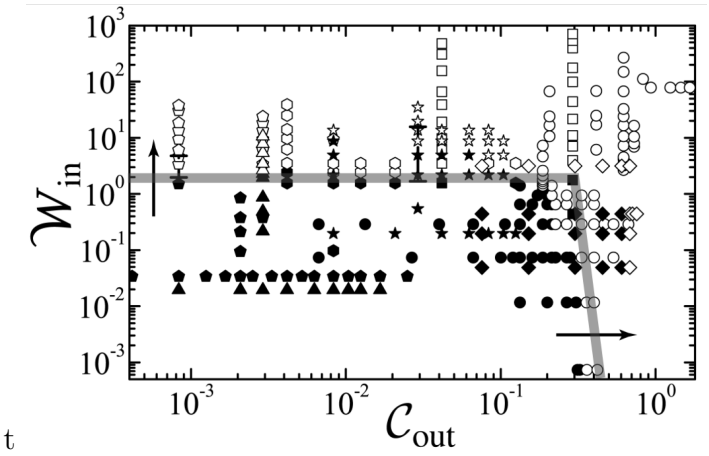

Figure 2.11.: **State diagram of the dripping-to-jetting transition in a coflowing stream as a function of Ca_{out} and We_{in}.** Filled symbols represent dripping while open symbols represent jetting. Each shape is a different viscosity ratio, surface tension, or geometry. Surface tension is 40 mN/m unless otherwise stated. Squares and diamonds: $\eta_{in}/\eta_{out} = 0.01$ with slightly different geometries; Hexagons and circles: $\eta_{in}/\eta_{out} = 0.1$ with slightly different geometries; Pentagons: $\eta_{in}/\eta_{out} = 1$; triangles: $\eta_{in}/\eta_{out} = 10$; stars: $\eta_{in}/\eta_{out} = 10$ and $\gamma = 4$mN/m. Typical error bars for different surface tensions are shown. Reprinted from [36]

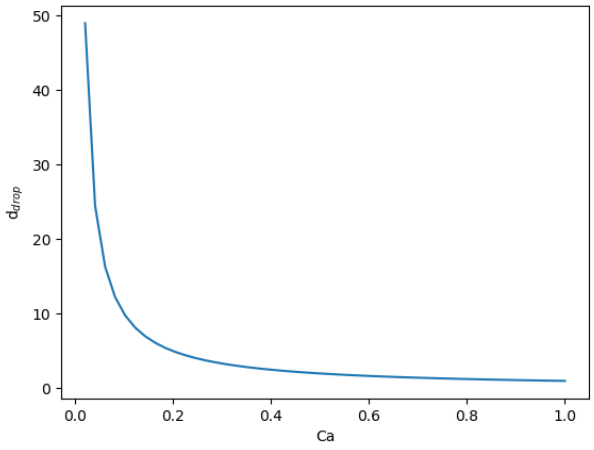

Figure 2.12.: Drop diameter depending on capillary number Ca. From Equation 2.31 it becomes clear that drop diameter only depends on Ca_{out}, and, therefore, can be influenced by the outer fluid's velocity u_{out}.

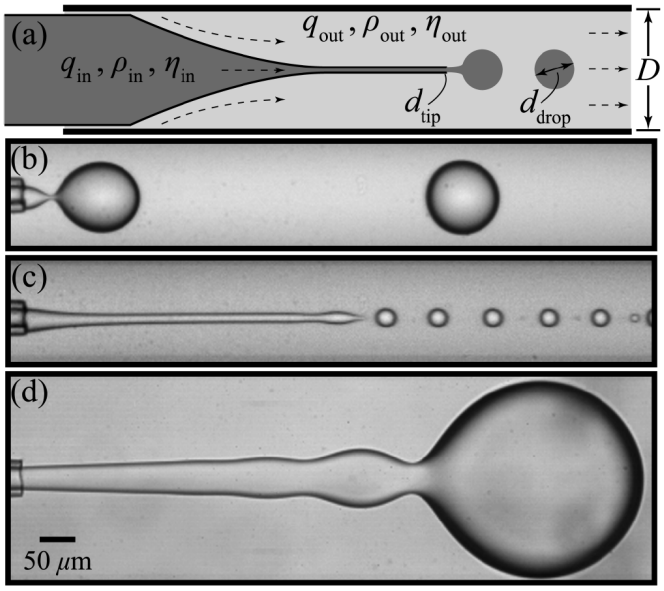

Figure 2.13.: Drop diameter depending on device geometry. (a) Device geometry showing tapered inner capillary in outer square capillary. (b) Image of dripping regime. (c) Image of a narrowing jet generated by increasing q_{out} above a threshold while keeping q_{in} constant, with $\eta_{in}/\eta_{out} = 0.1$. (d) Image of a widening jet generated by increasing q_{in} above a threshold while keeping q_{out} constant, with $\eta_{in}/\eta_{out} = 0.1$. Images (b)-(d) were taken with a high-speed camera (walls not shown). Scale bar applies to (b)-(d). Reprinted from [36]

intrinsic fluid properties, the drop diameter can be controlled by controlling the flow velocity. From the flow relation q_{in}/q_{out} that is proportional to the frequency at which droplets are formed, it follow that the transition from jetting to dripping is influenced by either increasing u_{in} or u_{out}.

This concept is further illustrated in Figure 2.13.
When the outer flow velocity u_{out} is raised, the droplet diameter is reduced until $d_{drop} = d_{tip}$. Is it raised beyond this point, the stream becomes elongated further into a jet and consequently transitions into jetting regime. From such a jet droplets can pinch off at the *Rayleigh-plateau instability*. At this point disturbances intensify to a point where the pressure difference inside the half-spherical tip of the jet is higher than the outside. This is schematically shown in Figure 2.13.

2.3.2. Polymerisation

While the aforementioned procedure creates fluid droplets, they are not stable in their collected "reservoir environment", least of all to be put in a different solution. There are different established materials and methods to use for microcapsules that are to act as carrier system, such as polymerisation, temperature induced gelation and freezing, ionic crosslinking, solvent evaporation or diffusion. While polymerisation is the most commonly used method, in the end it strongly depends on the physical and chemical properties the particles are supposed to exhibit and with it

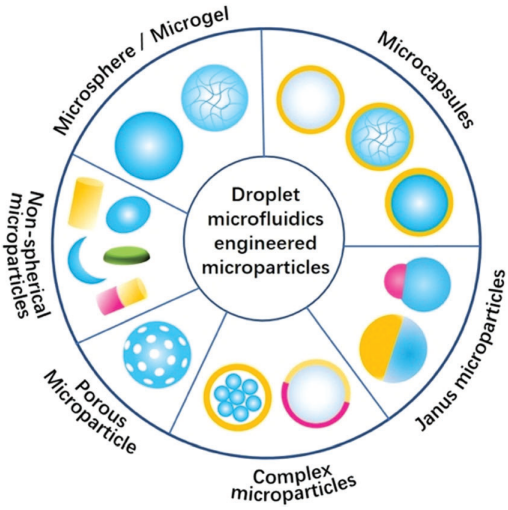

Figure 2.14.: **Different microfluidic particles.** Adapted from [37]

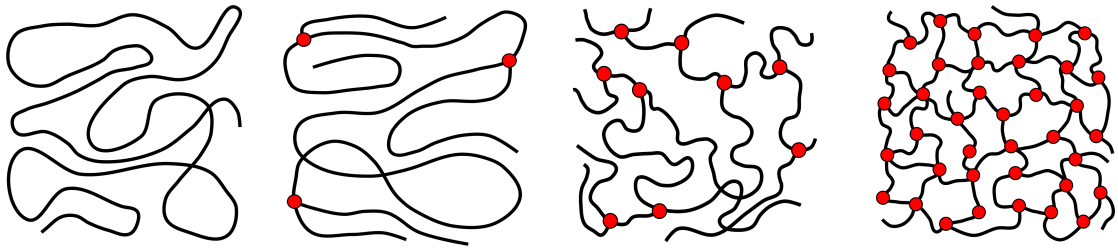

Figure 2.15.: **Levels of crosslinking.**

the material that is to be used. As shown in Figure 2.14 shape and composition can range significantly and thus is highly adaptable to ones purpose. We want to produce a carrier system that is robust against most environmental influences and stable around 30°C, while controllable in its release and efficiency at higher temperatures. Polymerisation is a crosslinking process between repeating subunits of a polymer, or macromolecule. These monomer subunits are not necessarily repeating molecules, but can be different molecules or blocks of molecules repeating alternately, regularly or irregularly, forming a Homomer of one repeating Monomer, a Heteromer of two or Copolymer at least two Monomeric Groups. At first glance, this process might seem to allow little room for irragularities and variants, but at a closer look this is not the case at all. Neglecting multiple Monomers and assuming two different subunits, one finds that they can not only arrange alternating or as (alternating) blocks, but arrange statistically or along a gradient. Monomers do not only polymerise along a line but can form complex structures where the microstructure can determine polymer architecture. As such, the way in which the polymerisation reaction is initiated and maintained determines how branched or crosslinked a polymer will be, ranging from linear unbranched macromolecules over a simple branched case to a highly cross-linked polymer mesh, seen in Figure Figure 2.15. From this it is easy to see how complex and various polymeric structures can get, but for this work the specifics of the polymerisation process are important to encapsulate cytokines. There are many different ways in which monomers can polymerise and how to

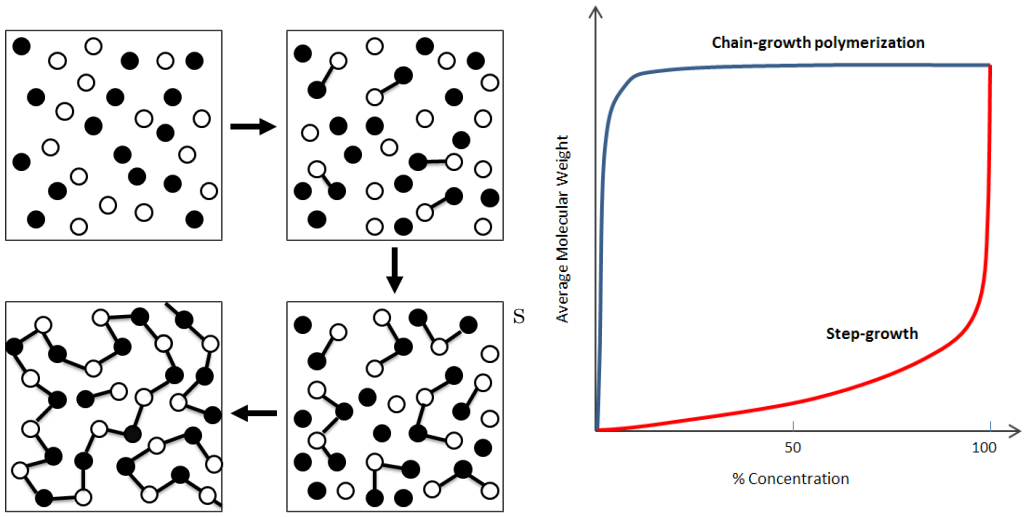

(a) Simplified principle of step-growth polymerisation. [35]

(b) Increase of molecular weight over the duration of the polymerisation process [35].

Figure 2.16.: Different polymerisation growth scenarios.

categorize them. Most commonly one distinguishes chain-growth polymerisation and step-growth polymerisation. During step-growth monomers form first dimers, trimers and oligermors as figuratively shown in Figure 2.16a. Long chain polymers are formed comparatively late, leading to a smaller molecular weight over a long duration of the process.

Chain-growth polymerisation, on the other hand, describes the binding to a main chain of one monomer after the other. This leads to rapid growth of molecular mass but slows down significantly when there are only few monomers left. A comparison of both reactions is shown in Figure Figure 2.16b.

3. Experimental Methods

The methods applied and exemplary experimental procedures are briefly explained in the following section.

3.1. Cell Culture

For all experiments in this work we used 3T3 fibroblasts, one of the most commonly used cell lines since their introduction by Todaro and Green in 1963 [38]. This immortalised cell line derived from mouse embryo was cultivated in the cell lab of the Max-Planck-Institute for Dynamics and Selforganisation in cooperation with the Department of Physical Chemistry at the Georg-August-University Göttingen. The cells were seeded in T25 flasks and cultured in a medium of DMEM (Dulbecco's Modified Eagle Medium) with 10% FBS (Fetal Bovine Serum) and 1% L-Glutamine. This medium was also used during all ECIS experiments. All experiments were conducted without addition of antibiotics to eliminate possible additional manipulations of cell behaviour.

3.2. ECIS Measurements

ECIS experiments were realised with an ECIS ZΘ (Applied BioPhysics Inc, Troy NY) and recorded using software supplied by Applied BioPhysics Inc, see Figure 3.1. This set up is placed in a 37°C incubator to provide appropriate conditions for the cells.

3.2.1. Conducting an ECIS Experiment

An ECIS experiment typically runs over several days, for this work a typical experiment took up to five days. This was necessary, as wound healing process we want to study takes about that long (see Figure 3.2). The typical procedure of one measurement can be followed by looking at the exemplary behaviour of the imaginary part of the impedance in Figure 3.2. On the first measurement day the experiment is started with 250µl culture medium, see section 3.1, only in each culture wells of the ECIS chip, see Figure 3.2 up to (1). Analogous to this the ECIS flow setup was prepared and cells seeded. This is run for approximately one hour to let the medium equilibrate and gain a baseline for the contribution to the signal due to the medium. After this time 250µl of cells, see section 3.1, are seeded into the culture wells in a concentration of $1 \cdot 10^6$ per ml, at approximately (1) in Figure 3.2. With the ECIS flow chips, Figure 3.1a, cells were added from both sides of the chip for a better distribution over the electrodes. The cells are let to rest for 24 hrs in order

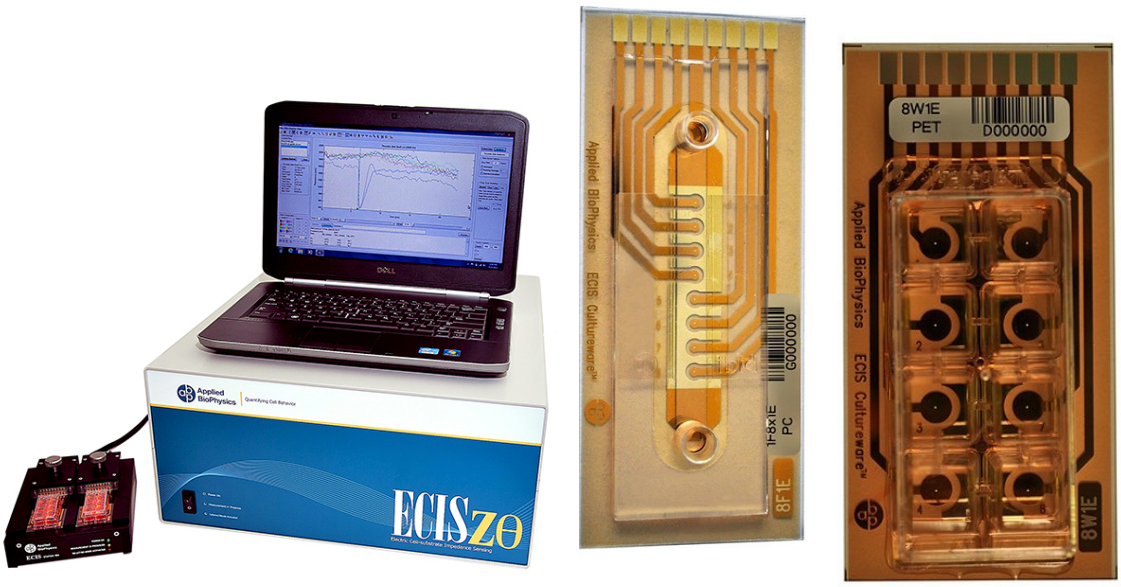

(a) ECIS 8F1E flow chip with 8 electrodes.

(b) ECIS chip with 8 culture wells.

Figure 3.1.: ECIS ZΘmeasurement setup by Applied BioPhysics Inc. [39].

to form a consistent monolayer, see Figure 3.2 (2). Once this has been confirmed the wounding is initiated, through a current of 1800µA at 100.000 Hz applied for 120s to each electrode, see Figure 3.2 (3). After the wounding has been completed, the dead cells and debris are washed from the culture by removing all medium and washing twice with 500µl of medium. If the TGF-β concentration is to be adjusted, the inhibitor or additional TGF-β is resolved in culture medium and added at this point instead of pure culture medium. Otherwise, just as before 500µl of culture medium is added and the cells let to rest for 24hrs. In contrast to this, the flow chip was connected to the corresponding flow pumps which contain either culture medium only, or culture medium with the PNIPAM shells added. After the flow is connected, the fluid is continuously pumped through the chip for approximately 3-5 min. and then disconnected to let the cells rest. Now the recovery can be monitored over the following days, see Figure 3.2 (4), and the measurement terminated when the desired data is collected. Over the concluding measurement days following the wounding the cells are fed approximately every 24hrs with 250µl of fresh culture medium. In this work, the measurement was typically concluded after a total of five days. During that time the signal has either recovered to the initial value of the monolayer, see Figure 3.2 (2), or even overshot, see Figure 3.2 (5).

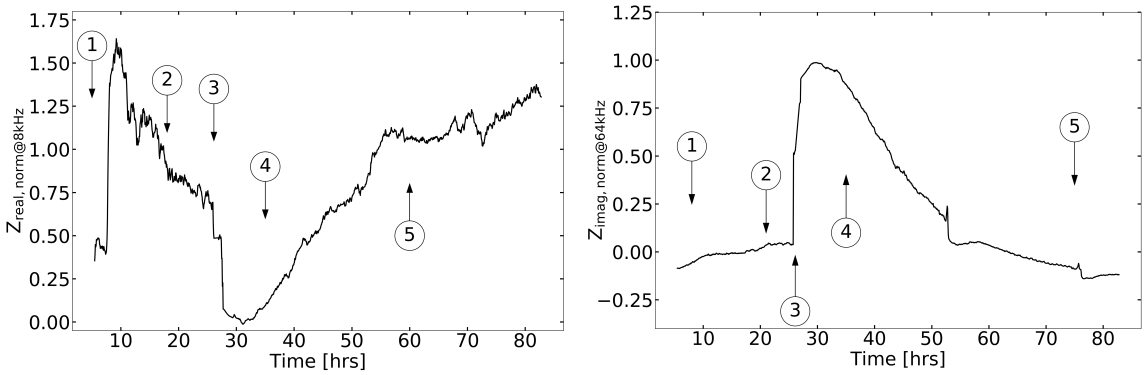

Figure 3.2.: Exemplary trend of the impedance signal measured by an ECIS experiment on 3T3 fibroblasts. The curves show each the real part (left) and the imaginary part (right) of a measured impedance signal. Different phases of the experiment are denoted: (1) seeding of the cells, (2) formation of a monolayer, (3) wounding, (4) recovery and migration into wound and by (5) the initial electrode coverage is restored or even overshot.

3.3. Microfluidics

3.3.1. Microfluidic Channel

For the preparation of microcarriers, we use soft lithography to create a flow focusing PDMS channel with a t-junctional pinch-off to produce single emulsion droplets. This PDMS channel is cast from a lithographically created mask following the preoptimized proportions of [40], also shown in Figure 3.3. A PDMS block containing multiple such channels is then fastened to a microscope slide after oxidising, and thus activating the surfaces of the glass slide and channel in a plasma cleaner (*model of plasma cleaner*) for 20s. This complex is baked at 75°C to foster the bonding of glass and PDMS for at least one hour before being ready to use after cooling down.

3.3.2. The emulsions

The requirements we set for the droplet production according to our design were:

1) **Stimulus responsiveness** to ensure controllability of the content release, here based on temperature,
2) **Non-cytotoxic** for living cell applications, tested via MTS vitality test accessing cellular metabolism,
3) **Low complexity implementation** to provide a "quick and easy" platform for manipulation of cell-experiments (and motivating a medical implementation), as achieved via ECIS micro- and millifluidic combination.

To account for these points we chose to work with Poly(N-isopropylacrylamide) (PNIPAm), a thermo-responsive polymer. PNIPAm is synthesised from the monomer N-isopropylacrylamide (NIPAm) by free-radical polymerisation, the principle of which we discussed in subsection 2.3.2. Its popularity for many applications like

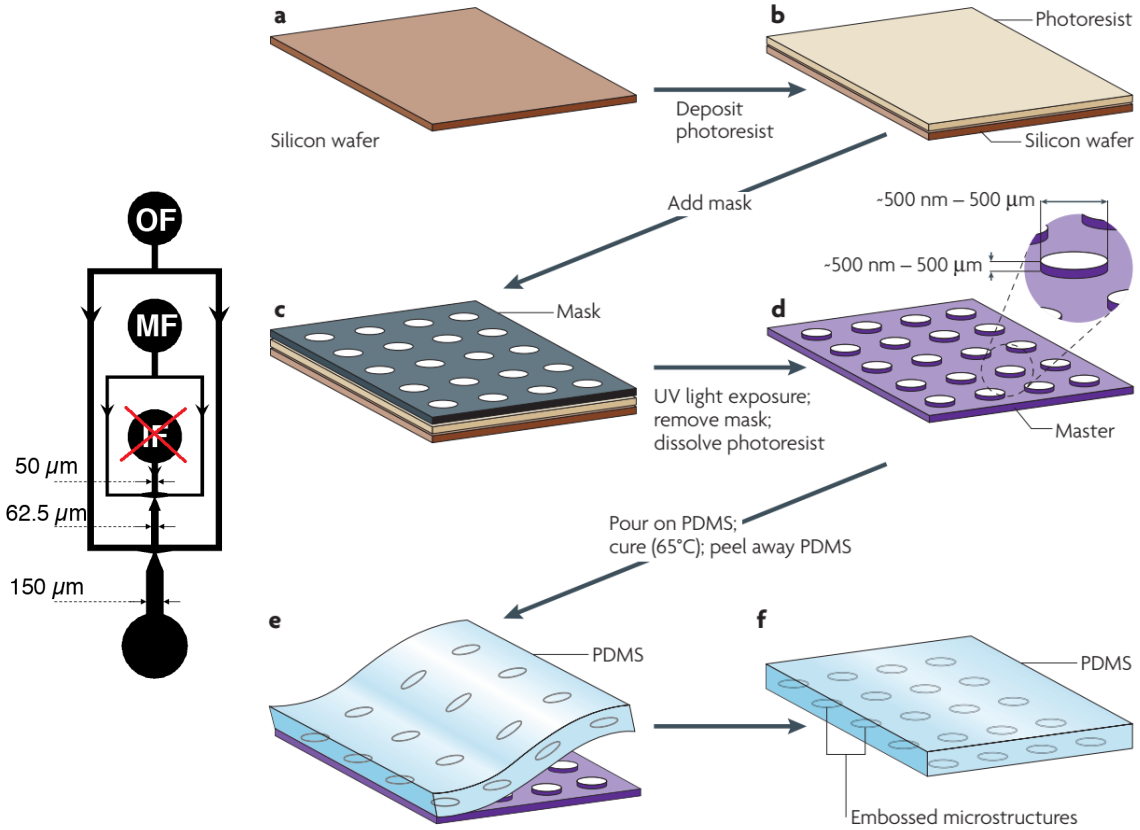

Figure 3.3.: Left: Microfluidic channel design. For the preparation of microcarriers, we use soft lithography to create a flow focusing polydimethylsiloxane (PDMS) channel with a t-junctional pinch-off to produce single emulsion droplets. This PDMS channel is cast from a lithographically created mask following the preoptimized proportions of [40]. Right: Reprinted from [41].

drug delivery and tissue engineering can be attributed to its property to undergo a reversible phase transition close to human body temperature. When solved in water PNIPAm reaches a lower critical solution temperature (LCST) at 32°C and undergoes the aforementioned phase transition above this point. Thereupon the polymer shrinks and dehydrates in contrast to a swollen hydrated state below this temperature. As such, PNIPAm exhibits hydrophobic behaviour in contrast to its state below the LCST. This shrinking behaviour is shown schematically in Figure 3.4 together with its possible use as a carrier system, releasing its content when shrinking due to the increase in temperature. For a single emulsion flow system of Water-in-Oil droplets, two flows are required: a first aqueous solution which the droplet shall be composed of, and an oil-based one dividing the first flow and transporting the droplets into a reservoir. For the aqueous solution we mix varying concentrations of NIPAm monomer, N,N'-Methylenbisacrylamid (BIS) as Crosslinker and Ammonium persulfate (APS) as polymerisation initiator. Also, as PNIPAm is hydrophilic below LCST, we continue using an aqueous solution There are different ways in which to

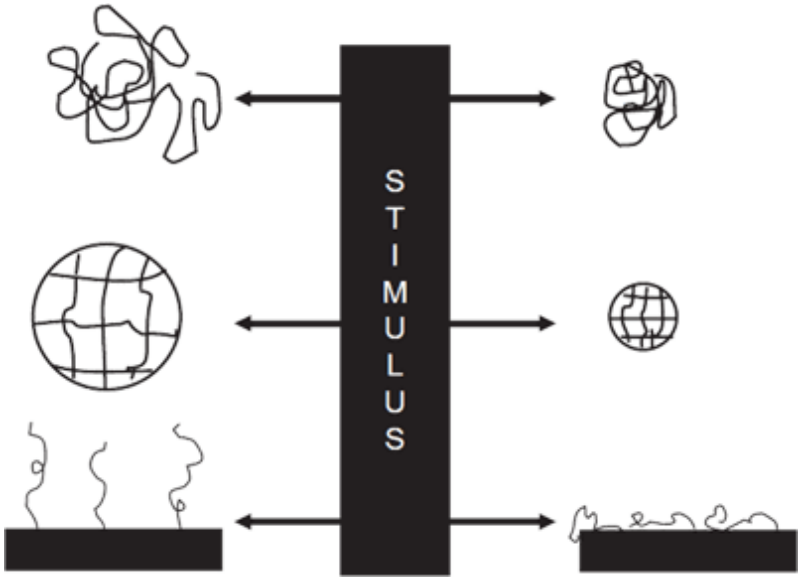

Figure 3.4.: PNIPAm exhibits a typical phase transition when heated above its lower critical solution temperature (LCST) of 32°(stimulus). While hydrated and swollen below LSCT, the polymer shrinks, is therefore dehydrated, and exhibits hydrophobic behaviour above LCST. Schematic adapted from [42].

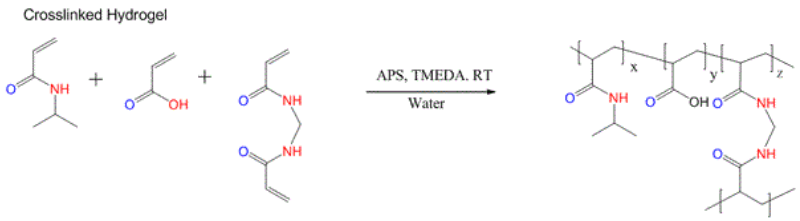

Figure 3.5.: Crosslinking reaction to form a hydrogel from NIPAM monomers with the addition of APS and TEMED [43].

start a polymerisation process one being free-radical polymerisation, a chain-growth polymerisation procedure, see Figure 3.5. As the name suggests, the reaction is started by the presence of free radicals and continues until all monomers have been used up or the reaction is interrupted. These radicals can be formed by a number of different initiating processes, like thermal decomposition, redox reactions, by photolysis, persulfates or ionizing radiation. We have used photolysis and persulfates as initiating agents and will therefore focus on these two mechanisms in the following explanation. The persulfate is solved in the aqueous monomer-containing solution and acts as a radical-source. The process is initiated and sped up by a catalist contained in the reservoir solution, diffusing into the aqueous droplets and reacting with the persulfate contained therein. This sets off a chain reaction of the radical initiator reacting with a new monomer and forming a new radicals until there are no more monomers or the reaction is terminated. But as radicals are highly reactive, chains do not always grow in this controlled way and other mechanisms can occur depending on the initiator concentration at the beginning. If the initiator

concentration is high, many shorter chains will be formed due to the rapid reaction and two active chain ends combine to form a longer chain. Further, interactions with impurities or inhibitors, like oxygen can occur and slow down the polymerisation rate significantly because the oxygen radical is less reactive. During a photolysis process, a chemical compound is broken down by the interactions of one or more photons with the target molecule. In order to start a polymerisation chain, it is necessary to add a photoinitiator to the aqueous solution that creates free radicals upon irradiation with ultraviolett (UV) or visible light. Generally a photoinitiator responds to a specific wavelength regime, but reacts with maximal efficiency only upon irradiation by usually one certain wavelength or a very narrow range around it. In the beginning both methods were used for this work, but with the present experimental setup, chemical polymerisation turned out to be more efficient and was, for this reason, adopted as only polymerisation method. As we used APS as radical initiator, we combined it with a catalyst, Tetramethylethylenediamine (TEMED), which is part of the reservoir,in order to enhance and accelerate the reaction. This is a standard procedure described before in [44]. Alternatively, photolysis is used with macromolecular precursors of the polymer. The longer chain length of the subunits that are to be cross-linked generally leads to a tighter network and smoother surface, while the PCR runs on the same time scale as chemical polymerisation, meaning within seconds. While this approach can be said to give overall nicer polymeric shells, the factor of irradiation with UV-light should not be neglected, especially when encapsulating biomaterial thsat can be changed or damaged by the same. A lot of photoinitiators have absorption spectra overlapping with those of biomaterials, i.e. biomolecules like ATP or even DNA. In such a case the radiation does not only initiate a polymerisation reaction, but also damages the biomolecules to varying degree depending on the duration the molecules were subjected to radiation. Such damage can include structural and functional damage up to a point where the molecule looses its structural integrity completely and is no longer recognizable by functional groups it would normally interact with. This can be avoided by shifting the wavelength required for radical production outside of the absorption spectrum of the encapsulated biomolecules. While this has been proven to be a solid and well functioning method, these dependencies have been a reason to prefer chemical polymerisation for this work as one of the objectives was to use a straight forward and robust system. By using chemical polymerisation we eliminate the varying factor of wavelength shift depending on the cargo's absorption spectrum. To be on the safe side we made a cytotoxicity-test, which showed the droplets to be harmless to the cultures of 3T3 fibroblasts.

3.3.3. Droplet Production

This two-flow set up was used together with a flow pressure pump, which allowed for better control than a typical velocity controlled flow pump. The production was optically controlled by a camera connected to a Leica Microscope and a Monitor. Flow velocity and, therefore, flow conditions and size of droplets was viewed at a sampling rate of 2000pps to adjust flow velocities for the desired droplet size and flow stability as they were generated. Generally, droplets were produced to be around

100µm to avoid the aforementioned influence of curvotaxis or endocytosis by the cells later on. The production protocol can be broken down to three main steps:

1. **Preparation of the solutions.** For that the appropriate concentrations are weighed and solved in deionized water at NIPAM:BIS:APS=9.4:0.6:0.7%(w/v) (on the basis of [44]) as basic solution that was adapted for different conditions. For the oil phase 8%(w/v) Span80 is solved in mineral oil and for the reservoir 10%(w/v) TEMED added to that.
2. **Production of droplets**, usually for approximately 30-60 min. For this the flow setup, chip and reservoir are connected on a microscope for bright field and fluorescent observation.
3. **Washing of the droplets.** Depending on whether the droplets are filled or not they can be centrifuged at 2000 rpm or let rest and sediment over approx. 1h. The fluids are removed from the droplets as much as possible before adding Isopropanol, mixing thoroughly and repeating these steps at least three times. After removing the last isopropanol, 10µl Pluronic F127 are added with water and washed with water two times.

After this they can be either stored in water or in cell medium, which showed no significant degradation of the droplets in comparison to water.
For a better overview of different concentrations used, see section 4.2.

3.4. Atomic Force Microscopy

With the goal of using synthetic carrier system together with cells it is necessary to keep possible interactions in mind. These are not limited to a possible toxicity of the droplets. Depending on the droplet size they are either so small that they are easily taken up endocytotically by the cells together with their content. If the droplets are too large they promote curvotaxis in the cells, which leads to unwanted clustering of cells. But just as important for the way in which polymer shells and cells interact are mechanical properties. As such, the stiffness quantified by the *Young's modulus* E. The Young's modulus can be determined by various methods. One such possible method is the use of a rheological measurement set-up. These set-ups measure the Young's modulus by measuring a materials reaction to different shear strains and are usually the means of choice when regarding hydrogels. Another possibility is the use of optical manipulation contraptions like optical tweezers. Using such a device allows for very precise manipulations and is often used on a macromolecular scale in order to measure single bond strengths when pulling molecules from a cell or folding strengths and dynamics when pulling a single molecule apart. Atomic Force Microscopy (AFM) is another powerful method to measure the Young's modulus. We decided to use AFM for this work, because it allows to measure the polymer shells by themselves and their interaction, possibly adhesion from the cells. The AFM is also used to image samples and can depict sub-nanometer-sized structures, but in this work we focus on the determination of elastic properties. AFM is based on the principle of measuring a force by relation to the deflection of a cantilever arm through a laser spot reflected from the back of this tip to a four-way photodiode. The tip of this cantilever can extend in different shapes towards the

sample, either pyramidal, rounded or without any extension "tip-less" but instead coated with a functionalisation for cell adhesion. The cantilever is mounted on a piezo stage which allows for careful and accurate approach to and retraction from the sample. The resourcefulness of this operating principle becomes especially apparent in combination with *Hooke's Law* and consideration of elastic deformation of materials. For an ideal purely elastic one-dimensional spring, the applied force is directly proportional to the extent of deformation x through a spring constant k, with $F = k \cdot x$. In a non-ideal setting, however, a force is generally applied over a certain area and, as such, a materials behaviour under such a force F per applied area A defines its elastic properties with the *Young's Modulus* E:

$$E = \frac{\sigma}{\epsilon} = \frac{F/A}{\Delta L/L_0} \tag{3.1}$$

, with ΔL the extent of the deformation relative to the materials dimension in rest L_0. This relation is also expressed as the ratio of applied stress σ to strain ϵ of a material and translates to a more general representation of Hooke's Law as:

$$\sigma = E \cdot \epsilon \ . \tag{3.2}$$

In addition the *Poisson's ratio* ν gives a measure to the deformation of a material perpendicular to the applied force with

$$\nu = \frac{\Delta z/z_0}{\Delta x/x_0} = -\frac{\epsilon_{zz}}{\epsilon_{xx}} \ . \tag{3.3}$$

For further analysis of the polymer shells used in this work, a Poisson's ratio of $\nu = 0.5$ was assumed, similar to elastic materials like rubber with $\nu = 0.4999$ [45]. For an AFM, the cantilever indenting an elastic sample is considered as a series of two elastic springs with characteristic spring constant k_{AFM} for the cantilever and an effective spring constant k_{eff} for the sample. While k_{AFM} is a pre-defined constant that is set by manufacture and material, and can be confirmed by calibration measurements, the effective spring constant k_{eff} is the variable to be determined in order to know the Young's modulus of the material. As shown in Figure 3.6 the deformation of the material is derived from the deflection of the laser beam due to dislocation of the cantilever tip recorded through a four quadrant photodiode. A pyrimidal cantilever tip is typically used for such experiments, but in that case corrections have to be considered due to the change in contact area between tip and sample during indentation. As such, the resulting force-distance curve would be non-linear and a simple spring model no longer properly describes the condition. In 1882 the Hertz model was first introduced considering relations between contact area and force holding two elastic bodies together. Eventually a modified Hertz model was

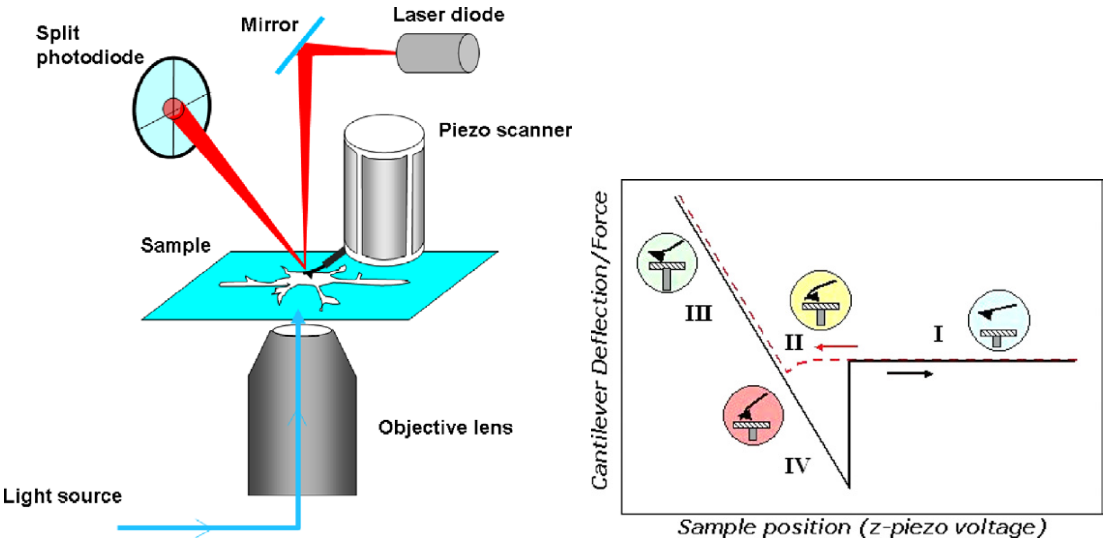

(a) AFM setup with laser beam deflected from a cantilever and recorded by a four quadrant photodiode with an inverted optical bright field microscope for optical adjustment and evaluation.

(b) Schematic of a force-distance curve with approximate cantilever tip positions at characteristic regions.

Figure 3.6.: Adapted from [46].

introduced describing the indentation of an elastic sample by a spherical indenter as

$$F = \frac{4}{3}\frac{E\sqrt{R}}{(1-\nu^2)}\delta^{3/2} \quad (spherical) \tag{3.4}$$

$$F = \frac{2}{\pi}\frac{E\tan\alpha}{(1-\nu^2)}\delta^{2} \quad (conical) \tag{3.5}$$

, with R the probe radius and δ the indentation depth. Accordingly there is a variation for conical probes as well as the Sneddon model, Equation 3.6, describing the indentation by sharp probes with the approximation for a four-sided pyramid as indenter [47]

$$F = 0.7453\frac{E\tan\alpha}{(1-\nu^2)}\delta^{2} \ . \tag{3.6}$$

α represents the averaged half-opening angle of the four-sided pyramid indenter and is therefore a constant of the cantilever provided by the manufacturer. The cantilever tips used for the experiments in this work had $\alpha = 17.5°$. From this the Young's modulus for the PNIPAM shells was determined by fitting recorded force-distance curves of shells at different temperatures to the modified Hertz model implemented in a Matlab script.

4. Results

The following section presents important steps on the way from wound healing and the respective influences of TGF-β1 and formins mDia1 and mDia3 on fibroblasts wound healing, to microfluidic droplet production and their application as carrier system. In this dynamic recovering system we reproduce basic aspects of fibrosis and scar formation. We first consider 3T3 fibroblast cultures of different formin knock out mutants, namely an mDia1 k.o., mDia3 k.o. and an mDia1/3 double k.o. for better comparison. For the impedance experiments we present core parameters determining cell vitality pre, 24 and 48 h post wounding, that were extracted using the model introduced by Lo and Ferrier [34], and further quantify the sigmoidal monolayer recovery, as explained in section 2.2 [48] [16].
This provides a first context for the measurements on 3T3 fibroblasts around TGF-β1 addition and inhibition, that follow an analogous procedure. Such a direct comparison might give insight into a possible treatment of formin-mediated wound healing problems with TGF-β1. To provide the cells with TGF-β1 or its inhibitor efficiently, and simultaneously with a scaffold for stabilisation, we further present the adjusted production procedure of a pNIPAm carrier and the characterisation of its physical properties, mainly its thermal response and elasticity. Finally we will show the resistance and reactance of 3T3 fibroblast cell cultures' wound healing with the addition of the prepared carrier with 15ng TGF-β1.

To this end, Figure 4.1 shows the averaged and normalised resistance for 3T3 fibroblasts, that all results will be compared to. The resistance of unperturbed formation of a monoalayer and its development over 3 days is shown Figure 4.1a as negative control to the wounded monolayer in Figure 4.1b, where wound healing is monitored. As a double negative control, excluding not only wounding but also cells, Figure 4.1a shows the resistance of cell culture medium only. The monolayer was averaged over N=6 electrodes out of n=4 experiments with n_c=3 cell cultures, the culture medium over N=6 and n=n_c=3, and the wild type recovery over N=17, n=9 and n_c=8.

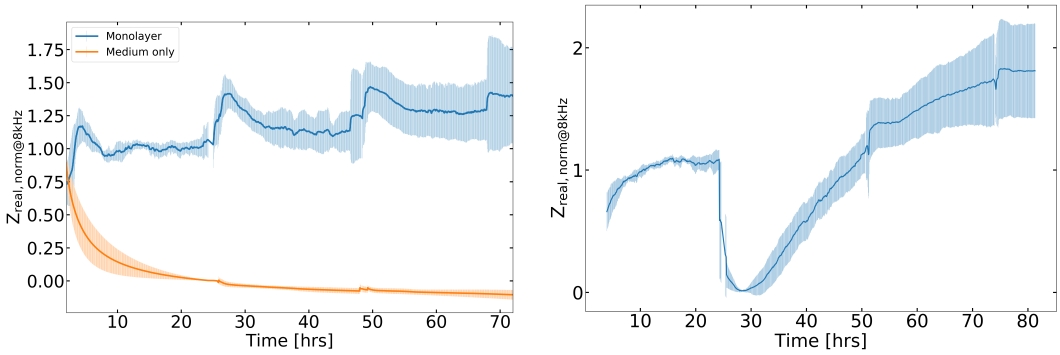

(a) Average resistance from N=6 electrodes out of n=4 experiments with n_c=3 cell cultures for an unperturbed 3T3 fibroblast monolayer over three days (blue), in contrast to the impedance of culture medium (N=6, n=n_c=3).

(b) Average resistance from N=17 electrodes out of n=9 experiments with n_c=8 cell cultures of wild type 3T3 fibroblast, monitoring monolayer formation before wounding(20 h) and subsequent recovery.

Figure 4.1.: Average resistance of the negative (no wounding=monolayer) and double negative (no cells=medium) controls in a) provide a frame of reference for the resistance of a healthy fibroblast monolayer, while b) shows the resistance during wild type fibroblast wound healing.

4.1. Impedance analysis on mDia1, mDia3 in wound healing

In this first set of ECIS experiments, we investigate the influence of fomins mDia1 and mDia3 on the wound healing behaviour of 3T3 fibroblasts, a protein group relevant for actin bundling and capping for polymerisation, involved in rear end myosin dynamics as well as filopodia, and thus for cortical tension but also migration and wound healing. In this context we will consider wound size as variable in addition to protein deletion (k.o.) type and time. Four types of cells are compared: The same wild type 3T3 fibroblast line (blue) as used in all experiments in this work, mDia1 knock out (yellow), mDia3 knock out (green), and mDia1/3 double knock out (red) mutant cells, as depicted in Figure 4.2 and Figure 4.3, and measured on four different sized electrodes corresponding to the wound size of 250 µm, 125 µm, 50 µm and 25 µm. However, over the course of several experiments, the 25 µm electrode yielded only a minimal number of successful experiments where the cells recovered at all, which cannot be quantified using the Lo/Ferrier model due to missing cell-cell contacts and thus R_b contributions, e.g. the electrode being similar in size to the approximate single cell size of 22 µm x 46 µm, an as such, this electrode size will not be considered in further comparisons.
Figure 4.2 and Figure 4.3 show exemplary curves of resistance and reactance respectively of the different cell types for a 250 µm electrode. The mean was taken over a sample of N=17 electrodes out of n=9 experiments with n_c=8 cell cultures for the wild type, and for mDia1 k.o. over N=9, mDia3 k.o. N=12 and mDia1/3 double k.o. N=10, with n=8 with n_c=6 for all formin k.o.. This is the same electrode size that was

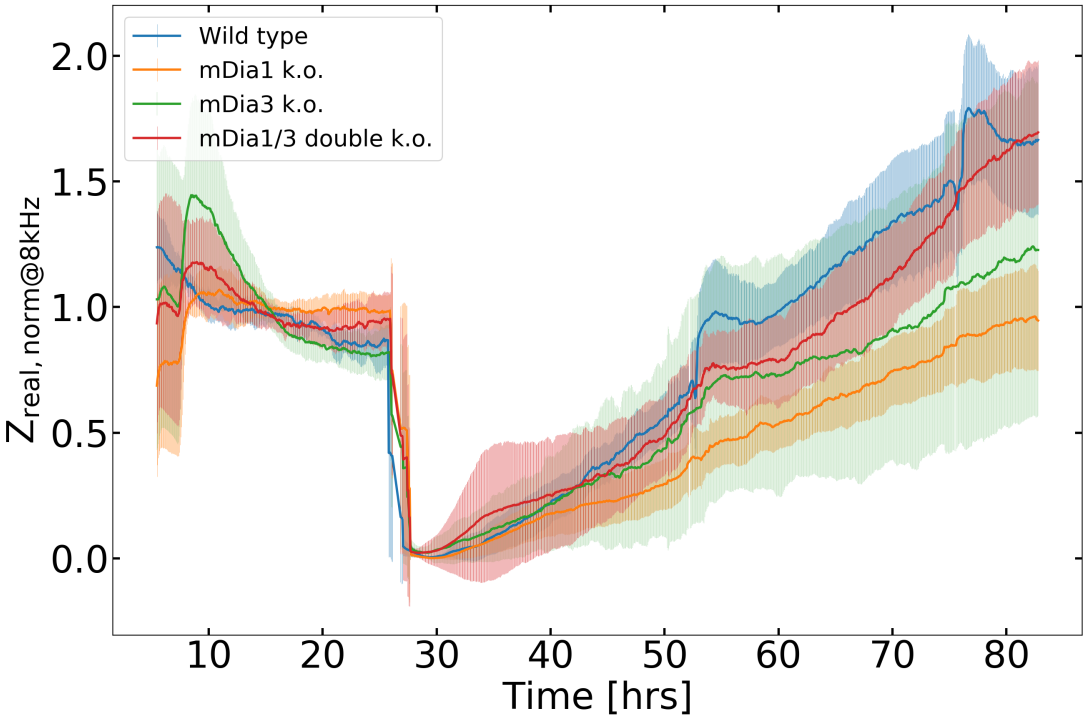

Figure 4.2.: Normalised mean resistance (real part) and standard deviation of measured impedance signals for wild type 3T3 fibroblasts, mDia1, mDia3 k.o and mDia1/3 double k.o. on a 250 µm electrode, thus 250 µm wound. MDia1 k.o cells (yellow) first follow the wild type cells' (blue) response closely up to 40h, then continue their slow and steady rise but never reaching the initial monolayer amplitude. MDia1/3 double k.o. alternates between a steep and a slow, steady rise, in the end catching up to the level of wild type cells overshooting the monolayer amplitude. With N, the total number of electrodes out of n experiments with n_c different cell cultures, for the wild type (N=17): n=9 and n_c=8, and for mDia1 (N=9), mDia3 (N=12) and mDia1/3 (N=10) k.o.: n=8 with n_c=6.

used for all previous and further measurements in **??** and **??** and would seem a good point for later comparisons, but at this point provide an example of the different cell types' trends. From Figure 4.2 we can see that the standard deviation for mDia3 cells grows larger over time due to some curves recovering very slowly and others faster large error and, as such, the mean (green line) can not give us a clear tendency with the error encompassing all other curves including their errors. In contrast to this, the other curves behave more distinctly.
The wild type cells (blue) show the slowest response directly after wounding, together with the mDia1 k.o cells (yellow), but unlike those, the wild type curve rises steeply approximately 20 h after wounding and reaches a comparable pre-wounding amplitude faster than the mutant cell lines, and even overshoots this goal. The mDia1 k.o. curve (yellow) diverges from the wild type after about 40h to rise slowly and steadily with a smaller slope, and never quite recovers the initial monolayer amplitude.

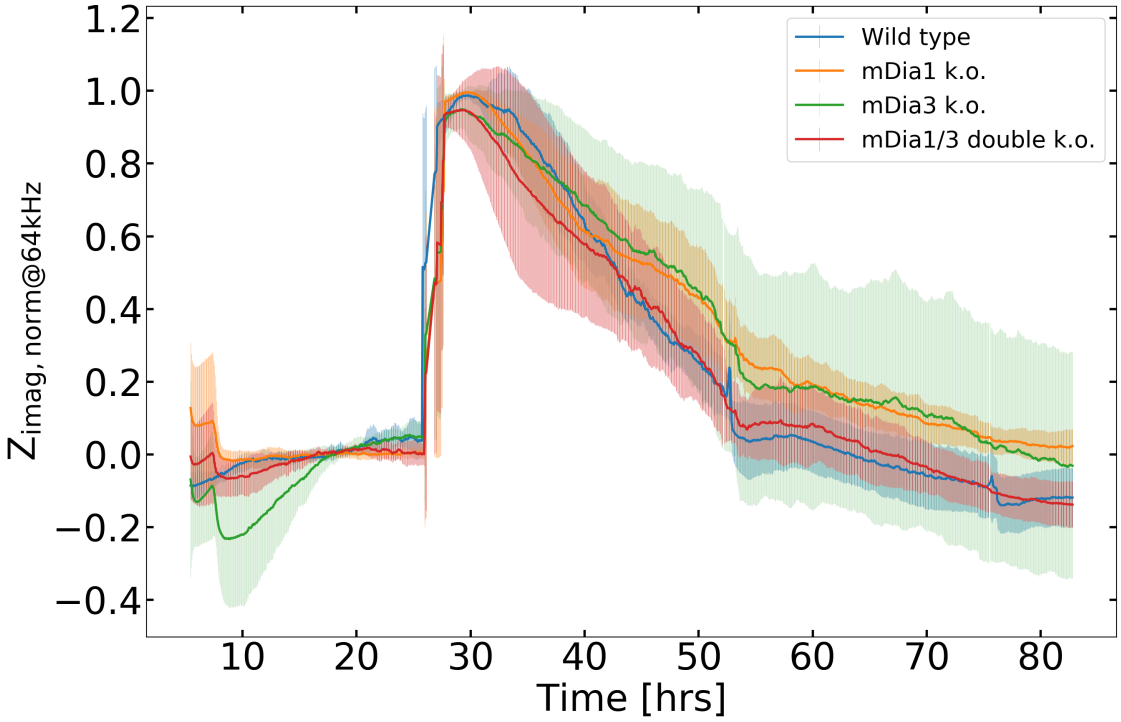

Figure 4.3.: Normalised mean reactance (imaginary part) and standard deviation of measured impedance signals for wild type 3T3 fibroblasts, mDia1, mDia3 k.o and mDia1/3 double k.o. on a 250 µm electrode, thus 250 µm wound. With N, the total number of electrodes out of n experiments with n_c different cell cultures, for the wild type (N=17): n=9 and n_c=8, and for mDia1 (N=9), mDia3 (N=12) and mDia1/3 (N=10) k.o.: n=8 with n_c=6.

Opposed to this steady rise, the curve describing mDia1/3 double k.o cells (red) rather fluctuates in its response. The response time directly after the wounding event is very short and the curve rises almost immediately, only to flatten after 5 to 10h and run parallel to the mDia1 k.o. curve (yellow) for approximately 20 h. At that point, close to 50h, the curve rises steeply, and flattens again for roughly 10h and ultimately rise again until the end of the experiment. By that time the double k.o. curve has not only recovered the initial amplitude, but caught up to the same level as the wild type curve (blue).

Figure 4.3 shows the reactance curves of the different cell types on a 250 µm electrode, complementary to Figure 4.2 with the same statistics mentioned above. This figure, as well, shows the growing error for mDia3 k.o. cells over time. This increase is similarly reflected in the average membrane capacitance C_m, which would be expected because the capacitance is directly derived from the imaginary impedance, as explained in sectionsection 2.2. However, the tendencies seen in Figure 4.2 for mDia1 k.o (yellow) and mDia1/3 k.o (red) in comparison to wild type cells, are also found in this plot. As such, the mDia1 curve reacts slightly faster than the wild type directly after wounding, falls steeply with it up to about 40h until it

flattens and never quite reaches the initial monolayer level. The mDia1/3 double k.o. curve seems to react together with or only slightly fast than the mDia1 curve. They fall together until about 40h of measurement, thus 16h after wounding„ from which point on mDia1/3 and wild type fall together towards the initial monolayer amplitude and slightly below that. In contrast to the resistance curve in Figure 4.2, mDia1/3 double k.o reactance curve does not fluctuate as much in its behaviour during the characteristic phases of the experiment. In summary, formins 1 and 3 do influence the wound healing dynamics of 3T3 fibroblasts, while deleting both apparently is compensated at a certain point by another process.

4.1.1. Evaluation of formin k.o. monolayer properties with Lo model

Characteristic of impedance measurements is the evaluation of cell-cell and cell-substrate dynamics through the junctional resistance R_b, the resistance of the cleft between cell and substrate α which is inversely proportional to the distance between basal membrane and substrate, and the average capacitance of cell membranes C_m. We determine these parameters through the Lo/Ferrier model introduced in subsection 2.2.2, at different times of the experiment to gain insight into dynamic changes in cell vitality and behaviours during wound closure.
Beginning with R_b we will consider each parameter depending on TGF-β1 concentration over time. The Lo/Ferrier model is based on the assumption of a consistent cell monolayer. As such, each parameter was determined for three significant stages of the experiment: the unperturbed monolayer at the beginning of the experiment, a first stage of recovery 24 h after wounding, and close to the end of the experiment 48 h after wounding. For comparability and better statistics, a time interval of three

Diameter	Cell type	N electrodes	n experiments	n_c cultures
250	Wt	12	9	8
	mDia1 k.o.	5	4	4
	mDia3 k.o.	7	6	5
	mDia1/3 d.k.o.	6	6	6
125	Wt	5	4	4
	mDia1 k.o.	5	4	4
	mDia3 k.o.	5	5	4
	mDia1/3 d.k.o.	5	5	5
50	Wt	3	3	3
	mDia1 k.o.	3	3	3
	mDia3 k.o.	0	0	0
	mDia1/3 d.k.o.	3	3	3

Table 4.1.: Statistics for recovery measurements of cell types and electrode size. The number of different cultures is given because two experiments from the same day on different set ups can come from the same cell culture and therefore still be dependent.

	R_b [Ωcm^2]		
	pre	24 h post	48 h post
WT	(3.5±0.9)	(2.1±1.1)	(4.0±1.3)
mDia1 k.o.	(4.0±0.8)	(1.4±0.1)*	(3.6±0.7)
mDia3 k.o.	(3.5±0.3)	(0.72±0.14)***	(1.4±1.3)*
mDia1/3 d. k.o.	(3.4±0.8)	(1.51±0.37)*	(5.6±1.9)

Table 4.2.: Mean R_b over time for different cell types on 250 µm electrodes. With N, the total number of electrodes out of n experiments with n_c different cell cultures, for the wild type N=12: n=9 and n_c=8,and for mDia1 k.o. N=5, n=n_c=4, mDia3 k.o. N=7, n=6, n_c=5 and mDia1/3 N=6 k.o. n=n_c=6. *, **, *** denotes significance with $p<0.05$ and $p<0.001$ respectively.

hours was fitted, typically corresponding to 20 to 23 h for the pre-wounding initial state due to wounding at approx. 24 h, 45 to 48 h for a first recovery, and 69 to 72 h for final recovery representing confluency, repopulation and further differentiation of cells on the electrode. This was possible for most experiments but some could no longer be fitted after 60hrs, implying that the assumptions made no longer properly represent the situation at hand, most likely due to very strong changes in cell morphology, overcrowding or simply cell death; or most likely a combination of these factors. As such R_b, α and C_m were all taken over the following number of electrodes N out of n experiments with n_c cultures.
(Table 4.1): Figure 4.4 shows the distribution of R_b for each cell type over time on a 250 µm electrode, where the only significant deviations from the wild type cells' R_b was found. The corresponding mean R_b are listed in Table 4.2, as significance was determined from the t-test and the assumed normal distribution confirmed.
The respective figures for 125 µm and 50 µm can be found in section B.3, but are not shown here due to only small deviations of low significance in R_b. Looking at R_b before wounding at 20 h, all k.o. cell lines appear to be able to form a monolayer similar to the wild type. Although, no k.o. R_b differs significantly from the wild type, it is interesting to note, that mDia3 R_b is with (3.5±0.3) Ωcm^2 on average slightly smaller than mDia1 R_b with (4.0±0.8) Ωcm^2, thus might form fewer or reduced adherens junctions. Overall, R_b is closed to previously observed 3T3 fibroblast monolayers of around 3 Ωcm^2 or smaller. 24 h after wounding at 45 h, all k.o. cells' R_b are significantly smaller with (1.4±0.1) Ωcm^2 ($p<0.05$) for mDia1 k.o., (0.72±0.14) Ωcm^2 ($p<0.001$) for mDia3 k.o. and (1.51±0.37) Ωcm^2 ($p<0.05$) for mDia1/3 double k.o., in comparison to the already smaller wild type R_b (2.1±1.1) Ωcm^2. In this case, mDia3 R_b shows the greatest divergence from the wild type, which suggests that the recovery of cell-cell contacts is significantly reduced, thus slowing down wound closure. This point is confirmed when looking at R_b 48 h after wounding, when a confluent monolayer should have been recovered and cells further differentiated. At this time after wounding, only R_b of mDia3 k.o.cells is significantly smaller than the wild type R_b of (4.0±1.3) Ωcm^2 with (1.4±1.3) Ωcm^2 , and the only cell line to show a significant difference 48 h after wounding.

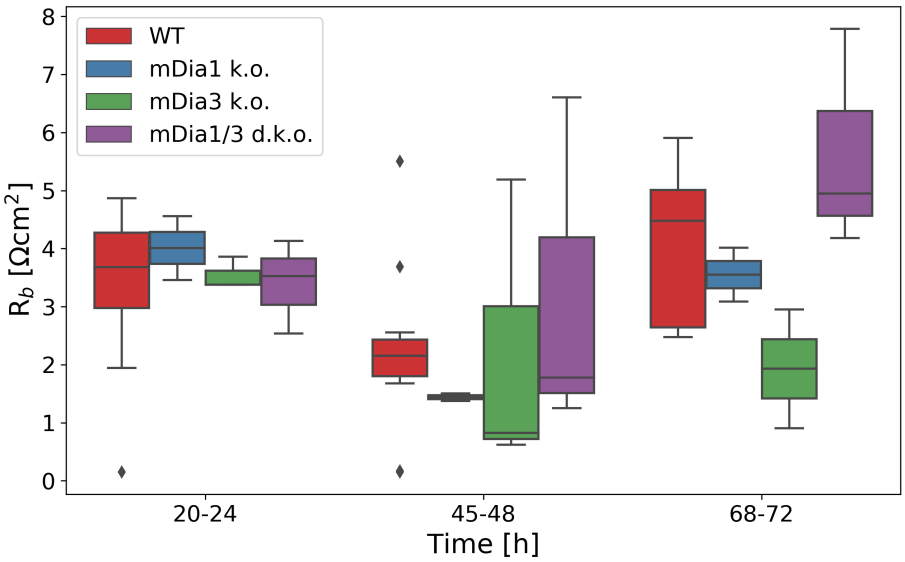

Figure 4.4.: R_b distribution of wild type, mDia1, mDia3 and mDia1/3 double k.o. fibroblasts on 250 µm electrodes over time. During the second phase (24 h after wounding) all formin k.o. cells are significantly smaller than wild type R_b . With N, the total number of electrodes out of n experiments with n_c different cell cultures, for the wild type N=12: n=9 and n_c=8,and for mDia1 k.o. N=5, n=n_c=4, mDia3 k.o. N=7, n=6, n_c=5 and mDia1/3 N=6 k.o. n=n_c=6. *,*** denotes significance with p<0.05 and p<0.001 respectively, ♦ outliers.

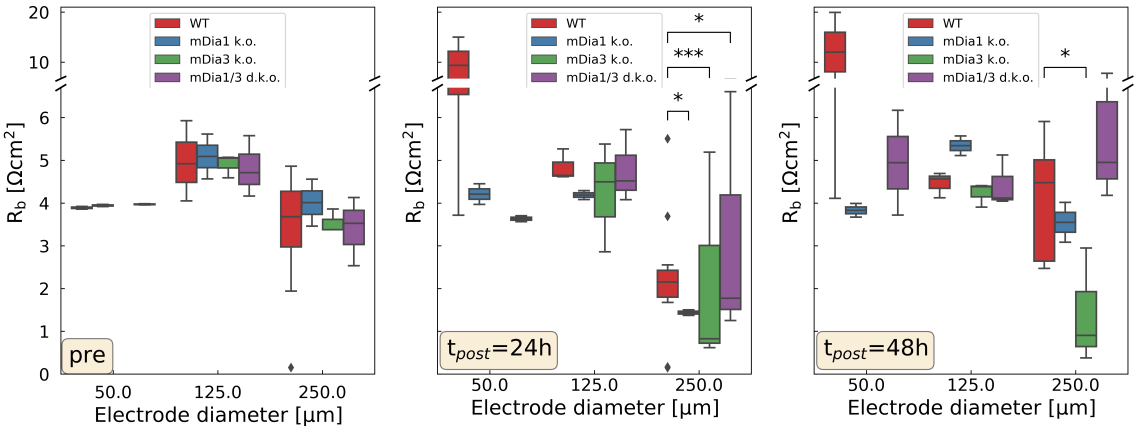

Figure 4.5.: R_b distribution of wild type, mDia1, mDia3 and mDia1/3 double k.o. fibroblasts over electrode diameter for the three phases of the experiment: before wounding, 24 and 48 h after wounding. With N, the total number of electrodes out of n experiments with n_c different cell cultures, for the wild type N=12: n=9 and n_c=8,and for mDia1 k.o. N=5, n=n_c=4, mDia3 k.o. N=7, n=6, n_c=5 and mDia1/3 N=6 k.o. n=n_c=6. *, *** denotes significance with p<0.05 and p<0.001 respectively, ♦ outliers.

The first thing to notice when considering R_b over electrode diameter at different times as shown in Figure 4.5 are the similar R_b before wounding. At this point the different cell types still seem to form similar adherens junctions with the most prominent difference still in mDia3-deleted cells on the 250 µm electrode. However, after wounding they appear to split up and on 125 µm electrodes similar tendencies are observed 24 after wounding as for 250 µm electrodes: All k.o. cells show smaller R_b than the wild type with the double k.o. surprisingly closer to mDia3 k.o. and wild type cells' R_b. 48h after wounding, there is an interesting difference between 125 µm electrodes and 250 µwhich might hint towards different wound healing dynamics. While on 250 µm electrodes mDia3 k.o. cells have significantly smaller R_b and mDia1 and mDia1 and -3 k.o. cells are both more similar to the wild type R_b, on 125 µm electrodes the direct opposite is observed: MDia3 and mDia1- and -3-deleted cells' R_b is closer to the wild type R_b , and mDia1 k.o. cells have higher R_b than the rest.
This means, that the differences due to mDia-family formins 1 and 3 deletion, independently and together, are more pronounced after wounding, thus needing a trigger or being especially important in specific wound healing dynamics. This second implication of an implied differentiation of mDia1 and 3 functionality in wound closure dynamics is further supported by the dependence and variation with electrode diameter.

	α [$\Omega^{1/2}$cm]		
	pre	24 h post	48 h post
WT	(0.12±0.11)	(0.04±0.03)	(0.03±0.02)
mDia1 k.o.	(0.397±0.031)**	(0.008±0.003)	(0.0103±0.0036)
mDia3 k.o.	(0.40±0.08)**	(0.17±0.04)*	(0.1394±0.0003)
mDia1/3 d. k.o.	(0.43±0.18)**	(0.019±0.008)	(0.049±0.048)

Table 4.3.: Mean α over time for different cell types on 250 µm electrodes. With N, the total number of electrodes out of n experiments with n_c different cell cultures, for the wild type N=12: n=9 and n_c=8,and for mDia1 k.o. N=5, n=n_c=4, mDia3 k.o. N=7, n=6, n_c=5 and mDia1/3 N=6 k.o. n=n_c=6. *, ** denotes significance with p<0.05 and p<0.01 respectively.

We will now consider the distribution of α over time before, 24 and 48 h after wounding, shown in Figure 4.6, and the corresponding mean α in Table 4.3.
In contrast to the transcellular permeability R_b , α links to the cell-substrate distance in an inverse proportional fashion. The number of points varies over time, with N, the total number of electrodes out of n experiments, with n_c different cell cultures. An experiment is considered to be a seperate ECIS set up, as such, two experiments on the same day can be done using the same cell culture prepared that day. At 20 h the number of points for wild type cells is N=17 (n=9, n_c=8), for mDia1 k.o. N=9, mDia3 k.o. N=12 and mDia1/3 double k.o. N=10 with(n=8, n_c=6) for all k.o. cells. At 45 h wild type cell statistics is equal to 20 h, while for mDia1 k.o. N=7, mDia 3 k.o. N=9 and mDia1/3 double k.o. N=7 with (n=6, n_c=5), and at 72

h: wild type N=10 (n=5, nc=5), mDia1 k.o. N=n=n_c=4, mDia 3 k.o. N=n=n_c=4 and mDia1/3 double k.o. N=n=n_c=3.

Figure 4.6 shows distinctly that wild type cells' α drops after wounding from

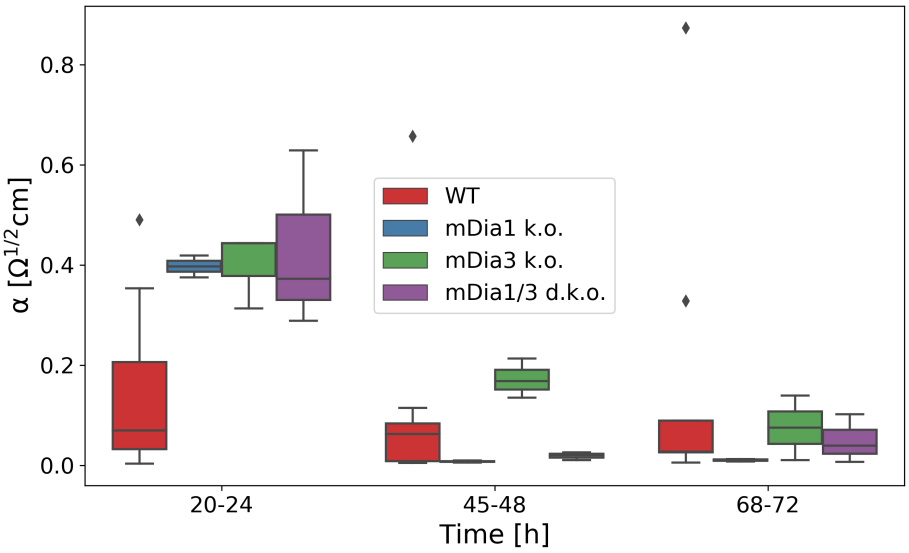

Figure 4.6.: α distribution of wild type, mDia1, mDia3 and mDia1/3 double k.o. fibroblasts on 250 µm electrodes over time. After wounding only mDia3 k.o. α is significantly higher than wild type α, in contrast to all formin k.o. before wounding. With N, the total number of electrodes out of n experiments with n_c different cell cultures, for the wild type N=12: n=9 and n_c=8,and for mDia1 k.o. N=5, n=n_c=4, mDia3 k.o. N=7, n=6, n_c=5 and mDia1/3 N=6 k.o. n=n_c=6. *, ** denotes significance with $p<0.05$ and $p<0.01$ respectively, ♦ outliers.

(0.12±0.11) $\Omega^{1/2}$cm before to (0.04±0.03) $\Omega^{1/2}$cm and (0.03±0.02) $\Omega^{1/2}$cm over the course of the experiments, indicating that cell-substrate distance increases after wounding and stays constant afterwards. Similarly, mDia3-deleted α is significantly higher before wounding with (0.40±0.08) $\Omega^{1/2}$cm and becomes smaller afterwards with (0.17±0.04) $\Omega^{1/2}$cm and (0.1394±0.0003) $\Omega^{1/2}$cm, showing a decrease also seen in mDia1 k.o. α. Neither mDia1 nor mDia1/3 double k.o. show a different behaviour after wounding, only that α for all k.o. cell lines is significantly higher with (0.397±0.031) $\Omega^{1/2}$cm , (0.40±0.08) $\Omega^{1/2}$cm and (0.43±0.18) $\Omega^{1/2}$cm ($p<0.01$) than for the wild type α with (0.12±0.11), meaning that cell-substrate interaction is perturbed during monolayer formation. Because α is inversely proportional to the height of the basal cell membrane above the substrate, higher *alpha* indicates that the cell is closer to the substrate, thus the k.o. cells seem to adhere closer to the surface than the wild type cells.

24 h after wounding, α of mDia1 and mDia1/3 double k.o. cells drops to a level comparable to the wild type cells, while in the mDia3 k.o. α is still significantly higher with (0.17±0.04) $\Omega^{1/2}$cm ($p<0.05$) compared to (0.04±0.03) $\Omega^{1/2}$cm.

48 h after wounding, a clear distinction is not possible for any celltype, although mDia3 k.o. α seems slightly higher, but for a concrete statement more experiments are required.

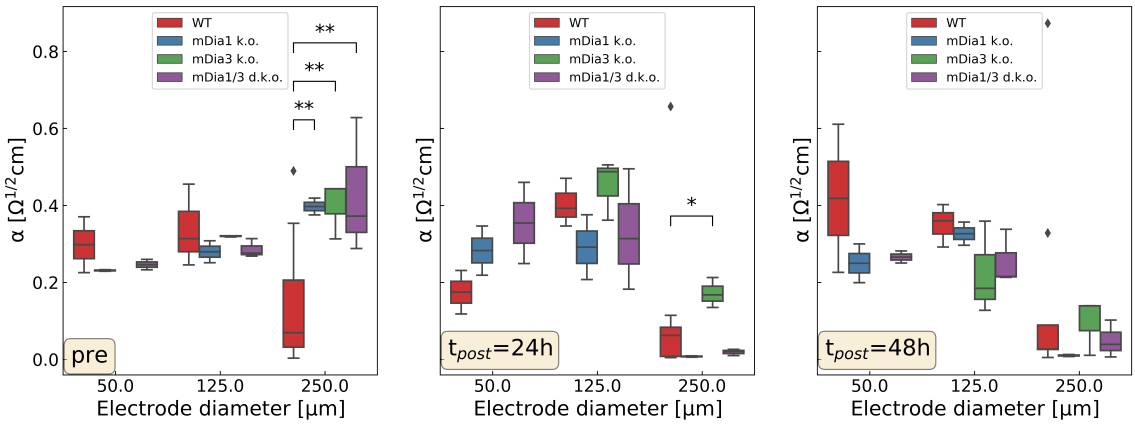

Figure 4.7.: Average α of wild type, mDia1, mDia3 and mDia1/3 double k.o. fibroblasts over electrode diameter for the three phases of the experiment: before wounding, 24 and 48 h after wounding. With N, the total number of electrodes out of n experiments with n_c different cell cultures, for the wild type N=12: n=9 and n_c=8,and for mDia1 k.o. N=5, n=n_c=4, mDia3 k.o. N=7, n=6, n_c=5 and mDia1/3 N=6 k.o. n=n_c=6. *, ** denotes significance with p<0.05 and p<0.01 respectively, ♦ outliers.

Figure 4.7 shows α over different electrode diameters before, 21-24 h and 45-48 h after wounding. From this we find that α as well changes with the electrode size and time. While there is a strong difference between wild type α and that of all formin-deleted cell types on 250 µm electrodes before wounding, the same is cannot be said for 50 and 125 µm electrodes, where all α are closer together. However, 24 h after wounding similar tendencies are observed on 125 µm and 250 µm electrodes, which seem to be more strongly pronounced on the bigger electrode.
48 h after wounding this similarity changes especially in the mDia3 k.o. and mDia1 and -3 double k.o. α and both of theses results are clearly below wild type α on 125 µm electrodes, while on 250 µm both celltype's α appear to be equal to or slightly higher than the wild type while mDia1 k.o. α is smaller.
The smallest electrode of 50 µstands in direct contrast to this as not only is mDia1 k.o. α higher than that of wild type cells, but also the double k.o. has a higher α than both other celltypes.
These variations with electrode size appear to be also time-dependent which further supports the implications gleaned from R_b over electrode size in Figure 4.5 on a possible distinction of wound size-dependent healing dynamics.

The last parameter to consider for this line of analysis is the average capacitance of cell membranes C_m. Figure 4.8 shows the averaged C_m fit results before, 24 and 48 h after wounding, analogous to R_b and α, with the same statistics mentioned above. The wild type C_m displays results in an expected regime of 10^{-6} Fcm^{-2}, with the notable exception of several results around 10^{-5} before wounding. Already before wounding the mean C_m (Table 4.4) for mDia1 and mDia3 k.o. is significantly smaller than the wild type C_m (3.5±0.9) µFcm^{-2} with (1.10±0.22) µFcm^{-2} (p<0.05) and

	C_m [µFcm^{-2}]		
	pre	24 h post	48 h post
WT	(0.35±0.09)	(0.21±0.11)	(0.40±0.13)
mDia1 k.o.	(0.110±0.022)*	(0.17±0.03)	(0.1062±0.0021)
mDia3 k.o.	(0.12±0.06)**	(0.97±0.32)**	(0.78±0.01)
mDia1/3 d. k.o.	(0.36±0.05)	(0.18±0.03)	(0.99±0.09)

Table 4.4.: Mean C_m over time for different cell types on 250 µm electrodes. With N, the total number of electrodes out of n experiments with n_c different cell cultures, for the wild type N=12: n=9 and n_c=8,and for mDia1 k.o. N=5, n=n_c=4, mDia3 k.o. N=7, n=6, n_c=5 and mDia1/3 N=6 k.o. n=n_c=6. *, ** denotes significance with p<0.05 and p<0.01 respectively.

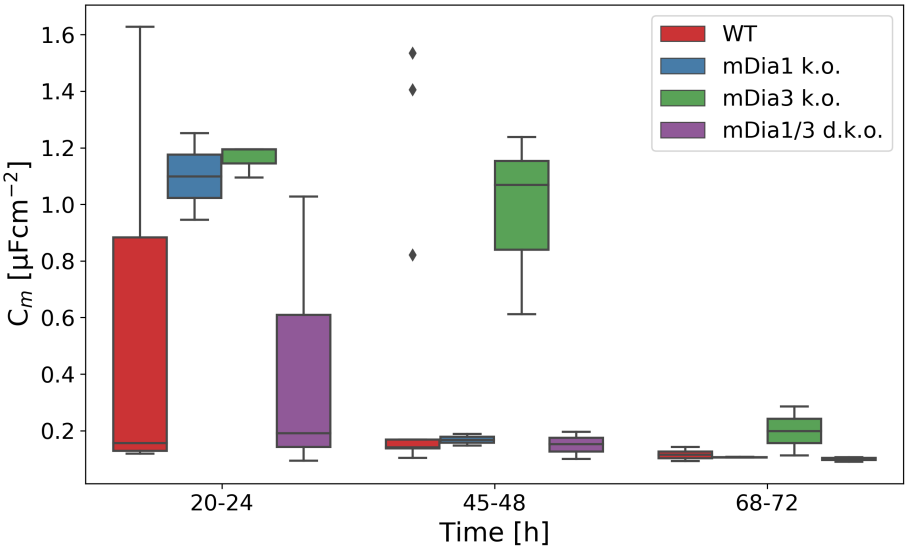

Figure 4.8.: C_m distribution of wild type, mDia1, mDia3 and mDia1/3 double k.o. fibroblasts on 250 µm electrodes over time. After wounding only mDia3 k.o. C_m is significantly higher than wild type C_m , in contrast to mDia1 and mDia3 k.o. before wounding. With N, the total number of electrodes out of n experiments with n_c different cell cultures, for the wild type N=12: n=9 and n_c=8,and for mDia1 k.o. N=5, n=n_c=4, mDia3 k.o. N=7, n=6, n_c=5 and mDia1/3 N=6 k.o. n=n_c=6. *, ** denotes significance with p<0.05 and p<0.01 respectively, ♦ outliers.

(1.2±0.6) µFcm^{-2} (p<0.01) respectively, thus with a smaller membrane surface. Interestingly, the mDia1/3 double k.o. C_m resembles the wild type C_m most judging by Figure 4.8 and Figure 4.9, but considering the effective mean values in Table 4.4 this cannot be confirmed. Considering the first phase 24 h after wounding, mDia3 k.o. C_m is significantly higher with (9.7±3.2) µFcm^{-2} (p<0.01) than wild type C_m , while mDia1 k.o. and mDia1/3 double k.o. are on the same level with (1.7±0.3) µFcm^{-2} and (1.8±0.3) µFcm^{-2} respectively. The large distribution of mDia3 k.o. C_m due to a split in several high and low values is not meaningful at

this point and would require more experiments. This increasing uncertainty stems directly from the imaginary impedance and is reflected in the reactance, as seen before in Figure 4.3.

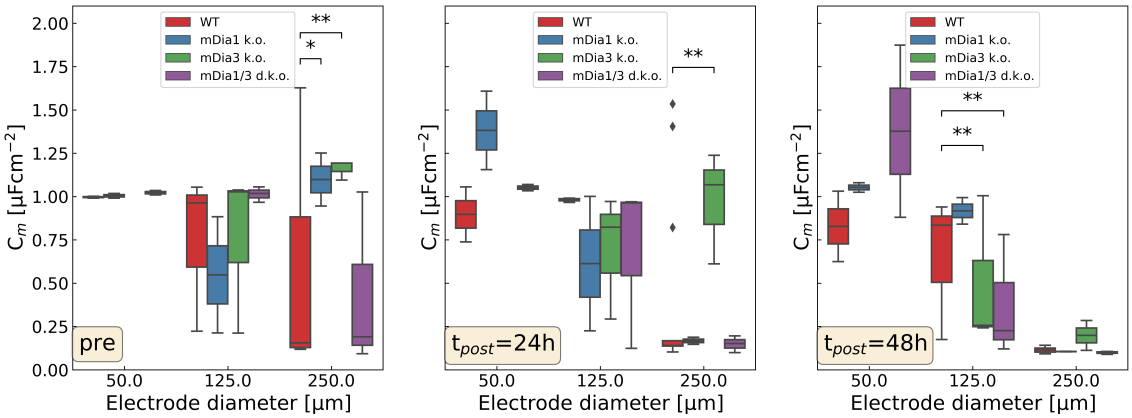

Figure 4.9.: Averaged C_m of wild type, mDia1, mDia3 and mDia1/3 double k.o. fibroblasts over electrode diameter for the three phases of the experiment: before wounding, 24 and 48 h after wounding. In contrast to higher mDia3 k.o. C_m 24 h after wounding on 250 µm electrodes, on 125 µm there is no significant deviation, until 48 h after wounding, where mDia3 and mDia1/3 double k.o. C_m is smaller. With N, the total number of electrodes out of n experiments with n_c different cell cultures, for the wild type N=12: n=9 and n_c=8,and for mDia1 k.o. N=5, n=n_c=4, mDia3 k.o. N=7, n=6, n_c=5 and mDia1/3 N=6 k.o. n=n_c=6. *, ** denotes significance with $p<0.05$ and $p<0.01$ respectively, ♦ outliers.

Looking at C_m for different electrode sizes over time, there seems be slightly different behaviour in mDia3 k.o. cells on 125 µm electrodes than on 250 µm. While mDia3 k.o. C_m was significantly higher before and 24 h after wounding on 250 µm electrodes, on 125 µm C_m is on one level with wild type C_m , maybe even slightly smaller 24 h after wounding. Additionally, 48 h after wounding, mDia3 and mDia1/3 double k.o. C_m are significantly smaller on 125 µm electrodes with (2.5±0.1) µFcm^{-2} ($p<0.01$) and (1.74±0.74) µFcm^{-2} ($p<0.01$) compared to wild type C_m with (8.88±0.75) µFcm^{-2}. This suggests, that for smaller electrodes of 125 µm, the capacitance, and thus the membrane surface, is not as strongly impacted as for larger wounds with 250 µm, and only later during the third phase where cells differentiate further, membrane capacity is significantly smaller. As mDia3 and mDia1/3 double k.o. are affected, while mDia1 k.o. shows no similar tendency, mDia3 appears to have a slightly different role in fibroblast wound healing depending on the wound size.

In summary, strong changes in R_b, α and C_m can be observed, especially for the mDia3 k.o. cells: The higher α, thus closer cell-substrate distance, together with a significantly higher C_m 24 h after wounding and the larger divergence 48 h later, suggesting an increase in membrane surface or change in lipid composition, hints

towards stronger morphological variations due to the deletion of mDia3.

4.1.2. Recovery time

Next to the fit parameters R_b, α and C_m monitoring cell vitality, two other parameters that might be informative are the recovery time towards half of the initial signal $t_{1/2}$ and the rate at which this recovery happens $r_{1/2}$. These values are results from fitting the sigmoidal function (Equation 4.1) to a recovery interval of a resistance curve using the curve.

$$y(t) = A_0 + \left\{ \frac{A_{max}}{\left(1 + \exp\left(\frac{t_{half} - t}{r_{1/2}}\right)\right)} \right\} \tag{4.1}$$

The interval was chosen between typically a curve minimum, and the point where a quasistationary equilibrium was recovered, e.g. if the initial amplitude was not reached, the interval was chosen up to the the post-wounding maximum of a curve. The half point recovery time $t_{1/2}$ and respective recovery rate $r_{1/2}$ are extracted to gain dynamic information about the wounding contribution of formins, besides parameters R_b, α and C_m monitoring general cell vitality. In Table 4.10 the averaged results for $t_{1/2}$ and $r_{1/2}$ extracted from this sigmoidal fit are shown for each k.o. for 250 µm, 125 µm and 50 µm electrode diameter, with the corresponding statistics for total electrode number N from n experiments with n_c different cell cultures listed in Table 4.5. Figure 4.10 shows the half point time $t_{1/2}$ in its variation over different

Diameter	Cell type	N electrodes	n experiments	n_c cultures
250	wild type	17	9	8
	mDia1 k.o.	9	8	6
	mDia3 k.o.	12	8	6
	mDia1/3 d.k.o.	10	8	6
125	wild type	7	4	4
	mDia1 k.o.	9	8	6
	mDia3 k.o.	12	8	6
	mDia1/3 d.k.o.	9	7	6
50	wild type	4	3	3
	mDia1 k.o.	8	5	5
	mDia3 k.o.	6	5	3
	mDia1/3 d.k.o.	5	5	5

Table 4.5.: Statistics for recovery measurements of cell types and electrode size. The number of different cultures is given because two experiments from the same day on different set ups can come from the same cell culture and therefore still be dependent.

electrode, and wound, diameters, the corresponding results for $t_{1/2}$ and $r_{1/2}$ are

Cell type	250 µm		125 µm	
	$t_{1/2}$ [h]	$r_{1/2}$ [1/h]	$t_{1/2}$ [h]	$r_{1/2}$ [1/h]
wild type	(15.3±3.0)	(4.6±1.2)	(14±3)	(2.4±1.4)
mDia1 k.o.	(26±8)*	(12.4±3.2)****	(20±5)*	(5.2±2.1)*
mDia3 k.o.	(23.5±8.2)*	(9.0±5.6)	(15±5)	(3±1)
mDia1/3 d.k.o.	(20±6)	(5±2)	(14±6)	(3.2±1.2)

Cell type	50 µm	
	$t_{1/2}$ [h]	$r_{1/2}$ [1/h]
wild type	(9±3)	(1.6±0.9)
mDia1 k.o.	(16±7)	(3.8±2.1)
mDia3 k.o.	(11±3)	(2.4±1.3)
mDia1/3 d.k.o.	(16±5)	(3.4±1.9)

Table 4.6.: Averaged $t_{1/2}$ and $r_{1/2}$ results from sigmoidal fit for different concentrations. '*' denotes respective significant deviation from wild type cells. With N, the total number of electrodes out of n experiments with n_c different cell cultures, for the wild type (N=17): n=9 and n_c=8,and for mDia1 (N=9), mDia3 (N=12) and mDia1/3 (N=10) k.o.: n=8 with n_c=6.

listed in Table 4.6. Table 4.5 lists the statistics for the evaluation of recovery time and rate with N, the number of total electrodes out of n experiments with n_c cell cultures. At first glance we can tell that $t_{1/2}$ rises with increasing diameter from 50 µm to 250 µm for all cell celltypes, which would be expected for increasing wound size. Overall, the k.o. $t_{1/2}$ appear to be higher than the wild type $t_{1/2}$, thus taking longer to recover half the initial monolayer amplitude and with that taking longer to close the wound. Between the k.o. cells, the mDia1 k.o. $t_{1/2}$ is gernerally the largest, differing from the wild type $t_{1/2}$ of (14.3±3) with (20±5)h ($p<0.05$) and mDia3 $t_{1/2}$ with (15±5) ($p<0.05$) for 125 µm, and with (26.8±8) ($p<0.05$) from the wild type $t_{1/2}$ of (15.3±3.0) on 250 µm electrodes. Although the mDia3 k.o. $t_{1/2}$ is only slightly higher than the wild type on 125 µm, it is more so 250 µm electrodes with (23.5±8.2) ($p<0.05$).
However, mDia1/3 double k.o. shows a slight divergence from this pattern on 125 µm electrodes, where $t_{1/2}$ remains equal to $t_{1/2}$ for 50 µm or slightly smaller which might resemble an adjustment in the way cells migrate into the wounded area. This implication is reinforced by the impression that on 50 µm electrodes mDia1/3 $t_{1/2}$ resembles the mDia1 $t_{1/2}$, while on 250 µm electrodes mDia1/3 $t_{1/2}$ is level with mDia3 k.o $t_{1/2}$.
In summary, the recovery half time $t_{1/2}$ tends to be higher for formin k.o. cells, thus the recovery of a quasistationary state, and with that wound healing, takes longer. That this is especially the case for mDia1 k.o. cells, while mDia3 k.o. seem to be able to compensate this effect up to 125 µm, diverging significantly for 250 µm wound size, indicates that mDia1 might play a more important role in fibroblast

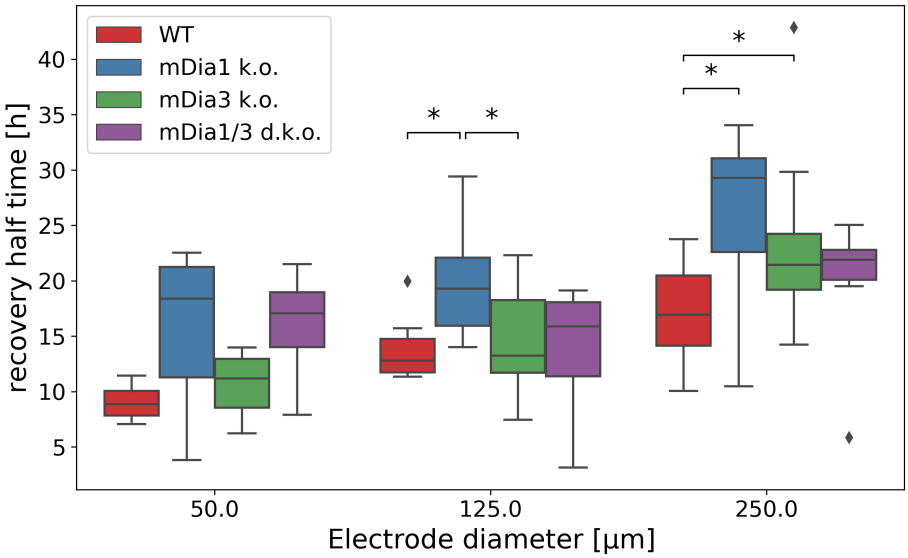

Figure 4.10.: Half point recovery time $t_{1/2}$ over different electrode diameters for wild type fibroblasts (circle), mDia1 k.o (downward triangle), mDia3 k.o. (upward triangle) and mDia1/3 double k.o. (square) mutants. From 50 µm to 250 µm $t_{1/2}$ overall increases with wound (electrode) size, but there is a dip for all cell types at 125 µm before $t_{1/2}$ rises again. With N, the total number of electrodes out of n experiments with n_c different cell cultures, for the wild type (N=17): n=9 and n_c=8,and for mDia1 (N=9), mDia3 (N=12) and mDia1/3 (N=10) k.o.: n=8 with n_c=6. * denotes significance with p<0.05, ♦ outliers.

migration into the wound than mDia3.

Looking not only at recovery time but also rate, provides insight into how fast cells repopulate the electrode, thus migrate into the wounded area. This recovery rate $r_{1/2}$ is shown in Figure 4.11 over varying electrode diameter for the different cell types on the basis of the statistics listed in Table 4.5. Similar to $t_{1/2}$, $r_{1/2}$ increases with electrode diameter for all cell types, like for wild type cells from (1.6±0.9)h on 50 µm electrodes to (2.4±1.4)h on 125 µm electrodes to (4.6±1.2)h on 250 µm, which would mean, that fibroblasts move faster to close the wound proportional to wound diameter. The tendency for slower recovery of mDia1 k.o. cells seen in the recovery time, is not confirmed with the increasingly higher mDia1 k.o. $r_{1/2}$ with (5.2±2.1) (p<0.05) in comparison to the wild type $r_{1/2}$ (2.4±1.4)h on 125 µm, and (12.4±3.2) (p<0.0001) to (4.6±1.2)h on 250 µm electrodes. MDia3 and mDia1/3 k.o do not appear to have such a strong impact on the recovery rate, as their $r_{1/2}$ is on the same level as the wild type $r_{1/2}$. This means that while the mDia3 and mDia1/3 k.o. cells take longer than the wild type to close a wound of 250 µm and form a confluent monolayer, they do so at similar rates as the wild type, implying a slower response after wounding. Especially pronounced is this varying impact of mDia1 and mDia3 on the 125 µm electrode with mDia1 k.o. $r_{1/2}$ (5.2±2.1)h and mDia3 k.o. $r_{1/2}$ (3.2±1) (p<0.05), and on 250 µm electrodes for mDia1 and mDia1/3 double k.o. rates (26±8)h and (20±6)h (p<0.001). Such a strong divergence of mDia1/3 double k.o. $r_{1/2}$ to mDia1 k.o., and being equal to the wild type $r_{1/2}$ suggests that

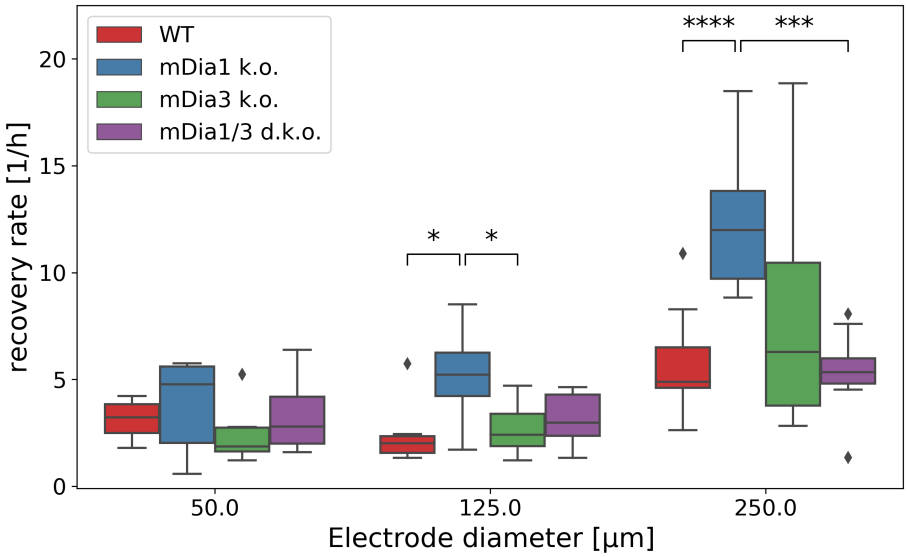

Figure 4.11.: Cell recovery rate $r_{1/2}$ over different electrode diameters for wild type fibroblasts (circle), mDia1 k.o (downward triangle), mDia3 k.o. (upward triangle) and mDia1/3 double k.o. (square) mutants. Despite few irregularities in $t_{1/2}$ for the smaller electrodes in mDia1 and mDia1/3 k.0. behaviour, there is a clear tendency for larger $t_{1/2}$ with increasing wound (electrode) size. With N, the total number of electrodes out of n experiments with n_c different cell cultures, for the wild type (N=17): n=9 and n_c=8,and for mDia1 (N=9), mDia3 (N=12) and mDia1/3 (N=10) k.o.: n=8 with n_c=6. *, ***, **** denotes significance with p<0.05, p<0.001 and p<0.0001 respectively, ♦ outliers.

some compensation mechanism is employed to counter the loss of both formins.
In summary, $t_{1/2}$ results suggest a slower wound healing for formin k.o. cells than wild type, especially for mDia1 deletion. This is supported by mDia1 $r_{1/2}$ being significantly higher, and thus wound healing takes longer in parts due to a significantly higher recovery rate, reinforcing that mDia1 appears to play a more important role in fibroblasts' migration dynamics into the wounded area. MDia3 k.o. cells also recovered slower than the wild type on 250 µm electrodes but with similar rates as the wild type, which means that there is a distinct lag during the initial response phase after wounding. Taking both observations into account, it appears as though mDia1 plays a critical role in driving migration and thus wound closure once the cells move, hence mDia1 k.o. cells are slower overall not seen as strongly in mDia3k.o., while mDia3 seems to be critical for initiating and organising cell response, hence the slower response in mDia3 k.o. not present in mDia1 k.o. cells. This might also be an interesting point scrutiny: whether this response lag can be countered by the use of pNIPAm polymerosomes as scaffold, promoting cell polarisation, and carrier of TGF-β1. However, in what ways the mDia1/3 double k.o. manages to compensate the deleted mDia1 for most parts, is not possible to determine from these observations and might need further investigation.

4.2. Impedance analysis on TGF-β1 in wound healing

Of the two sets of measurements done to investigate influences on wound healing, this second part focusses on TGF-β1 and how its reduced production or enrichment through addition of either a TGF-β1 inhibitor (ALK5 receptor) or TGF-β1 accelerates or delays healing, respectively. These measurements were performed on a wild type 3T3 fibroblast cell line, as introduced in section 3.1 with additional TGF-β1 concentrations of 2.5ng, 5ng, 10ng, 15ng and 25ng. The order of magnitude for the concentration likely to achieve a response from the cells was approximated from previous measurements on the epithelial-to-mesenchymal transition [49]. An equally distinct approximation could not be made for the ALK5 inhibitor due to widely different concentrations found in the literature ranging from 5ng IC_{50} for TGF-β-induced epithelial-to-mesenchymal transition [50] to 400ng to inhibit profibrotic signaling in fibroblasts. [51]. As a result of this we chose to vary the inhibitor concentration over a wider range of 5ng, 10ng, 15ng, 100ng and 200ng.
The inhibitor A83-01(AdooQ Bioscience) targets the activin-like receptor kinase 5 (ALK5) selectively inhibiting the TGF-βreceptor-coupled Smad pathway, the main signaling pathway for TGF-β1, and the Nodal receptor ALK4 and ALK7. In the following tables an inhibitor concentration is denoted as negative concentration. This has no quantitative relevance and serves only to simplify the notation and clarify concentration-dependent plots.

From these different concentrations, the most relevant ones, showing a representative behaviour, are shown in Figure 4.12 and Figure 4.13 as 10ng inhibitor (red), 5ng (orange, N=4, 2 experiments, 1 cell culture) and 15ng (green) additional TGF-β1 in comparison to a an uninfluenced control group (blue). A summary of curves for all concentrations can be found in Appendixsection B.3 together with a summary of performed experiments.

Each curve represents the mean over all measurements (thick line) for that concentration and the respective standard deviation (shaded errorbars). The mean was taken for each concentration of N total electrodes out of n experiments with n_c cell cultures: for unperturbed cells N=17, n=9, n_c=8, for 5ng additional TGF-β1 N=4, n=2, n=2, for 15ng additional TGF-β1 N=4, n=2, n=2 and for 10ng inhibitor N=8, n=4, n_c=3. Figure 4.12 shows the progression of the real part of the measured impedance signal, the resistance, over the course of the course of three days and evaluated for a frequency of 8kHz for the best signal-to-noise ratio. The data averaged for these curves was recorded during different experiments leading to differences in timing most notably wounding time, seeding of cells and feeding, and further showed strong differences in amplitudes, and as such was normalised so that a monolayer formed over approximately 24 h at the beginning of the experiment corresponds to a value of 1.0, and the signal at the point of and directly after wounding to 0.0. If we accept the control group as recovery behaviour typical for 3T3 fibroblast, one can immediately see that the 10ng of ALK5 inhibitor on average do not significantly change. It should be noted at this point, that neither the control group nor the inhibitor group recover the intial monolayer amplitude and instead find a steady state at about 0.75. The large error of this inhibitor curve especially during the second day of recovery (at approx 50hrs) is representative of the strongly fluctuating response to the inhibitor.

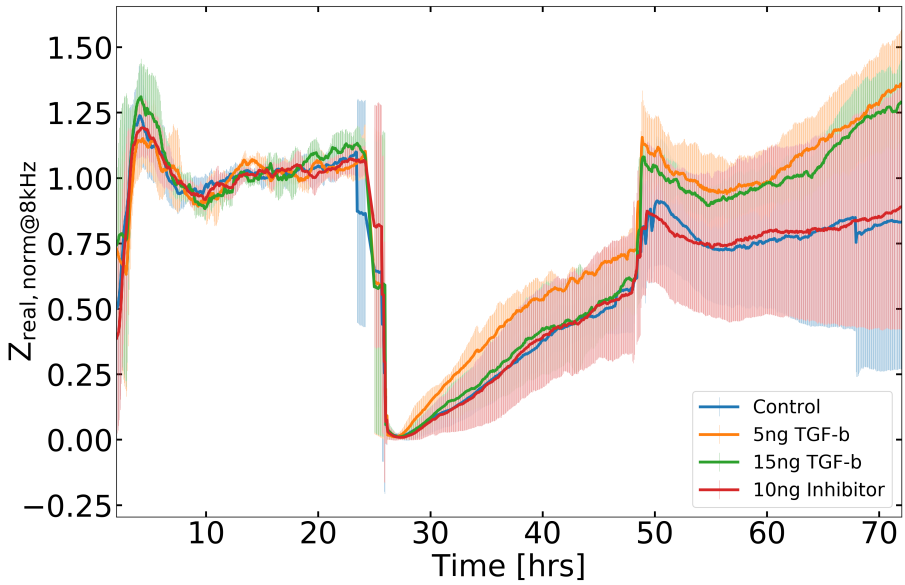

Figure 4.12.: Normalised mean resistance (real part) and standard deviation of measured impedance signals for concentrations with the most pronounced effect. The 10ng inhibitor (red, N=8, 4 experiments, 3 cell cultures) and 15ng TGF-β1 (green, N=4, n=n_c2) groups on average follow the control group (blue) (N=17, n=9, n_c=8), while cells with 5ng additional TGF-β1(yellow) (N=4, n=n_c=2) exhibit a faster and stronger initial response. Neither control nor inhibitor group recover the initial monolayer intensity, contrary to the 5ng and 15ng (green)(N=4, n=n_c2) groups that even surpass that level from 50h on.

As such, some curves showed a slower initial response during hours 30 to 40 and recovering somewhat during the last phase, while others followed a similar curve to the control group and deviated during this last phase. Overall, a clear impact of the TGF-β1 inhibitor on wound healing dynamics that could prove useful for further manipulations was not found in this context of cell resistance.
On the other hand, the additional TGF-β1 shows a distinctly different behaviour which is concentration dependent. The 5ng administration shows a faster initial response after wounding than all other curves and recovers up to the initial value of 1.0 with implications of rising further. This faster response time exists even in consideration of the standard deviations and offers a possible starting point for further manipulations of healing dynamics.
Surprisingly, the 15ng additional TGF-β1, represented by the green curve, show a transitional behaviour combining the initial response of the control group with the surpassing recovery of the 5ng TGF-β1 group during later stages, which might hint at inhibitory over-saturation effects

Complementary to the resistance in Figure 4.12, the normalised mean imaginary part of the impedance, the reactance, is shown in Figure 4.13 for a frequency of 64kHz allowing to asses the electrode coverage. The mean was taken over the same statistics as the resistance. Directly opposed to the real part, the monolayer formed after 24 h is set to zero as base line and the empty electrode signal to one. While

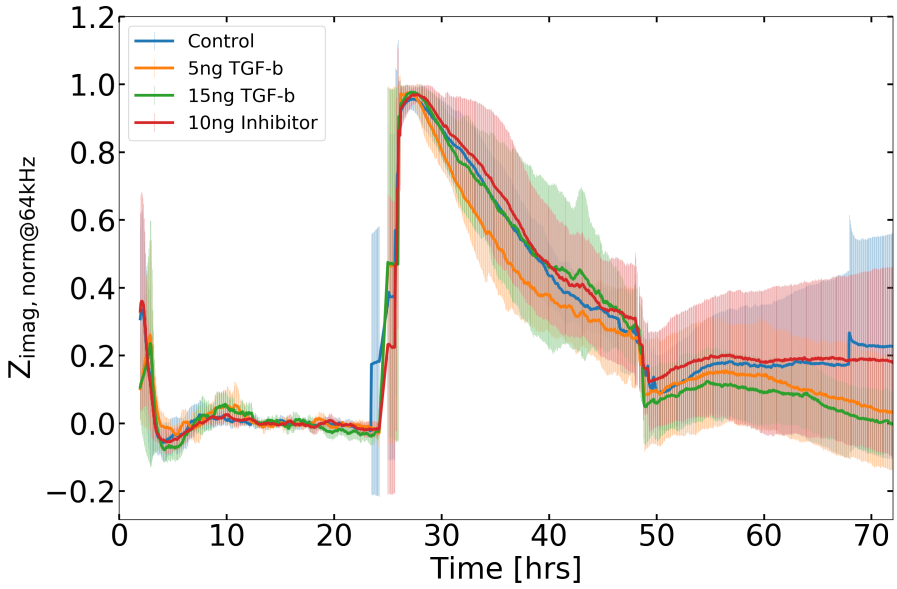

Figure 4.13.: Normalised mean reactance (imaginary part) and standard deviation of measured impedance for concentrations with the most pronounced effect. The trends seen in the resistance(Figure 4.12) are shown here as well, but not as strongly pronounced. As such,the 10ng inhibitor group (red, N=8, n=4 experiments, n_c=3 cell cultures) on average follows the curve of the control group (blue, N=17, n=9, n_c=8), while cells with 5ng additional TGF-β1(yellow, N=4, n=2, n=2) exhibit a faster initial response and only additional TGF-β1 groups recover to initial zero level, thus full electrode coverage.

distinctive behaviours could be clearly seen in the different resistance curves which also takes into account cell substrate and cell dynamics, the situation for the same concentrations is not so clear for the reactance. What is confirmed in this plot, is that the inhibitor curve seems to resemble the control group behaviour. Again, 5ng exibits a faster immediate response but not as strongly as for the resistance, and recovery of the initial value during the second day after wounding only occurs with the 15ng group. Similar to the resistance curves but not as pronounced, neither the control nor the inhibitor group recover the initial 0 value, so that only for the 15ng approach during the later phase a full prewounding electrode coverage can be assumed.

4.2.1. Evaluation of TGF-β1 modified monolayer properties with Lo model

Analogous to the evaluation of R_b , α and C_m of the formin k.o., we determine these parameters for TGF-β1 modified fibroblast cultures through the Lo/Ferrier model introduced in subsection 2.2.2, at different times of the experiment to gain insight into dynamic changes in cell vitality and behaviours during wound closure.
Beginning with R_b we will consider each parameter depending on TGF-β1 concentration

TGF-β1; Inhibitor(-) [ng]	R_b [Ωcm^2]				
	pre	24 h post		48 h post	
-200		(1.966±0.6)		-	
-100		(2.26±0.42)		-	
-15		(1.5±0.9)	(1.9±0.3)	(3.8±0.6)	
-10		(2.13±0.4)		(3.3±0.3)	(3.5±0.4)
-5		(1.7±0.5)		(3.41±0.22)	
0	(3.5±0.9)	(2.1±1.1)		(4.0±1.3)	
2.5		(1.4±0.9)		-	
5		(2.3±0.1)		(4.1±0.4)	
10		(2.2±0.1)	(1.87±0.21)	(3.46±0.34)	(3.79±0.22)
15		(2.0±0.4)		(3.8±0.4)	
25		(1.46±0.34)*		-	

Table 4.7.: Mean R_b over time for different TGF-β1 and inhibitor concentrations. With N the total number of electrodes out of n experiments: -200ng (N=6, n=3, N^{72}=4), -100ng(N=6, n=3, N^{72}=4),-15ng(N=5, n=3, N^{72}=4), -10ng(N=8, n=4, N^{72}=5), -5ng(N=5, n=3, N^{72}=4), 0ng(N^{20h}=51 n=9^20h, N^{72}=12, n^{72}=9), 2.5ng(N=3, n=2, N^{72}=3), 5ng(N=4, n=2, N^{72}=4), 10ng(N=8, n=4, N^{72}=6), 15ng(N=4, n=2, N^{72}=4), 25ng(N=4, n=2, N^{72}=4). * denotes significant deviation from wild type cells with $p<0.05$.

over time. The Lo/Ferrier model is based on the assumption of a consistent cell monolayer. As such, each parameter was determined for three significant stages of recovery: the unperturbed monolayer at the beginning of the experiment, a first stage of recovery 24 h after wounding, and close to the end of the experiment 48 h after wounding. For comparability and better statistics, a time interval of three hours was fitted, typically corresponding to 20 to 23 h for the pre-wounding initial state due to wounding at approx. 24 h, 45 to 48 h for a first recovery, and 69 to 72 h for final recovery representing confluency, repopulation and further differentiation of cells on the electrode. This was possible for most experiments but some could no longer be fitted after 60hrs, implying that the assumptions made no longer properly represent the situation at hand, most likely due to very strong changes in cell morphology, overcrowding or simply cell death; or most likely a combination of these factors. As a result R_b , α and C_m are averaged over the following total number of electrodes N out of n experiments with n_c cell cultures, with N^{20}=N^{45}=N: For -200ng N=6, n=3, n_c=3, N^{72}=4, for -100ng N=6, n=3, , n_c=3, N^{72}=4, for -15ng N=5, n=3, n_c=3, N^{72}=4, for -10ng N=8, n=4, n_c=3, N^{72}=5, for -5ng N=5, n=3, n_c=3, N^{72}=4, for 0ng N=51, n^20h=9, N^{72}=12, n^{72}=9, for 2.5ng N=3, n=2, n_c=2, N^{72}=3, for 5ng N=4, n=2, n_c=2, N^{72}=4, for 10ng N=8, n=4, n_c=3, N^{72}=6, for 15ng N=4, n=2, n_c=3, N^{72}=4 and for 25ng N=4, n=2, n_c=2, N^{72}=4.

A table of mean R_b values for these three times is shown in Table 4.7 with values

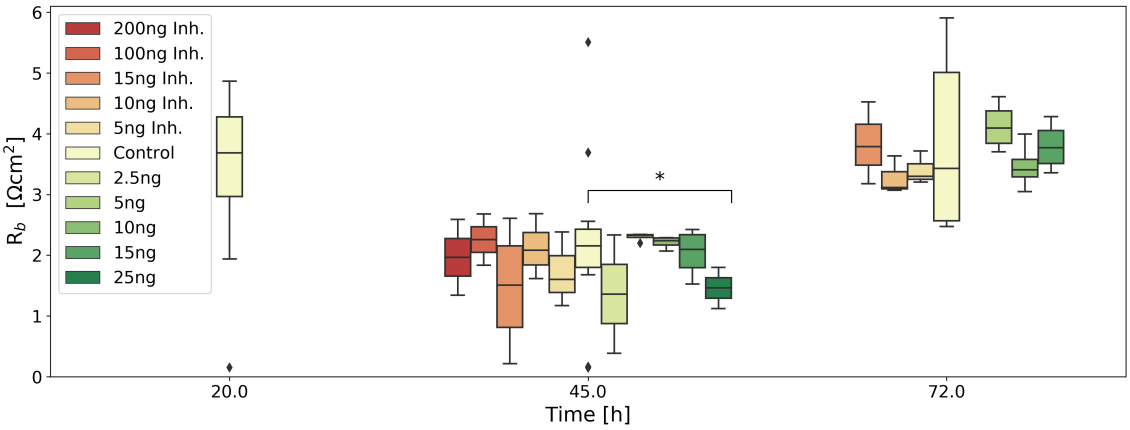

Figure 4.14.: R_b distribution for the different concentrations of inhibitor (red) and additional TGF-β1 (green) over time. With N the total number of electrodes out of n experiments: -200ng (N=6, n=3, N^{72}=4), -100ng(N=6, n=3, N^{72}=4),-15ng(N=5, n=3, N^{72}=4), -10ng(N=8, n=4, N^{72}=5), -5ng(N=5, n=3, N^{72}=4), 0ng(N^{20h}=51 n^20h=9, N^{72}=12, n^{72}=9), 2.5ng(N=3, n=2, N^{72}=3), 5ng(N=4, n=2, N^{72}=4), 10ng(N=8, n=4, N^{72}=6), 15ng(N=4, n=2, N^{72}=4), 25ng(N=4, n=2, N^{72}=4). * denotes significance with p<0.05, ♦ outliers.

depicted in Figure 4.15 as a function of concentration. As mentioned before, the negative concentration values are only used as indicator for an inhibitor concentration. For the category pre-wounding, no cytokines have been added yet and therefore values from all groups are averaged. Just by looking at these values, we can tell that unperturbed 3T3 -fibroblast have recovered and surpassed their initial R_b of (3.5±0.9) Ωcm^2 48 h after wounding with (4.0±1.3) Ωcm^2, while it is still reduced 24 h after wounding with (2.1±1.1) Ωcm^2. Thus we can assume that the cell-cell contact density based on Connexins and adherens junctions, determining the transcellular resistance, is only restored on the second day after a wounding occured. In comparison to that there are notably two distinctions shown in the first phase for inhibitor and TGF-β1 concentrations. The first is the significantly smaller R_b for 25ng added TGF-β1 of (1.46±0.34) Ωcm^2, which might imply a slowed or even impeded restoration of cell-cell contacts up to that time. At later times these concentrations were not possible to fit, making the question of whether this trend might continue in later stages an interesting point for further experiments.
A second point are two dips respectively in the inhibitor and TGF-βconcentrations. Additional to 25ng TGF-β1, there is a slight decrease at 2.5ng, and mirroring this, at 5ng and 200ng for the inhibitor. While none of these deviations are statistically significant, this as well might give important insights into the impact of TGF-β1 in fibroblast wound healing with further experiments. With (3.5±0.4) Ωcm^2 and (3.79±0.22) Ωcm^2 respectively, neither inhibitor nor TGF-β1 concentrations reach the control groups R_b, and while the TGF-β1 concentrations surpass the pre-wounding R_b, the inhibitor groups barely reach it.
This trend is further confirmed when looking at Figure 4.14 and Figure 4.15. The first plot shows the progress of R_b over time for the different concentrations and

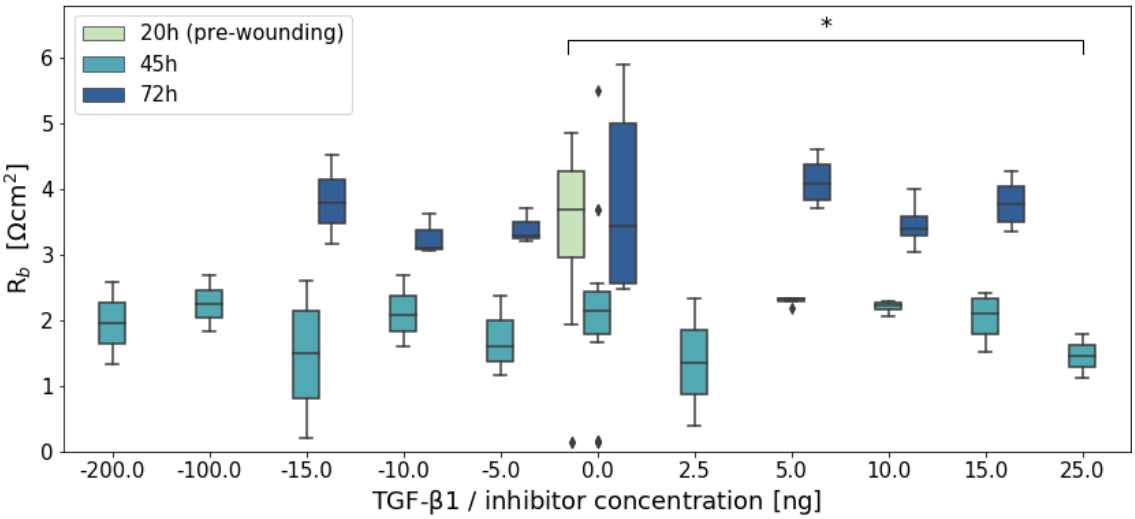

Figure 4.15.: R_b distribution over concentrations of inhibitor and additional TGF-β1 for t=20 h (pre-wounding), t=45 h (24 h after wounding) and t=72 h (48 h after wounding). In this case negative concentrations serve as notation for the inhibitor and have no mathematical meaning. With N the total number of electrodes out of n experiments: -200ng (N=6, n=3), -100ng(N=6, n=3),-15ng(N=5, n=3), -10ng(N=8, n=4), -5ng(N=5, n=3), 0ng(N^{20h}=51 n=9^{2}0h, N^{post}=17, n^{post}=9), 2.5ng(N=3, n=2), 5ng(N=4, n=2), 10ng(N=8, n=4), 15ng(N=4, n=2), 25ng(N=4, n=2). * denotes significance with p<0.05, ♦ outliers.

nicely visualises the average recovery. The second plot of the distribution of R_b over TGF-β1 concentration is a good representation of singular events and tendencies among the specific concentrations.

As such, it shows more clearly than Table 4.7 and Figure 4.14 the significantly lower R_b for 5ng and 15ng inhibitor 24 h after wounding and treatment, while for additional TGF-β1 no significant increase occurs.

The parameter α was determined together with R_b from the same fit and the analysis follows similar principles; As such, Table 4.8 lists the averaged fit results for the three characteristic phases pre-, post-wounding and additional differentiation. Time intervals for the fitting where chosen to match the ones as for R_b. Errors shown in Table 4.8 were calculated from the standard deviations with Gaussian error propagation and a t-test was done to check for significance.
From the unperturbed but wounded control group we can assume 3T3 fibroblasts to typically have a higher α with (0.12±0.11) $\Omega^{1/2}$cm , but with large deviations, before wounding, that is smaller 24 h after wounding with (0.4±0.3) $\Omega^{1/2}$cm and more so 48 h after wounding. This means that before wounding cell-substrate distance appears to be smaller than after wounding. 24 h after wounding, there is a tendency for α to increase with TGF-β1 inhibition and decrease with TGF-β1 addition, suggesting that cell-substrate distance increases with TGF-β1 availability, an thus myofibroblast-transitions.
Most notable is the higher α with the addition of 200 ng inhibitor of (0.11±0.02)

TGF-β1; Inhibitor(-) [ng]	α $[\Omega^{1/2}\text{cm}]$				
	pre	24 h post		48 h post	
-200		(0.11±0.02)*		-	
-100		(0.03±0.01)		-	
-15		(0.07±0.05)	(0.068±0.011)	(0.1±0.1)	
-10		(0.07±0.01)		(0.1±0.1)	(0.13±0.05)
-5		(0.06±0.01)		(0.2±0.01)****	
0	(0.12±0.11)	(0.04±0.03)		(0.03±0.02)	
2.5		(0.03±0.02)		-	
5		(0.03±0.01)		(0.03±0.01)	
10		(0.01±0.004)	(0.01±0.005)	(0.020±0.004)	(0.02±0.008)
15		(0.02±0.01)		(0.02±0.02)	
25		(0.010±0.005)		-	

Table 4.8.: Mean α over time for different TGF-β1 or inhibitor concentrations. With N the total number of electrodes out of n experiments: -200ng (N=6, n=3), -100ng(N=6, n=3),-15ng(N=5, n=3), -10ng(N=8, n=4), -5ng(N=5, n=3), 0ng(N^{20h}=51 n=9^{2}0h, N^{post}=17, n^{post}=9), 2.5ng(N=3, n=2), 5ng(N=4, n=2), 10ng(N=8, n=4), 15ng(N=4, n=2), 25ng(N=4, n=2). *,**** denotes significance with p<0.05 and p<0.0001 respectively.

$\Omega^{1/2}$cm (p<0.05) in comparison to wild type α of (0.04±0.03) $\Omega^{1/2}$cm. This impression is reinforced by α 48 h after wounding. Here, α increases from (0.020±0.008) $\Omega^{1/2}$cm with TGF-β1 addition, over (0.03±0.02) $\Omega^{1/2}$cm without any input, to (0.13±0.05) $\Omega^{1/2}$cm with TGF-β1 inhibition.
Interestingly, at this point α for 5ng inhibitor addition showed the strongest and significant divergence from the wild type with (0.2±0.01) $\Omega^{1/2}$cm (p<0.0001) to (0.03±0.02) $\Omega^{1/2}$cm, while only a slight increase was detected during the second phase. This speaks for a stronger impact of TGF-β1 inhibition during the third phase where a confluent monolayer has been recovered and also underlines that even 48 h after wounding further cell differentiation takes place.
However, there are two notable exceptions to this tendency 24 h after wounding: With the addition of 200ng inhibitor α appears to be on the same level as wild type α, and thus smaller than with all other inhibitor concentrations, meaning that despite 100ng inhibitor cell-substrate interactions seem unperturbed. Similarly, there is a slight increase of α for 15ng additional TGF-β1 compared to 10 and 25ng, which could hint to a slightly stronger reaction to that specific concentration and should be investigated further.

The results from Table 4.8 are plotted, similarly to R_b in Figure 4.16 as α over time, and Figure 4.17 over concentration for the different phases. In comparison the the larger α distribution before wounding, 24 h afterwards α shows clearer distinctions, most notably the significantly higher α of (0.11±0.02) $\Omega^{1/2}$cm (p<0.05) than the wild type α with (0.04±0.03) $\Omega^{1/2}$cm. This implies that with the addition

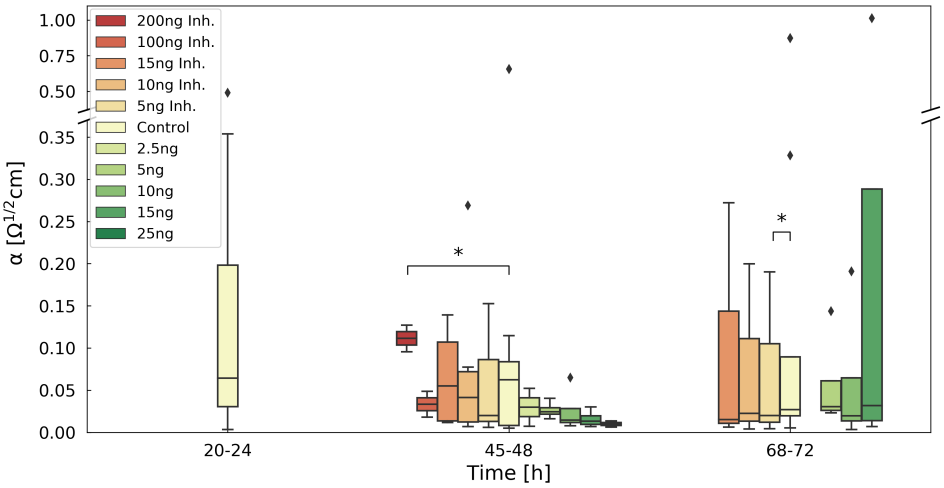

Figure 4.16.: α distribution for the different concentrations of inhibitor (red) and additional TGF-β1 (green) over time. With N the total number of electrodes out of n experiments: -200ng (N=6, n=3), -100ng(N=6, n=3),-15ng(N=5, n=3), -10ng(N=8, n=4), -5ng(N=5, n=3), 0ng(N^{20h}=51 n=9^{2}0h, N^{post}=17, n^{post}=9), 2.5ng(N=3, n=2), 5ng(N=4, n=2), 10ng(N=8, n=4), 15ng(N=4, n=2), 25ng(N=4, n=2). *, **** denotes significance with p<0.05 and p<0.0001 respectively, ♦ outliers.

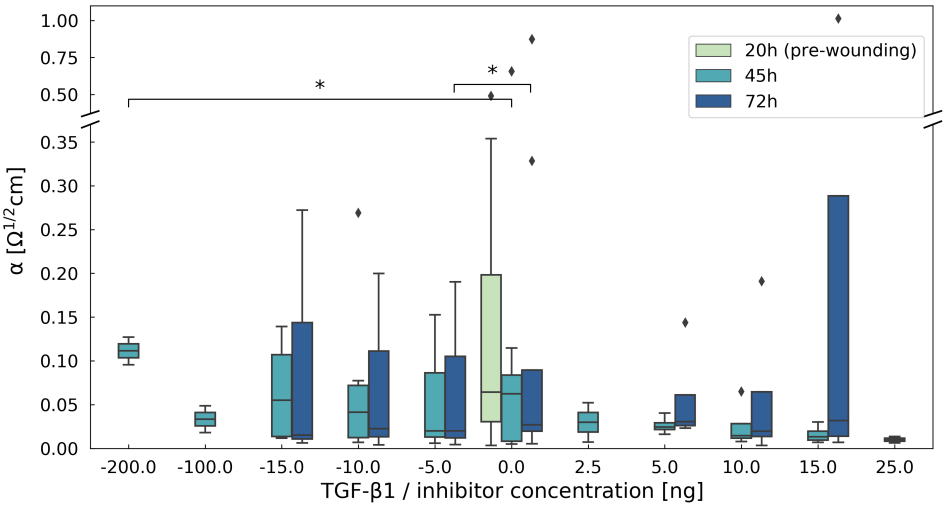

Figure 4.17.: α distribution for the different concentrations of inhibitor (shaded in red) and additional TGF-β1 (shaded in green) over time. Negative concentrations serve as notation for the inhibitor and have no mathematical meaning. With N the total number of electrodes out of n experiments: -200ng (N=6, n=3), -100ng(N=6, n=3),-15ng(N=5, n=3), -10ng(N=8, n=4), -5ng(N=5, n=3), 0ng(N^{20h}=51 n=9^{2}0h, N^{post}=17, n^{post}=9), 2.5ng(N=3, n=2), 5ng(N=4, n=2), 10ng(N=8, n=4), 15ng(N=4, n=2), 25ng(N=4, n=2). *, **** denotes significance with p<0.05 and p<0.0001 respectively, ♦ outliers.

of 200ng ALK5 inhibitor, thus blocking the main TGF-β1 signalling pathway to that extent, cells seem to be closer to the substrate, forming closer adhesion bonds. In direct contrast to that, the smaller α from TGF-β1 addition from Table 4.8 24 h after wounding seems to decline with higher TGF-β1 concentration, meaning that these fibroblasts adhere less strongly to the substrate. 48 h after wounding we see the strongest difference surprisingly between 5ng inhibition and unperturbed fibroblasts, suggesting a bigger cell-substrate distance that seems to increase with stronger inhibition of TGF-β1.
Figure 4.17 shows α over time. Here, the tendency for α to be higher before wounding, thus adhesion stronger, than after wounding is highlighted, and for a better distinction between the concentrations' impact more statistics is required.

TGF-β1(+); Inhibitor(-) [ng]	C_m $[10^{-6}\mu Fcm^{-2}]$				
	pre	24 h post		48 h post	
-200		(1.4±0.3)		-	
-100		(1.3±0.1)		-	
-15		(6±5)	(3.1±1.3)	(1.2±0.4)	
-10		(1.54±0.03)		(1.23±0.13)	(1.2±0.2)
-5		(5±4)		(1.1±0.2)	
0	(4.4±4.2)	(1.4±0.2)		(1.2±0.1)	
2.5		(2.9±1.8)		-	
5		(1.4±0.2)		(1.0±0.1)	
10		(1.7±0.5)	(1.9±0.4)	(1.11±0.14)	(1.27±0.09)
15		(1.6±0.4)		(1.7±0.2)	
25		(1.7±0.2)*		-	

Table 4.9.: Mean C_m over time for different TGF-β1 or inhibitor concentrations. With N the total number of electrodes out of n experiments: -200ng (N=6, n=3), -100ng(N=6, n=3),-15ng(N=5, n=3), -10ng(N=8, n=4), -5ng(N=5, n=3), 0ng(N^{20h}=51 n=9^20h, N^{post}=17, n^{post}=9), 2.5ng(N=3, n=2), 5ng(N=4, n=2), 10ng(N=8, n=4), 15ng(N=4, n=2), 25ng(N=4, n=2). * denotes significance with p<0.05.

The last fit parameter considered from this line of analysis is the average cell membrane capacitance C_m. Similar to R_b and α the mean fit results are listed in Table 4.9 for each concentration and time interval. Errors shown in Table 4.8 were calculated from the standard deviations with Gaussian error propagation and a t-test was done to check for significance.
For unperturbed cells, C_m appears to be smaller after wounding. This tendency becomes clear despite a wide variation in C_m due to accumulations around 1 μFcm^{-2} and 10 μFcm^{-2}, because 48 h after wounding with (1.2±0.1) μFcm^{-2} C_m is significantly smaller than before wounding with (4.4±4.2) μFcm^{-2} (p<0.001), and 24 h after wounding with (1.4±0.2) (p<0.05) This can be seen in Figure 4.19, where C_m is plotted over the concentrations and time variations among each category

is visualised. Considering the addition of TGF-β1 inhibitor, C_m does not vary

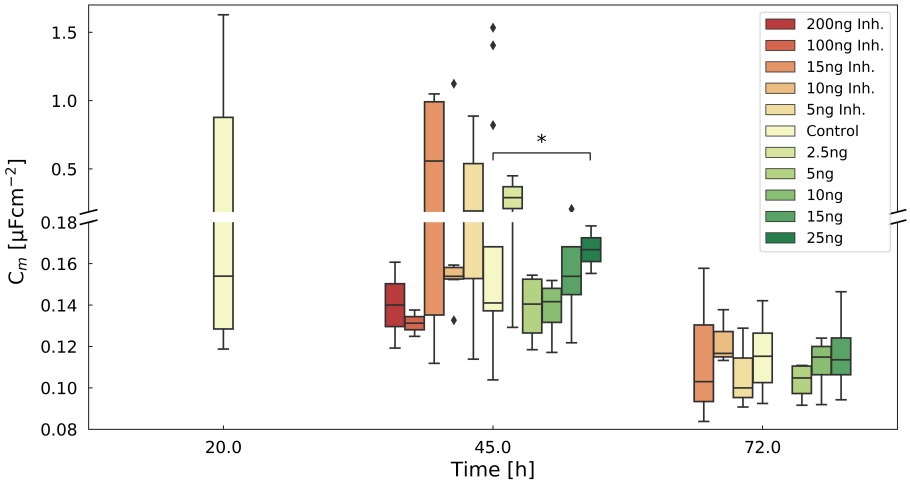

Figure 4.18.: C_m over time for different TGF-β1 (green) and inhibitor (red) concentrations. Here, C_m is significantly higher with 25ng additional TGF-β1 than the average wild type C_m . With N the total number of electrodes out of n experiments: -200ng (N=6, n=3), -100ng(N=6, n=3),-15ng(N=5, n=3), -10ng(N=8, n=4), -5ng(N=5, n=3), 0ng(N^{20h}=51 n=9^{2}0h, N^{post}=17, n^{post}=9), 2.5ng(N=3, n=2), 5ng(N=4, n=2), 10ng(N=8, n=4), 15ng(N=4, n=2), 25ng(N=4, n=2). * denotes significance with p<0.05, ♦ outliers.

distinctly from the wild type, with the exceptions of wider distributions in C_m with 5 and 15ng inhibitor, which might suggest a varying reaction in this second phase, but is not significant. This impression continues 48 h after wounding, where C_m also shows no distinction from the wild type, which suggests that the inhibition of TGF-β1 has no distinct impact on membrane capacitance, and thus membrane surface area and lipid composition.
However, with the additional TGF-β1 membrane capacitance appears to increase, most notably to (1.7±0.2) µFcm^{-2} (p<0.05) with 25ng TGF-β1 in contrast to (1.4±0.2) µFcm^{-2} for unperturbed fibroblasts. 10 and 15ng lead to similar C_m , increasing that possibility.
48 h after wounding C_m only seems to be increased for 15ng, making further investigations into the impact of 15 and 25ng on membrane capacitance relevant. This tendency of C_m to increase with TGF-β1 concentration during the second phase can be seen in Figure 4.18, where C_m is plotted over time which allows direct comparison of the impact due to different concentrations during each phase. This means that with the addition of 25ng TGF-β1 membrane capacitance increases 24 h after wounding in comparison to cells with unperturbed or inhibited TGF-β1 levels, implying a slight increase in membrane surface.
On the other hand, the slightly smaller C_m with 100ng inhibitor of (1.3±0.1) µFcm^{-2} , might prove an interesting point for further experiments, especially considering the variations of R_b and α that occured with the addition of 100ng inhibitor.
Figure 4.19 allows for direct comparison of C_m during the three phases for each

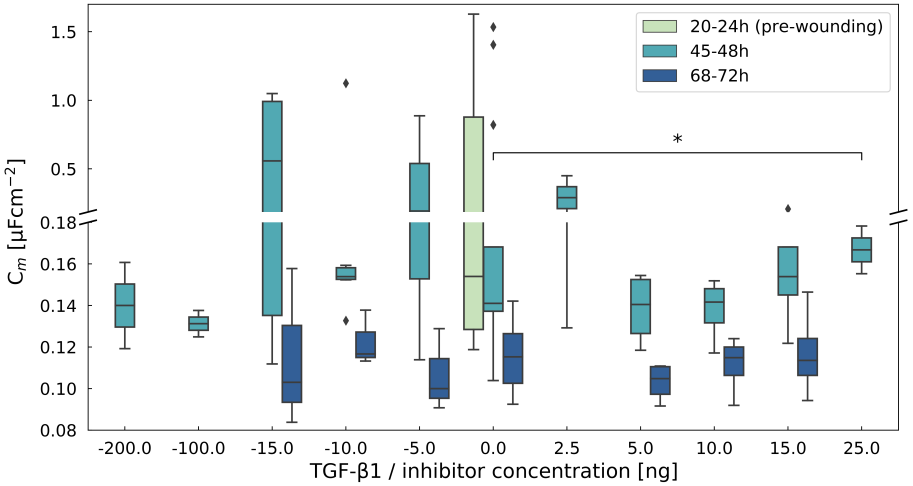

Figure 4.19.: C_m for the different concentrations of inhibitor and additional TGF-β1 for the three phases. C_m decreases with time for all concentrations, and for 25ng TGF-β1 C_m is significantly higher than wild type C_m . Negative concentrations serve as notation for the inhibitor. With N the total number of electrodes out of n experiments: -200ng (N=6, n=3), -100ng(N=6, n=3),-15ng(N=5, n=3), -10ng(N=8, n=4), -5ng(N=5, n=3), 0ng(N^{20h}=51 n=9^20h, N^{post}=17, n^{post}=9), 2.5ng(N=3, n=2), 5ng(N=4, n=2), 10ng(N=8, n=4), 15ng(N=4, n=2), 25ng(N=4, n=2). * denotes significance with p<0.05, ⧫ outliers.

concentration. This especially highlights that C_m tends to decrease with time, especially 48 h after wounding compared to C_m before. A slight increase 24 h after wounding can be observed for additional TGF-β1, while also showing how little C_m really varies. In summary, TGF-β1 seems to impact membrane capacitance only slightly, and only with increased concentration.

4.2.2. Recovery time

Analogous to the evaluation of recovery half time $t_{1/2}$ and rate $r_{1/2}$, the same sigmoidal function is fitted to a recovery interval of a resistance curve chosen as before between completed wounding, typically a curve minimum and the point where the amplitude was quasistationary. The approach is the same as before, so that we gain the results listed in Table 4.9 from fitting the same sigmoidal function (Equation 4.1) to a recovery interval of a resistance curve chosen as before between completed wounding, typically a curve minimum, and the point where the initial amplitude was quasistationary.

In Table 4.10 the averaged results for the recovery half time $t_{1/2}$ and rate $r_{1/2}$ extracted with the aforementioned sigmoidal assumption (see subsection 4.1.2) are shown for each concentration. Considering the mean over all inhibitor and TGF-β1 concentrations, $t_{1/2}$ seems to be smaller with additional TGF-β1 taking 13.9±2.4)h to recover half monolayer impedance, than unperturbed and inhibited cells with (15.3±3.0)h and (15±2)h respectively. However, while a faster recovery time is confirmed significantly for the addition of 5ng TGF-β1 with (11±5)h, it

TGF-β1(+); Inhibitor(-) [ng]	$t_{1/2}$ [h]	Mean	$r_{1/2}$ [1/h]	Mean
-200	(15±5)		(5±2)	
-100	(16.5±3.1)		(7±2)	
-15	(11.0±3.3)*	(15±2)	(6.4±2.2)	(6.6±1.1)
-10	(14.0±4.3)		(6.9±2.5)	
-5	(16.7±6.0)		(7.8±3.4)	
0	(15.3±3.0)		(4.6±1.2)	
2.5	(16±3)		(7±2)	
5	(11±5)*		(5.5±2.2)	
10	(13.6±5.1)	(13.9±2.4)	(5±3)	(5±1)
15	(14±6)		(3.2±1.3)*	
25	(15.1±7.3)		(6.1±2.21)	

Table 4.10.: Averaged $t_{1/2}$ and $r_{1/2}$ from sigmoidal recovery fit for different concentrations. *,** denotes significant deviation from wild type cells with $p<0.05$ and $p<0.01$ respectively. With N the total number of electrodes out of n experiments: -200ng (N=6, n=3), -100ng(N=6, n=3),-15ng(N=5, n=3), -10ng(N=8, n=4), -5ng(N=5, n=3), 0ng(N=17, n=9), 2.5ng(N=3, n=2), 5ng(N=4, n=2), 10ng(N=8, n=4), 15ng(N=4, n=2), 25ng(N=4, n=2).

also applies to the addition of 15ng inhibitor with similar $t_{1/2}$of (11.0±3.3)h, both reaching a half recovery 2h faster than the wild type with (15.3±3.0)h. Surprisingly, other additions of TGF-β do not seem to influence the overall recovery time significantly. For inhibitor concentrations, on the other hand, there are slightly higher $t_{1/2}$ for 5ng and 100ng, which confirms the necessity to further investigate the impact of 100ng inhibitor as that concentration showed slight deviations across R_b, α and C_m as well.

In summary, faster $t_{1/2}$ with 5ng additional TGF-β1 implies faster wound healing promoted by an enhanced transformation of fibroblasts to myofibroblasts.

However, this does not explain the equally increased recovery seen with 15ng TGF-β1 inhibitor. This deviation among inhibitor concentrations is also found in Figure 4.20, where $t_{1/2}$ is plotted over additional TGF-β1 and inhibitor concentration respectively. This figure further shows that there is no faster recovery observed than the the two mentioned, and also no significantly slower recovery than the wild type's.

In direct relation, the recovery rate can be considered to gain insight into whether TGF-β1 and its inhibition influences fibroblast wound healing in this context. The resulting $r_{1/2}$ listed in Table 4.10 shows a significant deviation from the wild type $r_{1/2}$ (4.6±1.2)1/h with the addition of 15ng of TGF-β1 $r_{1/2}$ (3.2±1.3)1/h. This higher rate together with a $t_{1/2}$ similar to the unperturbed cells suggests that cells might respond slower but heal faster once the initial lag is overcome.

Interestingly, for all remaining concentrations of TGF-β1 and inhibitor $r_{1/2}$ is slightly higher, thus healing slower, than for unperturbed cells. This is resembled in a higher mean $r_{1/2}$, especially for the inhibitor concentrations with (6.6±1.1)1/h,

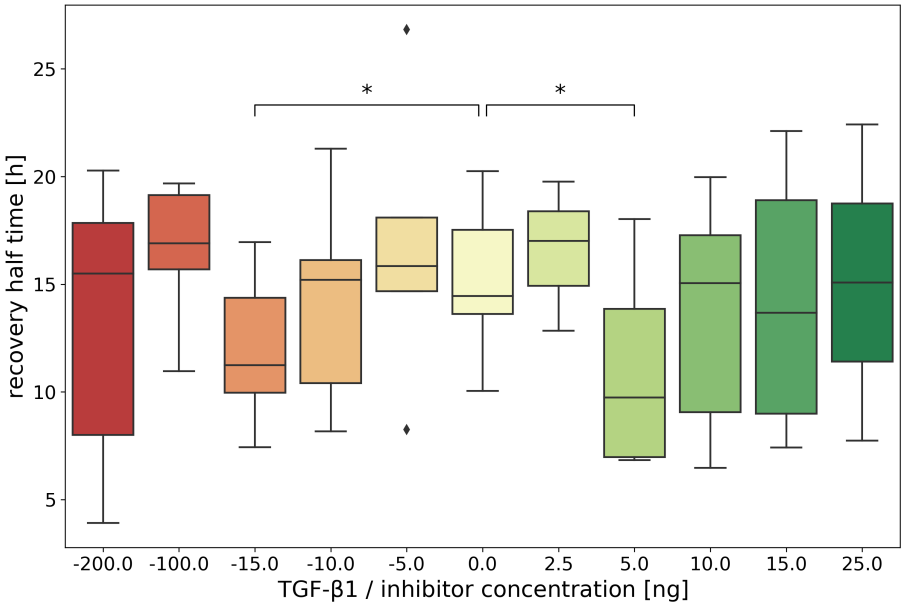

Figure 4.20.: Half point recovery time $t_{1/2}$ plotted over different concentrations of ALK5 inhibitor (area shaded in red) and additional TGF-β1 (area shaded in green). The blue line denotes $t_{1/2}$ for unperturbed cells for better comparison. Negative concentration values are used as notation for inhibitor concentrations. With N the total number of electrodes out of n experiments: -200ng (N=6, n=3), -100ng(N=6, n=3),-15ng(N=5, n=3), -10ng(N=8, n=4), -5ng(N=5, n=3), 0ng(N=17, n=9), 2.5ng(N=3, n=2), 5ng(N=4, n=2), 10ng(N=8, n=4), 15ng(N=4, n=2), 25ng(N=4, n=2). * denotes significance with $p<0.05$, ♦ outliers.

and reinforced by the significant deviation of $r_{1/2}$ with 100ng inhibitor (7±2)1/h ($p<0.01$) and 10ng inhibitor (6.9±2.5)1/h ($p<0.05$) from the smaller rate with 15ng TGF-β1. Figure 4.21 shows the impact of the different concentrations on $r_{1/2}$.
In summary, the recovery half time is significantly reduced by the addition of 5ng TGF-β1 and 15ng ALK5 inhibitor. While this suggests an enhanced fibroblast to myofibroblast transition due to the additional TGF-β1, the 15ng inhibitor seems to trigger different wound healing dynamics. That the $r_{1/2}$ is not significantly decreased for either concentrations, and equal or slightly increased compared to unperturbed $r_{1/2}$, indicating a faster response. In addition to this, a 15ng TGF-β1 lead to a higher $r_{1/2}$, an indication that fibroblasts migrate faster into the wounded area with a certain lag phase, as $t_{1/2}$is not significantly smaller. The clear distinction of fibroblasts with 15ng TGF-β1 to 100ng and 10ng inhibitor, as well as unperturbed cells, decided the addition of 15ng TGF-β1 for droplet experiments in **??**.
Figure 4.21 shows the recovery rate $r_{1/2}$ from Table 4.10 for the different concentrations. In this figure we can confirm the tendencies already seen from the results in Table 4.10. As such, the inhibitor concentrations, shaded in red, mainly show rates significantly above that of the control group, with the exception of 10ng inhibitor added which has $r_{1/2}$ smaller than the control groups'. The tendency previously seen for additional TGF-β1 to induce equal or smaller rates is also confirmed by this plot; only two

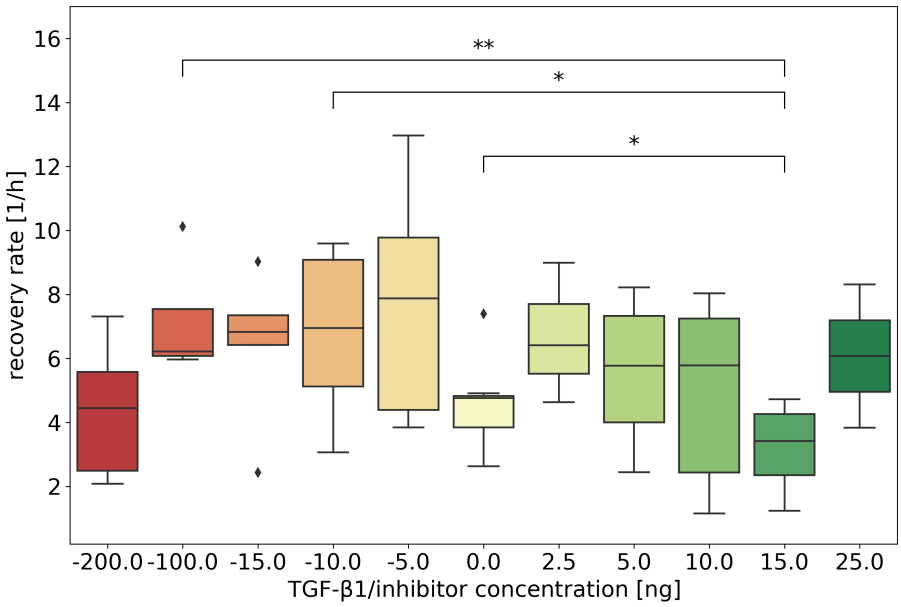

Figure 4.21.: Recovery rate $r_{1/2}$ plotted over different concentrations of ALK5 inhibitor (area shaded in red) and additional TGF-β1 (area shaded in green). The blue line denotes $r_{1/2}$ for unperturbed cells for better comparison. Negative concentration values are used as notation for inhibitor concentration. With N the total number of electrodes out of n experiments: -200ng (N=6, n=3), -100ng(N=6, n=3),-15ng(N=5, n=3), -10ng(N=8, n=4), -5ng(N=5, n=3), 0ng(N=17, n=9), 2.5ng(N=3, n=2), 5ng(N=4, n=2), 10ng(N=8, n=4), 15ng(N=4, n=2), 25ng(N=4, n=2). *,** denotes significance with $p<0.05$ and $p<0.01$ respectively, ♦ outliers.

rates at 5ng and 15ng additional TGF-β1 have a significantly smaller $t_{1/2}$. This is in good agreement with previous observations for additional TGF-β1 concentrations of 5ng and 15ng having the strongest impact on the fibroblasts. The clear exception of a high $t_{1/2}$ at 2.5ng is also obvious from this figure.

4.3. Microfluidic production of polymeric carrier droplets

4.3.1. Cell viability (MTT assay)

As a first step to the creation of stable pNIPAm polymerosomes, it was necessary to find a combination of concentrations for the aqueous droplet solution that would be stable not only during and shortly after production, but also for longer periods of time, under multiple temperature adjustments and in different buffer environments, especially in cell medium (see section 3.1). Additionally, production was supposed to be as simple and universal to implement as possible, thus requesting chemical polymerisation. To ensure the droplets would not be toxic to the used line of 3T3 fibrobalst cells or otherwise negatively influencing cell viability or metablolism in a significant way, an MTT test was done for varying amounts of droplets per ml in weight/volume-% and number of washing steps after production. This test was performed together with Dr. Tabea Oswald in the cell culture facility of the Faculty of Chemistry. The results are shown in Figure 4.22 as difference from a cell-only control group in percentage.

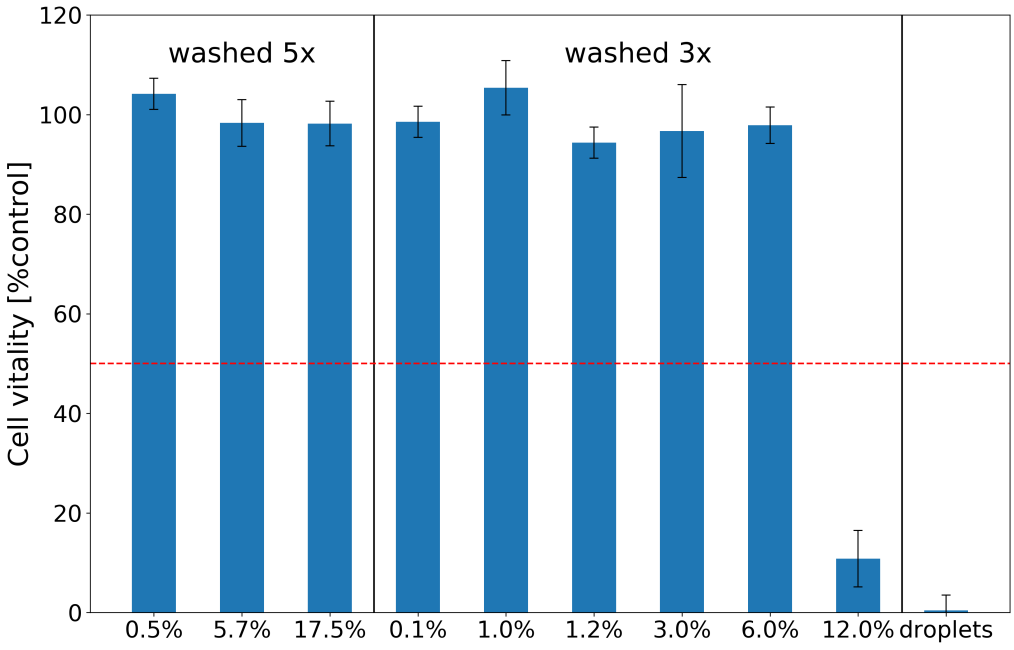

Figure 4.22.: Results of an MTT test of chemically polymerised droplets on 3T3 fibroblasts in different v/w-percentage in respect to the culture medium they are contained in, and either three or five washing steps. Only a higher concentration (12%) of droplets that were only washed three times had a toxic impact on the cells, while none of the other combinations show any significant negative impact and are clearly non-influential to cell viability (red line = 50%).

From this it is easily seen that the only values below 50% viability are for samples

with droplets at 12% (w/v) per ml that were only washed three times, the minimal amount required, and a sample containing only droplets and no cells to check for potential redox interactions between tetrazolium salt and polymer, or possible residue among the droplets.

In comparison to the reduction of (89.2±0.5)% of the 12% sample, the 17.5% sample that was washed 5 times showed only a reduction of (1.8±0.5)%. That is significantly bigger than 50% cell viability and as such was sufficient in this early stage to assume no cytotoxic effects on the cellular model system for this first implementation. A calculation or approximation of half maximal inhibitory concentration (IC_{50}) was not necessary, as a sigmoidal shape and expanded testing for the IC_{50} would have needed high and costly polymer concentrations way beyond the application concentration and was not relevant at this point.

4.3.2. Droplet production and encapsulation

Based on the procedure described in [44] a combination of concentrations producing stable droplets was found in the ratios of

$$\text{NIPAm} : \text{BIS} : \text{APS} = 9.4 : 0.6 : 0.7 \ . \tag{4.2}$$

The droplets from this solution are shown in Figure 4.23a. With this condition as base line, the crosslinker concentration was varied in both directions for 0.3%, 0.6%, 1.5%, 3.0%, 4.0%, 5.0% to narrow down a stable production regime. Respective images of the experiments can be found in AppendixAppendix A. While the 0.3% sample did not polymerise properly and, as such ruled out lower concentrations while above 3.0% the solution nears saturation, thus the components dissolve only with difficulty, the most promising samples were those at 0.6%, 1.5% and 3.0%.

To test the droplets for their carrier properties, they were loaded with the watersoluble

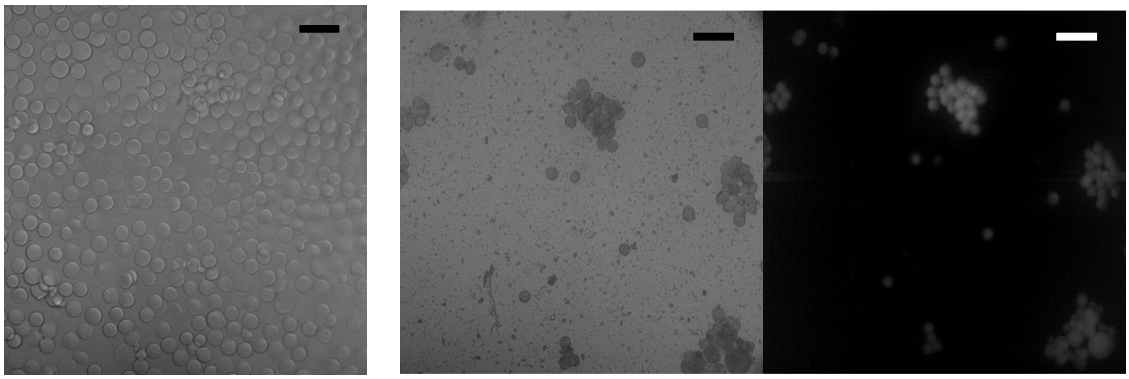

(a) Basic solution with 0.6% crosslinker.

(b) Adjusted solution with 1.5% crosslinker and FluoNa as marker.

Figure 4.23.: Images of droplets from different solutions. The basic solution (a) had to be adjusted to allow for crosslinking of monomers despite the presence of cargo molecules (b).

fluorochrom fluorescein sodium, which also supplied a means of visibility Figure 4.23b. From tests it became clear, that pNIPAm does not polymerise properly for the 0.6%

crosslinker droplets, as the produced droplets dissolved during the washing process. By raising the crosslinker to 1.5% and 3.0% droplets polymerised properly, albeit with a smaller yield.
For further use as carrier system, the solution of 1.5% crosslinker was used as it gave the best and most reliable results. When fluorescein sodium was exchanged for TGF-β1, NIPAm polymerisation and resulting droplets did not change and, thus, did not appear to be influenced in a significant way.

4.3.3. Temperature sensitivity and droplet size

The droplet composition ultimately used for following cell experiments of 1.5% crosslinker concentration was tested for their temperature sensitivity, the deciding factor for this controllable system. First and foremost, PNIPAm's thermal responsiveness was tested optically as key feature for controlled content release. This responsiveness was measured in a series of bright field phase contrast micrographs for temperatures from 25°C up to 40°C in steps of 5°C, with an uncertainty of ±2°C from the heat plate. We could also study the droplets shape recovery during cooling. Exemplary results of this measurement with a 63x objective are shown in Figure 4.24 with a red arrow indicating temperature switching. In Appendix A a more extensive documentation of the experiment can be found with the entire image series.

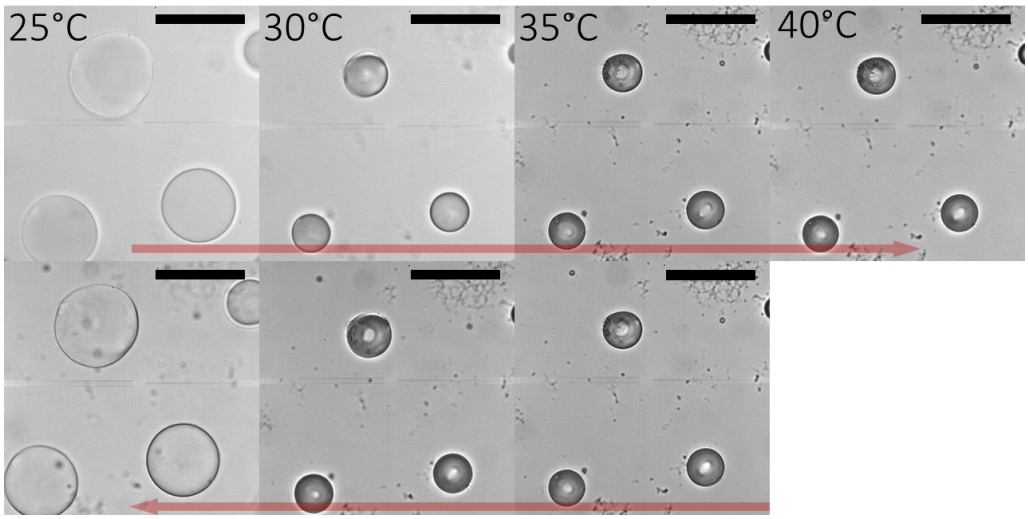

Figure 4.24.: Droplets's thermal response and shape recovery for increasing temperature (top red arrow) from 25°C to 40°C, and decreasing temperature (bottom red arrow) in steps of 5°C. The droplets recover their initial size and shape. The test sample consisted of N≈ 70 droplets with 1.5% crosslinker for each temperature.

The results of this analysis are listed in Table 4.11 and plotted in Figure 4.25 for which the diameter of droplets was measured using ImageJ and averaged over a sample of approximately 70 droplets. As foundation for these evaluations served the images shown in Appendix??, the shape recovery is not entirely symmetrical, but with a distinct lag, especially seen in the average diameter of droplets at 35°C.

Temperature	25	30	35	40
Diameter [µm]	(100±10)	(51±9)	(43±7)	(39±7)
-recovery [µm]	(91±12)	(43±7)	(39±7)	

Table 4.11.: Quantitative analysis of PNIPAm droplets' thermal responsiveness and shape recovery via optical diameter quantification.

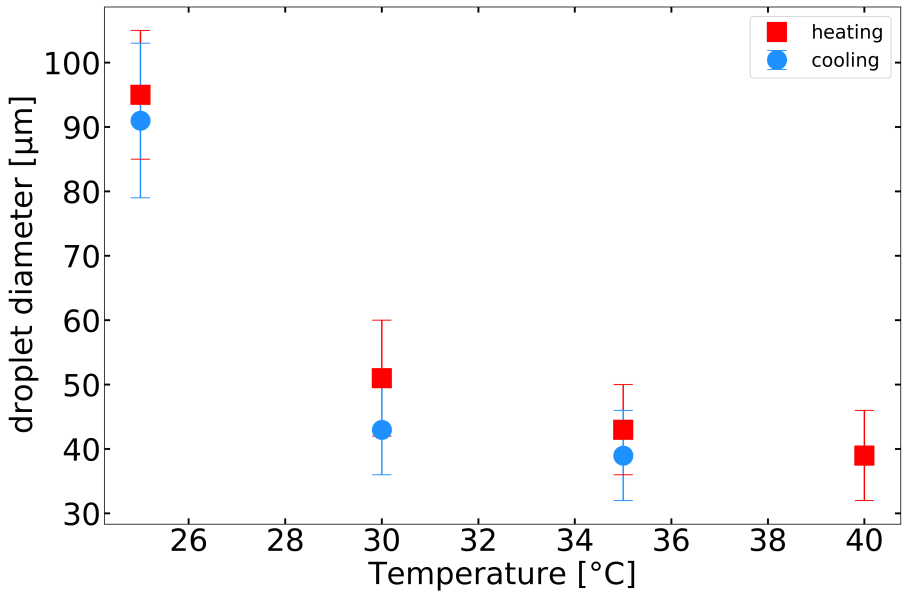

Figure 4.25.: Thermal responsiveness assessed via shape recovery of PNIPAm droplets. The shape response of the droplets to a change in temperature is not symmetrical between heating (red) and cooling (blue) but shows a clear lag in recovering the shape.

When raising the temperature to 35°C the diameter shrinks to (43±7) µm and upon recovery when dropping to the same temperature it is still equal to the diameter at 40°C of (39±7) µm, and it is only at 30°C temperature that the size of (43±7) is recovered. Interestingly, the greatest change in size could be observed during the transition from 25°C to 30°C in both directions, although PNIPAm's LCST is given at 32°C.

4.3.4. Droplet Young's modulus

A second important question concerning the suitability of the droplets was posed by their elastic properties, usually best characterized by the Young's modulus (see **??**). The aim was to not only provide cells controllably with cytokines but also with a possible scaffold to not only change wound healing dynamics but also to eventually use for contact guidance to form a hybrid tissue. As such, the droplets had to be of a proper size of approximately 100 µm for them to neither be immediately consumed by cells or cause curvotaxis, but also they should be rigid enough, meaning that E should be on the order of typical cells at least, preferably one or two orders of

magnitude higher to promote cell polarisation [52]. An AFM was used to measure single force-distance curves in order to precisely determine E for single droplets during the two different temperature dependent PNIPAm states, as described in **??**. During this AFM experiment 7 droplets were measured at room temperature of approximately 20° and above the LCST at 37° to be comparable the situation to when they are used as carriers and scaffold with cells in an incubator. The plot in Figure 4.26a shows the behaviour of E over time with varied temperature for each measured droplet, averaged over multiple measurements. One can see that stiffness increases significantly over approximately two orders of magnitude when heated above PNIPAm's lower critical solution temperature to 37°C, and returns to it's initial value.

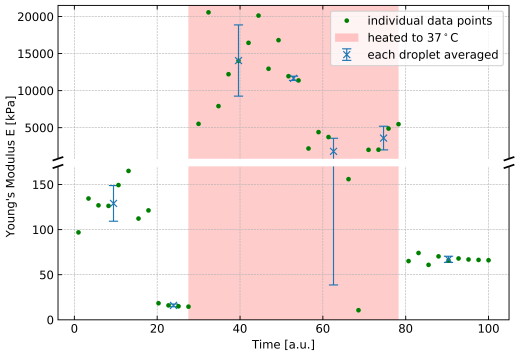

(a) Young's modulus E over time for each measured droplet with N=7 over a temperature switching cycle.

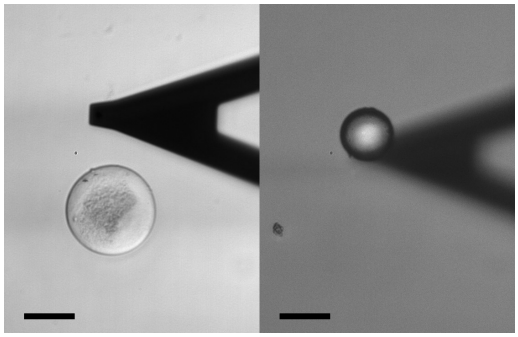

(b) Bright field image of a droplet during an AFM experiments at room temperature (left) and at 37°C. The cantilever is outside the focal plane because it is not in contact with the droplet.

Figure 4.26.: AFM measurement of Young's modulus E of polymeric droplets over a temperature switching cycle. Depicted here is E for 1.5%(v/w) crosslinker of one day of one day of experiments. 7 different droplets were each measured N_i times with $N_1 = 8$, $N_2 = N_6 = 4$, $N_3 = N_7 = 9$, $N_4 = 2$, $N_5 = 5$.

This includes a significantly larger error, especially for the heated droplets, due to differences in size, surroundings and slight polymerisation differences, as can be seen in the bright field micrograph in Figure 4.26b. However, the behaviour stays the same: a significant increase in stiffness of approximately two orders of magnitude when heated and the subsequent recovery after cooling to values before heating and thus the stiffness and temperature sensitivity in addition to the size should allow carrier and scaffold usage.

4.4. Impedance analysis on TGF-β1 carriers in wound healing

In a final set of experiments we were able to combine the produced microfluidic droplets with the cells in an ECIS wound closure study. The droplets were used as the intended TGF-β1 carrier system with fluorescein sodium as optical control for encapsulation, solved in cell culture medium and, therefore, loaded with a concentration of 15ng TGF-β1, due to the cells' typically strong reaction to this concentration during the later stages of an experiment.
Figure 4.27 shows the resistance (Figure 4.27a) and reactance(Figure 4.27b) from an ECIS experiment using the same setup as for previous ones, where fibroblasts were measured together with 15ng TGF-β1 carriers. These were added to each well after wounding and washing the cells in 250µl culture medium. While the resistance seems to be in good agreement with what we would expect and promising for further development, the reactance (Figure 4.27b) would imply that a monolayer has not been recovered, suggesting a distortion of the impedance signal eventually caused by the polymerosomes' passive electrical properties[53].

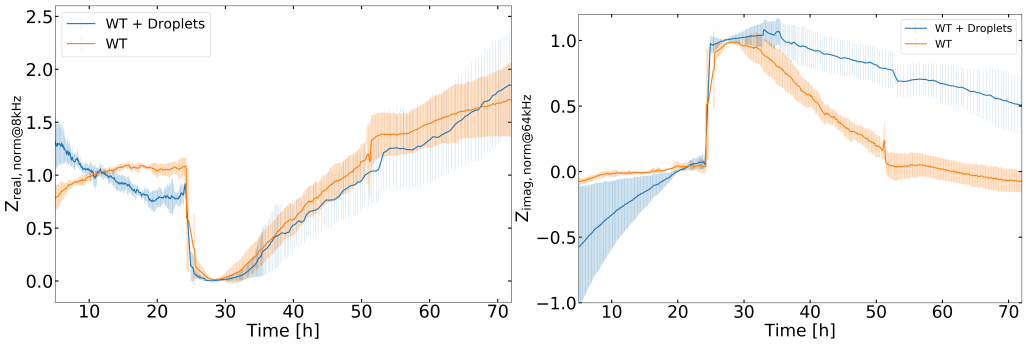

(a) Resistance of 3T3 fibroblasts with (blue) and without (orange) TGF-β1 carriers (blue).

(b) Reactance for 3T3 fibroblast wound healing with (blue) and without (orange) TGF-β1 carriers (blue).

Figure 4.27.: Mean impedance of the monoculture with Droplets results from a static ECIS experiment over four days, averaged over N=5 wells. In good agreement with results seen from 15ng TGF-β1 added directly to cells (Figure 4.12), the resistance a) mainly follows the control cells' behaviour until it shoots above it in later stages approximately 48 h after wounding.

In addition to previous measurements, the ECIS was used in combination with a flow pump setup in order to achieve a more consistent distribution of droplets across the measuring electrodes and between cells unfortunately at the drawback of having less homogenuous cell distribution in the microfluidic channel. For this setup, ECIS chip holder and flow pumps, which later also hold the tubing containing the medium with the droplets, were placed in an incubator typically held at 37°C. The tubing is placed inside the incubator several hours before a flow is started to minimise temperature fluctuations by allowing the material to equilibrate beforehand. This

was not possible for this experiment, because of the temperature responsiveness of PNIPAm. In fact, while the wounding took place, the temperature inside the incubator was reduced to 28°C, a compromise between not significantly disturbing the cells and still lower than pNIPAms LCST of 32°C, where above this temperature their most significant shrinkage, and thus TGF-β1 release, happens, so as to not release all their content beforehand. With the completion of the wounding, the flow in both pumps, each containing TGF-β1 saturated pNIPAm droplets, one for each chip, was activated and let run for about 3min. After turning off the flow, the incubator was returned to its initial temperature of 37°C and with that the TGF-β1 slowly released from the droplets.
In Figure 4.28a the resistance curves of these flow experiments is shown for 3T3 fibroblasts with TGF-β1 carriers in comparison to a control system without carriers. Despite the irregular and almost oscillating curve in the case of control cells, one observation is the faster response time and especially the steeper slope of the recovery curve between hours 50 to 70. However, the reactance, as shown in Figure 4.28b, is not recognizable as a repopulation of the electrode after wounding, which makes further analysis of these experiments not possible, thus leaving it for future investigations.

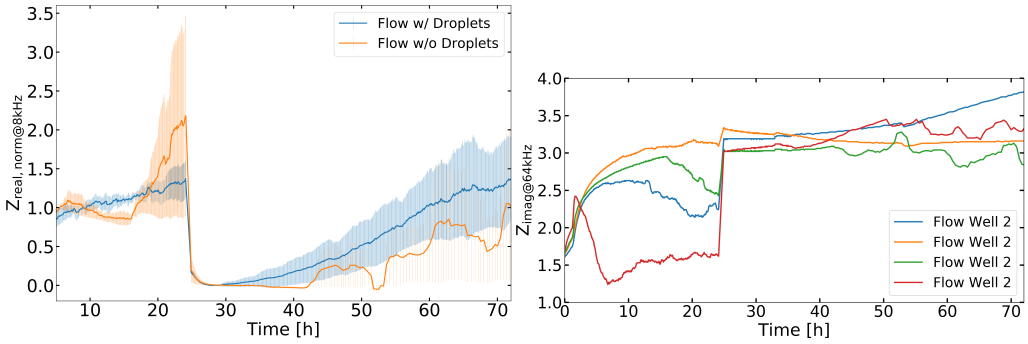

(a) Mean resistance of 3T3 fibroblasts with TGF-β1 carriers (blue) and without them (orange).

(b) Reactance of 4 electrodes of 3T3 fibroblasts with TGF-β1 carriers. The uncharacteristic behaviour makes further evaluations not sensible.

Figure 4.28.: Mean resistance a) and reactance of single electrodes b) in an ECIS flow setup.

Overall, the resulting curves follow the behaviour expected from **??** according to the influence of TGF-β1 concentrations in Figure 4.12 rather well. As such, one can see the similar behaviour of both curves up until the later stages of the experiment. In experiments where TGF-β1 was added directly to cells without droplets, a steep increase could typically be seen from 50h onwards. Here, this is not the case, but rather the response seems slightly delayed with the curve shooting up approximately 20 h later between 60h and 70h.

5. Discussion

In this work, we have studied the applicability of ECIS as a wound healing platform on three sets of experiments:
1. We analysed the role of mDia-family formins 1 and 3 in fibroblast wound healing dynamics through the comparison of wild type, mDia1-, mDia-3-, and both mDia1- and -3-deleted cells impedance throughout wound healing.
2. We studied the influence of TGF-β1 depletion and enrichment on fibroblast wound healing behaviour through the treatment of wild type cells with either an ALKs 4, 5 and 7 inhibitor, blocking the main TGF-β1 signalling pathway, or additional TGF-β1.
3. We analysed the reaction of fibroblast cultures to the addition of pNIPAm carriers and treatment with TGF-β1 through theses carriers in a static and flow environment.
Wound healing experiments with an ECIS set up provide many advantages to other, more conventional wounding assays like scratch, stamp and various barrier assays, as described in subsection 2.1.2, mainly that it is a quantitative and highly reproducible technique that monitors wound healing in real-time.

5.1. Impedance of formin deleted cell cultures

Formins are one of three major classes of actin nucleators next to the Arp 2/3 complex and tandem-monomer-binding nucleators that accelerate the elongation of the barbed ends of an actin filament. Formin mDia1 especially has been shown to play an important role in stress fibre and filopodia formation and the forming of adherens junctions [54]. This is confirmed in the junctional resistance R_b after wounding occurred where 24h after wounding all formin k.o. lines are significantly smaller than wild type R_b, when one would rather expect an equal, if not higher, R_b due to the formation of gap and adherens junctions after at least partial transformation into myofibroblasts. MDia3 seems to have a stronger long term effect on the formation of adherens junctions, as 48h after wounding R_b is still significantly smaller than for wild type and other formin k.o. Surprisingly though, all cell types appear to be forming similar monolayers before wounding. That would mean that wound healing triggers a stronger transformation which is necessary to show the effects of the missing formins.

5.1.1. Formins mDia1 and -3 in wound closure dynamics

Depletion of mDia1 in HeLa cells led to failure of cortical function in cell division, which other important factors for the actin cortex like the Arp2/3 complex did not show the same effects. This suggests a critical function of formins in cell cortex

mechanics, and as such progressive cell movement by filopodia as well as cell division relevant also to wound healing. As such, the study of mDia-deficient fibroblasts might give insight into the dynamics of how fibroblasts close wounds.
mDia subfamily formins 1 and 3 are regulated by RhoA [55], which is well established to drive contractility. Studies comparing the influence of mDia1 and -3 found highly similar results for cells with the deletion of each formin respectively, wich suggests at least some degree of functional overlap. Other compensatory mechanisms have already been implied by groups finding higher mDia1 levels in mDia3 k.o. lines and vice versa. It has been shown, that mDia1 and -3 k.o. cells display a slower migration rate, more so for the the mDia1 and -3 double k.o., which is similarly mirrored in a reduced cell speed, likely caused by inefficient protrusion in a productive direction due to defects in cell polarisation and the formation of multiple cell fronts [56]. This provides a possible starting point for polymeric PNIPAm droplets counteract polarisation defects by being inserted into a cell population as scaffold, as the difference in stiffness between cells and droplets could promote cell polarisation [52]. However, while all formin deleted cells were slower than than wild type cells, such a strong decrease of speed from single k.o. to both mDia1 and -3 deletion as is implied in [52], was not found in experiments for this thesis, rather the contrary in that the mDia1 and -3 k.o. cell lines showed the more pronounced difference from wild type 3T3 fibroblasts on 250 µm electrodes.
The variation from that behaviour of formin double k.o. cells over different electrode, and thus wound, sizes shows a distinction between mDia1 and -3. For smaller wound sizes of 50µm, the deletion of both mDia1 and -3 leads to a similarly slower recovery as the deletion of only mDia1, while the deletion of only mDia3 appears to slow down wound closure only slightly, so that mDia1 seems to become more important for recovery with decreasing wound size.
Publications describing different mechanisms MDCK cells apply to close a wound depending on wound size showed that for smaller wound sizes from 100µm on, closure dynamics change and progression slows down as smaller diameters do not allow wound borders to behave independently [11] with zero to two lamellipodia size extensions [15]. Likely, the longer recovery time of mDia1 and -3 deleted cells compared to only mDia3 deletion indicates different closure dynamics for 50µm wounds. While wound closure through the myosin-mediated contraction of an actin belt, a *purse-string*, is well established as main wound closure mechanism of epithelial cells besides collective cell motility of border cells, a similar phenomenon for fibroblasts is not as well explored. Rather, fibroblasts are known to close wounds by collective migration into the wounded area, similar to the formation of "leader" cells in epithelial tissues. However, recent studies have shown that fibroblasts can form an epithelial-like purse-string and close wounds with up to 300µm gap width through myosin II-mediated contraction [57].
This would mean, that fibroblasts close 50µm wounds mainly through purse-string contraction, and the larger wounds of 125µm and 250µm by a combination with established collective motility in the style of epithelial cells. Following this analogy, mDia1 formin appears to be especially important for the closure of small wounds, the loss of which cannot be compensated by higher mDia3 levels, contrary to larger wounds.

This, however, directly contradicts the findings in [58], where the authors found that the depletion of mDia1 in migrating epithelial monolayer results in dissociation of leader cells and impaired wound repair. But mDia1 might be more important for leader cell dynamics the more the cells are polarised or exhibit epithelial-like structures, too.
With this the need for follow up studies of other kinds like optical shape and recovery correlation and micromotion analysis supplementing these findings in order to draw specific conclusions becomes apparent, as the observed differences on 50µm electrodes might prove to be significant, and for that the current statistics need to be increased, too. Thus further experiments could further confirm wound size-dependent closure dynamics of fibroblasts and a distinction in the roles of formins mDia1 and -3.

5.1.2. Formin deletion reduces junctional resistance R_b

Interesting to note, is the behaviour of R_b next to $t_{1/2}$ for the deletion of mDia3, assuming a monolayer is recovered 48h after wounding. At that point for 250µm electrodes the junctional resistance is significantly smaller than for wild type and the other formin k.o. cell lines, and the recovery time is significantly higher. While the recovery time for mDia1 deleted cells is higher for all electrode sizes, a tendency as for the formin 3 k.o. is not apparent, which seems to imply a stronger correlation for cells without mDia3 between loss of adherens junction and wounding time. A similar connection was shown in [57], where the authors determined intercellular adherens junctions as a crucial factor during wound closure in the context of collective sheet migration. The strongest difference from the wild type recovery time is observed for 250µm electrodes This further supports the impression of mDia1 playing a more important part in purse-string-like closure, and mDia3 in collective cell sheet migration.

5.1.3. Cell-substrate distance increases after wounding

Previous publications like [16] and [59] showed that α as a measure of cell-substrate distance derived from the ECIS model by Lo and Ferrier [34] tends to be significantly smaller for fibroblast cultures after wounding than before, meaning that the cells are more erect on the substrate after wounding. This behaviour is also seen in the fibroblast cultures from this work with a sharp drop in α 24h after wounding and no tendency to recover to an earlier level with time. For this point in particular further analysis of the cells' micromotion monitored through fluctuations in the impedance and given further significance by appropriate modeling may reveal if mDia3-deleted cells are slower in their recovery as well [20]. However, with the deletion of mDia formin 3, α appears to be less sensitive to wounding and the reaction to this event slowed down. Interestingly, cells with mDia1 and -3 deleted, seem to approach the substrate slightly 48h after wounding. To determine such a tendency, measurements over a longer recovery period of three to four days are necessary.

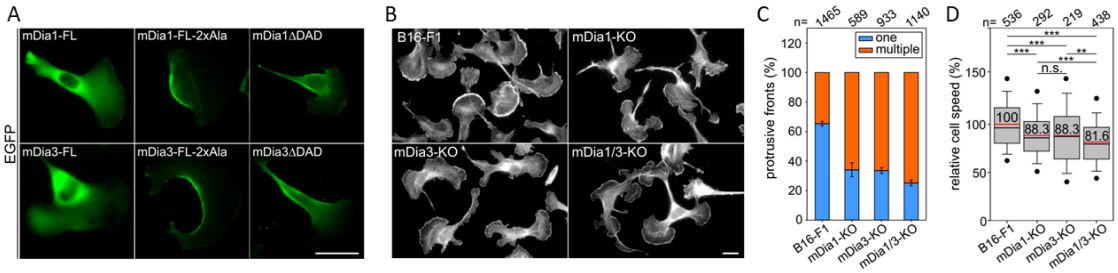

Figure 5.1.: Fibroblast like mouse melanoma cells B16-F1 displayed pronounced problems in regulating cortical tension and adhesion in mDia3-deleted cells, leading to transcellular holes (A) and increasing defects in polarisation dynamics and protrusive front formation for individual mDia1 and 3 k.o. and the combined double k.o. (B,C,D). Figures reprinted and indexing adjusted with permission from [56].

However, this increased cell-substrate distance together with the the strong increase in C_m of $(9.7\pm3.2)^{**}$ µFcm^{-2} 24 h and (7.8 ± 0.1) µFcm^{-2} 48 h after wounding observed in mDia3-deleted cells compared to the wild type with (2.1 ± 1.1) µFcm^{-2} and (4.0 ± 1.3) µFcm^{-2} , and even the mDia1 k.o. with (1.7 ± 0.3) µFcm^{-2} and (1.062 ± 0.021) µFcm^{-2} for each time after wounding respectively, implies stronger cell shape changes than ruffling. This is reminiscent of a phenomenon observed in [56] for fibroblast-like mouse melanoma cells B16-F1, which is shown in Figure 5.1 for reference. In this study on the impact of mDia-related formins 1 and 3 deletion, the authors found a pronounced formation of transcellular holes in mDia3 deleted cells, which are apparent in the fluorescent micrograph in Figure 5.1 A.
The occurrence of such holes due to an imbalance of cortical tension and adhesion in mDia3 k.o. cells would be a likely explanation for the increase in C_m we found, especially after wounding.
At the same time, the authors also found increasing cell polarisation defects from individual formin 1 and 3 deletion to the combined double k.o. cells. This is shown in Figure 5.1 B where the formation of protrusive fronts for wild type, single and double k.o. cells is emphasised through phalloidin staining, with a quantitative analysis of this behaviour shown in Figure 5.1 C and D. However, in the analysis of recovery time and rate in this thesis a pronounced impact of such polarisation defects for mDia3 and the double k.o. could not be detected, as mainly the mDia1 k.o. cells displayed a generally slower recovery.

5.2. Impedance of cell cultures with TGF-β1 (inhibitor) treatment

In a similar approach we considered how TGF-β 1 concentration influences wound healing through treatment of 3T3 wild type fibroblast cultures with either additional TGF-β 1 or a TGF-β 1 inhibitor.

5.2.1. Recovery time with TGF-β1

In contrast to formin deletion, inhibition of TGF-β1 signalling does not slow down the recovery significantly, and rather speeds it up depending on the concentration. As such, recovery is fastest with 15ng inhibitor (11.0±3.3)h and 5ng TGF-β1 (11±5)h. While a faster recovery with 5ng TGF-β1 is not surprising considering the higher junctional resistance due to optimal fibroblast-to-myofibroblast transitions, found for the same concentration, the equal recovery time with 15ng inhibitor is unexpected. This means that with both treatments, wounds close approximately 28% faster than untreated cells, with a a good margin to the next fastest recovery with 10ng TGF-β1 and approximately 11% shorter recovery time.
The closest comparable recovery times were found for 50µm electrodes with (9±3)h for wild type and (11±3)h for mDia3 k.o. cells.
However, while the recovery rate $r_{1/2}$ shows the expected inverse behaviour for TGF-β1 concentrations up to 15ng, with 25ng TGF-β1, $r_{1/2}$ is higher despite an overall slower recovery time $t_{1/2}$. Similarly, $r_{1/2}$with TGF-β1 inhibitor is steadily higher than for untreated cells and cells with TGF-β1, and only decreases with the addition of 200ng inhibitor.

5.2.2. Junctional resistance R_b implies optimal TGF-β1 concentration

The junctional resistance for different cytokine concentrations shows a similar tendency. Treatment with 15ng inhibitor induces a smaller R_b of (1.5±0.9), suggesting fewer adherens and gap junctions than untreated cells (2.1±1.1), an indication towards fewer fibroblast-to-myofibroblast transitions. Analogous to [60], treatment with 5ng TGF-β1 induces slightly higher R_b , which suggests more cell-cell junctions due to enhanced fibroblast-to-myofibroblast transitions.
However, with the addition of 25ng TGF-β1, R_b is significantly smaller than for unperturbed cells.
This might indicate a critical oversaturation, where TGF-β1 signalling is even more strongly reduced than through selective inhibition by inhibitor concentrations up to 200ng.
This is likely due an intrinsic regulatory mechanism reacting to the amount of TGF-β1, and needs to be further investigated for a better understanding of the impact of TGF-β1 on the fibroblast-to-myofibroblast transition. This non-linear dependency on TGF-β1 concentration is reminiscent of the role of Connexin43 (Cx4) in co-cultures of cardiomyocyte-myofibroblast dynamics as proposed in [61].
Figure 5.2 shows a schematic of the dependency of high electrical coupling, thus successful dynamism, and an optimal amount of Cx43. Here, the authors propose that a small amount of Cx43, thus low dynamism leads to low electrical coupling, in a similar way as high amounts of Cx43 with high dynamism. As such, an optimal point with high electrical coupling was found in between (Figure 5.2, point a) and could be further optimised through the addition of αCT1 to yield even stronger electrical coupling (Figure 5.2, point d).
Looking agagin at the resulting junctional resistance R_b , we find a similarly decreasing R_b in both directions from 5ng TGF-β1. Although, R_b decreases irregularly, this

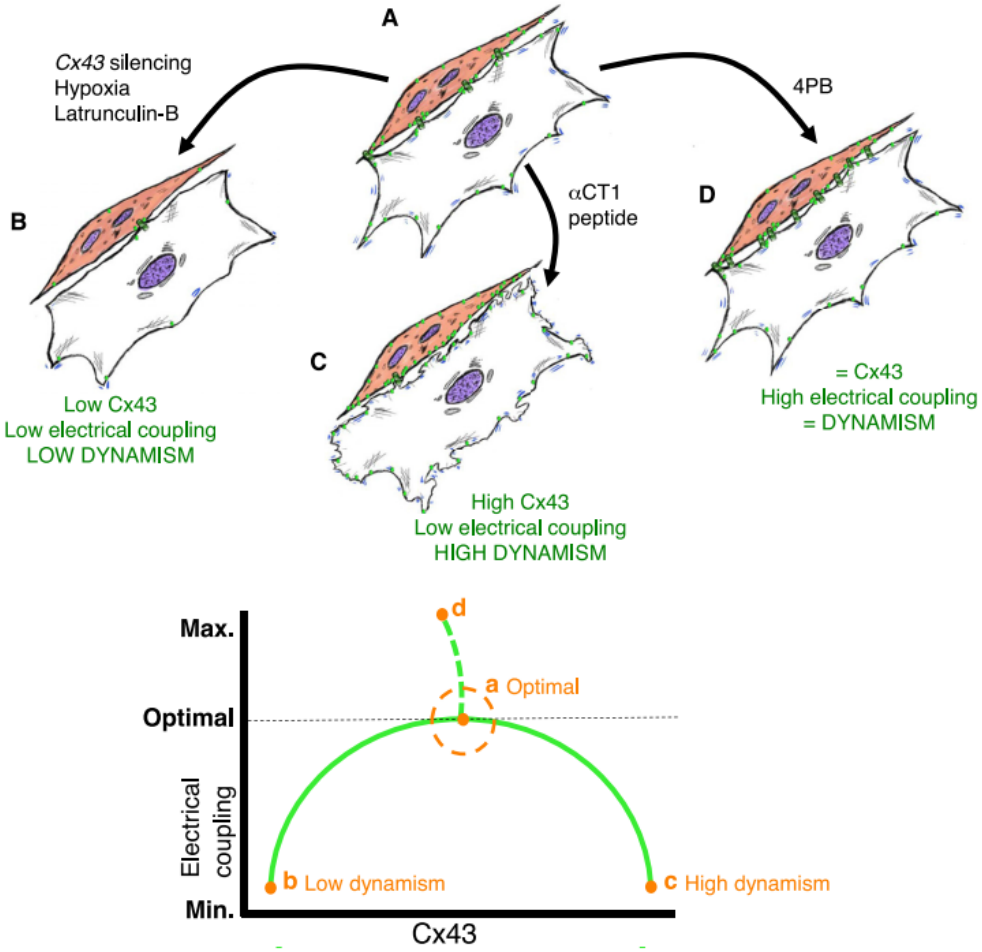

Figure 5.2.: A schematic from [61] on the role of Cx43 in cardiomyocyte-myofibroblast dynamism as introduced by the authors. The idea of an optimal amount of Cx43 for balanced dynamism and high electrical coupling bears a strong resemblence to the effect of 5ng additional TGF-β1 on the junctional resistance R_b, with higher and lower concentrations showing suboptimal results.

concept seems to be provide a good foundation for an adapted model of the effect of TGF-β1 on the fibroblast-to-myofibroblast transformation.
At the same time this decrease for TGF-β1 treatment above 5ng is similar to the to the epithelial-to-mesenchymal transition through three distinct phases as proposed in [49]. Here, the authors suggest that cells go through two distinct transitional states that are reflected in the impedance:
During the first phase approximately 4 to 9h after TGF-β1 treatment, they observed an increase of impedance fluctuations due to increased micromotion which they interpreted as an increase in cell-substrate dynamics as thermal undulations or membrane ruffling and actomyosin contractility.
Similar to this, we find a distinct TGF-β1 concentration-dependent increase in average membrane capacitance C_m 24h after wounding, which indicates a larger membrane surface or a significant change in membrane lipid composition. In this

way a higher C_m is more likely to indicate membrane extensions and deformations like ruffling.
During the second phase appoximately 10 to 30h after TGF-β1 treatment, they could observe a distinct dissolution of cell-cell contacts and enhanced stress fibre formation coupled to reduced barrier resistance and impedance fluctuations.
In analogy to a mesenchymal-ephithelial transition, we would expect enhanced cell-cell contacts and stress fibre formation for enhanced transformations to myofibroblasts. For 5ng TGF-β1 that is exactly what we see in an increased R_b and decreased C_m, compared to all other treatments 48h afterwards.
The considered time frame is however very different, as the epithelial-to-mesenchymal transition is characterised over 30h after TGF-β1 treatment, while we are considering different states 24 and 48h after wounding. This is also due to the fact, that wounding healing requires different cell dynamics and further differentiation of cell-cell contacts and fibroblast-myofibroblast morphology mainly occurs after 24h when the wound is mostly healed. This is confirmed in the reduced C_m only 48h after wounding, suggesting that indeed further differentiation due to wound healing requires measurement over at least 48h after wounding to be quantitatively evaluated. However, the loss in R_b 24h after wounding and TGF-β1 treatment inversely TGF-β1 concentraton-dependent above 5ng not only implies an optimal concentration as mentioned above. This atypical decrease implies a more mesenchymal-like transition, where cell-cell contacts are further reduced.
However, the concentration-dependent increase in C_m implies a larger membrane surface which would most likely be achieved through ruffels. Also, the cells seem to recover this loss in cell-cell contacts 48h after wounding, which might indicate the transition through a mesenchymal-like state triggered by additioinal treatment with TGF-β1 exceeding 5ng.

Interestingly, in [51] the groups showed that the inhibition of pro-fibrotic signalling through the same ALK5 inhibitor enhances the reprogramming of cardiac fibroblasts to induced cardiomyocytes. This might be a factor to consider for further cardiomyocyte-fibroblast co-culture experiments, as on one hand enhanced fibroblast-to-myofibroblast transitions tend to close a wound faster, but on the other hand excessive myofibroblast formation may lead to fibrosis and cause further cardiac arrhythmia and infarction. This is further supported by [62], where the authors found that electric conduction in fibrotic monolayers is slowed by mechanic coupling between myofibroblasts and cardiomyocytes.
Another point point that makes the interpretation of different TGF-β1 inhibitor concentrations difficult, is the selective inhibition. Due to inhibitor and TGF-β1 molecules competing for the ALK5 binding site, a specific estimate for an active TGF-β1 concentration or the relative reduction of the same, is not possible. Additionally, a detailed kinetic analysis on the ability of A-83-01, the inhibitor used throughout these experiments, to inhibit ALK4, ALK5 and ALK7 is missing, and potential off-target inhibitions of p38α , MAPK, PKD1 and FGF-R1 have been reported [63]. As such, the authors recommend the inhibitor SB-505124 for inhibition of ALKs 4, 5 and 7, when targeting TGF-β1 signalling pathway, in terms of specificity and potency.

In order to better relate the acquired results to TGF-β1 concentration, it will be necessary to correlate inhibitor concentration to TGF-β1 concentration and possibly make adjustments accordingly for the administration through pNIPAm carriers. For all experiments on the impact of TGF-β1 concentration, cytokines were solved in cell culture medium before added to wounded monolayer. As such, cytokines are distributed more evenly over the culture than through carriers, that create locally higher concentrations in the direct vicinity of the droplet.

5.2.3. Implied transformation phases in α

So far we could tell from previous studies and the formin k.o. experiments done in this work that usually α is smaller after wounding than before, meaning, cells seem to raise themselves higher above the substrate than before wounding.
An exception to this behaviour, however, is triggered by blocking the TGF-β1 receptor. 24h after wounding and administration of 200ng ALK5 inhibitor, α is significantly higher than for unperturbed cells and roughly equals α before wounding. During that phase, α also increases with inhibitor concentration, with the notable exception of 100ng ALK5 inhibitor. Over a longer time, this impact of reduced TGF-β1 on the cell-substrate distance, grows more pronounced, as 48h after wounding α for cells with inhibited TGF-β1 to any degree, is equal to pre-wounding α. This implies a stronger impact of TGF-β1 during the third phase, 45-48h after wounding, where a confluent monolayer has been recovered and also underlines that even 48h after wounding further cell differentiation takes place.
In ECIS experiments on the influence of TGF-β1 on the epithelial-to-mesenchymal transition, a similar correlation was found with α decreasing with cells subjected to increasing TGF-β1 concentrations [49]. This is the same trend, that we also see for the addition of TGF-β1 to fibroblast cultures. Notably, 15ng TGF-β1 is an exception in both cases with α slightly higher than for the addition of 10ng, but still smaller than for 5ng TGF-β1.
Such a change may be an indication of fibroblast-to-myofibroblast transitions, as a characteristic of myofibroblasts is the production of not only α-SMA, but also excessive ECM proteins [60].
However, the impact that the inhibition of TGF-β1 has on fibroblast transformation is ambiguous. In [60] the authors showed that not only does the ALK5 inhibitor suppress myofibroblast population in rat skin burn wounds in vivo, but also suppresses the transformation of dermal fibroblasts to myofibroblasts. This was determined from the reduced expression of Smad2, α-SMA and secreted collagen type I, with respective IC_{50} of approximately 20 to 30ng.

5.2.4. TGF-β1 and wounding as synchronisation stimulus

Looking at the temporal development of α and C_m for fibroblasts with TGF-β1 (inhibitor) treatment and mDia-deletion, we find that α and C_m are spread over a considerably wider distribution before wounding than after, therefore their postwounding behaviour is reminiscent of a reaction to a synchronisation stimulus.

This effect is pronounced in untreated wild type fibroblasts, while especially mDia3-deficient fibroblasts do not exhibit this trend either in α or C_m.
In [64], the authors found that a heat shock pulse of 43°C over 30 min can synchronise NIH-3T3 fibroblasts over the entire culture.
The wounding of the monolayer through short high-voltage pulse might trigger a similar synchronisation of cell phases, though not to a similar extent. [64] further indicated that already a slightly raised temperature of 38.5°C acts as a resetting cue and although the ECIS wounding pulse is restricted to the working electrode, heat-transfer across border cells, as mentioned above, is not controllable or quantified. However, the optimal duration for such a resetting heat pulse was found to be 30 min, whereas the wounding voltage is applied for 2 min, which would at most slightly impact border cells only. As the heat generated during the wounding can be assumed to be higher than 40°C, although shorter, the wounding event as a low-key synchronisation stimulus may explain this behaviour.
This reduced distribution of α and C_m after wounding, and even further over time, is even pronounced more strongly in fibroblast cultures treated with TGF-β1, so possible two additive synchronisation effects. In contrast to the typically used serum shock to synchronise cells, this effect appears to be caused along the TGF-β1 pathway, as with increasing TGF-β1 concentration administered, the distributions become smaller, with the exception of 15ng TGF-β1. An increase of inhibitor concentration, thus further decrease of TGF-β1, shows the inverse tendency up to 15n: While the distributions are still smaller after wounding than before, they increase relative to each other with increasing inhibitor concentration.
Following the suggested analogy of cell synchronisation, this dependency on TGF-β1 concentration may indicate that TGF-β1 supplies a similar synchronisation stimulus or supports the one given through the wounding.

5.3. Impedance of cell cultures with TGF-β1 carriers

In a first series of experiments aimed at influencing fibroblast wound healing through the addition of TGF-β1 in pNIPAm carriers, and test the cells reaction to the synthetic component, the carriers were filled with 15ng TGF-β1. This concentration was chosen because while treatment with 5ng TGF-β1 induced stronger changes in R_b with an overall faster recovery time, with 15ng TGF-β1 fibroblasts showed a stronger impact during the third phase. This is added to the fact, that the TGF-β1 concentration inside the droplets will already be smaller, after washing them during production. We have to further consider the loss of cargo due to Brownian motion, thus TGF-β1 molecules diffusing out of the droplet. This amount has not yet been quantified and will be needed as critical information on carrier properties.
In contrast to a quantitative determination of the tightness of the polymeric droplet mesh, the analysis of particle diffusion out of the carrier in different states, meaning above and below the LCST, thus also providing a quantitative assessment of release radius and efficiency, can and has to be done more easily through the use of fluorescence recovery after photobleaching (FRAP)[65].
Additionally, the TGF-β1 concentration throughout the culture will have strong local gradients depending on the vicinity to the TGF-β1 carrier, than the more even

distribution throughout the medium in the case of global TGF-β1 administration. By administering an incidentally higher concentration, the effective amount of TGF-β1 reaching the surrounding fibroblasts varies over a range that still affects the cells and enhances fibroblast-to-myofibroblast transitions.
At this point, where we need to assume a certain loss of cargo between production and administration of carriers, the initial loading with 5ng TGF-β1 would be further reduced and while we did not find a sufficient effect for concentrations below 5ng, in the range below 15ng we did and therefore decided for 15ng.
By administering the carriers through a flow system, we thought to promote a more

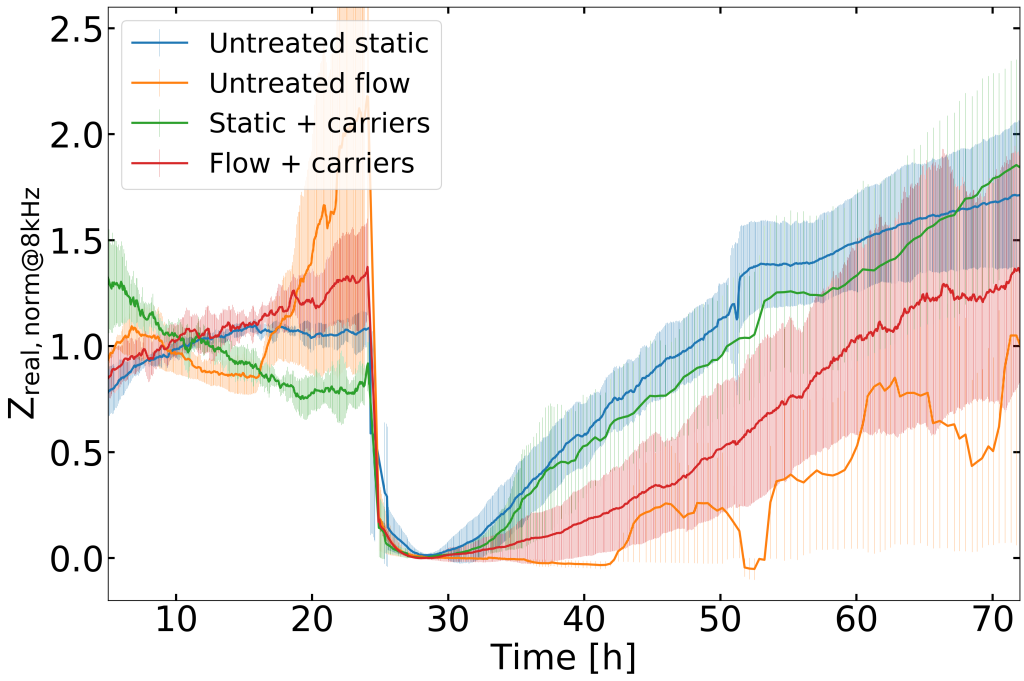

Figure 5.3.: Mean resistance of 3T3 fibroblasts with (green) and without (blue) TGF-β1 carriers in a static set up in compared to a flow set up (yellow, red).

even distribution of the carriers over the monolayer. While local gradients would still be present, this flow set up would ensure a wider spread.
Figure 5.3 shows the direct comparison of the resistance in a flow set up with a static set up, for 3T3 fibroblast cultures with and without TGF-β1 carriers. Here, we see an overall stronger recovery signal in the static system than with flow pumps, for unperturbed cells as well as with carriers. This might be due to a smaller cell density on the electrodes of the flow chip. Although the same overall cell density of $1x10^{-6}$ per ml was used for both experiments, the same amount of 250µl that is given into each well, thus onto each electrode pair, for a static set up, is distributed over all eight electrodes in a flow chip, through capillary motion. Thus it remains to be elucidated, that not all electrodes were sufficiently occupied, thus further indicating a lower cell density.
This might explain the slower recovery in both flow curves, which makes a specific conclusion as to the more efficient carrier distribution difficult. However, cultures

with carriers in the flow set up, appear to react more strongly than in the static set up, recover the resistance amplitude of the initial monolayer and have almost caught up to the resistance level of cells in the static set up. This could mean that cells that are already in a

This might also indicate a more efficient ratio of droplets to cells, thus more balanced intake. On the downside, it may also be a sign of a larger amount TGF-β1 being dissolved in the culture medium through the pumping, thus creating a situation similar to the direct treatment with TGF-β1.
Such a strong variation is not found in the static system, as both curves are very similar, with the resistance of cells with TGF-β1 carriers even slightly below that of untreated cells. The resistance of fibroblasts treated with 15ng TGF-β1 closely resembled untreated cells up to approximately 48h, and afterwards strongly rose and resembled treatment with 5ng TGF-β1. A longer experiment duration might give more insight into this effect. This might also imply, a delayed intake of TGF-β1 when applied through the carriers than directly to the cells. The slower recovery might also be caused by an accumulation of too many carriers inside the wounded area, in contrast to the flow system, where they are distributed over the entire monolayer.
This possibility is further supported by the reactance of fibroblasts with and without droplets in a static set up, shown in Figure 4.27b. With the addition of TGF-β1 carriers fibroblasts do not seem to fully repopulate the electrode, as the imaginary impedance as reactance, which gives insight into the coverage of the electrode, stays significantly above the level indicating that full coverage is delayed.. This may further be an indication of the distortion of the capacitance through pNIPAms electrical properties.
In [53], the authors studied the electrical conductivity of pNIPAm droplets in solution in relation to that of deionized water. They found that with increasing temperature, conductivity steadily drops to a minimum value for 32°C, where the behaviour is inversed and electrical conductivity steadily rises up to 37°. This electrical conductivity is dependent on the rheological properties of the pNIPAm droplets and its hydration dynamics. Therefore the electrical impact on an ECIS measurement depends on the crosslinker concentration used for carrier production, due to the different reactivity ratio to NIPAm monomers during the polymerisation which leads to slightly uneven distributions, thus heterogeneous chain density [66].

In this sense, the difference in reactance might just be a general contribution of the carriers remaining between the cells during and after repopulation of the electrode, or even imply, that the cells are not able to occupy the electrodes due to the pNIPAm droplets. In order to determine the specific effect of pNIPAm on the impedance, and the reactance specifically, in relation to electrode coverage, optical evaluations of different states during recovery are needed, as only then, further quantification of R_b, α and C_m after the Lo/Ferrier model is meaningful both for particles as well as cell cytoskeleton.
Another consideration is the sudden change in sampling for all measurements with TGF-β 1 carriers. This is most likely due to a software issue, and was not intentional, and had seemingly little impact on resistance and reactance.
However, more experiments for a better statistic are vital and a comparison to the

treatment with 5ng TGF-β 1 carriers might give important insight into the loss and release efficiency of pNIPAm carriers.

5.4. General experimental considerations

There are, however, more general experimental influences on the cultures that have to be considered in the interpretation of results.
While wound diameter and time is well controlled, the damage that border cells might take is unknown, as heat may transfer to cells outside the wound diameter and such heat development may affect cell viability. At the same time, the number of cells destroyed is generally high, leaving many remaining fragments in the wound. To remove these fragments, the cultures are washed three times with 500µl cell culture medium, however, if and how much remains cannot be determined from the impedance, which is similar for mechanical
Another point to consider in the interpretation of the impedance are the limitations of the model introduced by Lo and Ferrier [34] that was used for quantitative evaluation of R_b, α and C_m. If the cell shape changes too strongly during the experiment and the assumed rectangular shape can not apply any longer, the fit needs to be modified. One should keep in mind that the starting point for this model is the assumption of a continuous monolayer of cells. For 24 h, upon subconfluency, an extension of the existing fit taking into account different stages of confluency, coupled with direct optical correlation of cell shapes and at later times possibly overcrowding, might provide a more detailed and reliable account of healing dynamics, especially when considering cardiomyocyte-fibroblast co-cultures.
Further, evaluation of the parameter α not only includes the height of the substrate-membrane cleft but also the conductivity in this cleft. As such, changes in α may also indicate changes in the specific electrolyte resistance in the subcellular cleft, which might indicate a change in the extracellular matrix (ECM).

In summary, we find that wound modeling and the manipulation of wound healing behaviour is possible.
We found a pronounced response to the treatment of 3T3 fibroblasts with 5ng TGF-β 1 inducing enhanced fibroblast-to-myofibroblast transitions that were confirmed in quantitative evaluation of recovery time and rate as well as increased cell-cell connectivity and smaller cell surface area.
Further a tendency for cell phase synchronisation was observed triggered by the wounding and further increasing with TGF-β 1 concentration.
On the other hand, we studied fibroblast wound healing dynamics by considering mDia formin 1, 3 and both 1 and 3 k.o. cells on different electrode diameters. This allowed us to study the healing behaviour for different wound sizes and the effects of the formin-deletion.
From this we could deduce that there appears to be a switch in wound healing dynamics for wounds between 50 and 125 µm diameter. At the same time, this implies that mDia1 formin seems to be more active in the closing of smaller wounds as shown in the 50µm electrode, whereas mDia3 formin plays a more significant part

in the closure of larger wounds of at least 125 µm.
Overall, wound healing was disrupted to a different extent for all formin-deleted cells with longer recovery times, suggesting polarisation problems of the cells.
This provides us with an additional handle to enhance wound healing using pNIPAm cytokine carriers. Not only were the first experiments promising concerning the delivery of TGF-β 1 and the cells' acceptance of this synthetic component, but the stiffness ratio could work in favour of using pNIPAm carriers as wound scaffold to enhance polymerisation.
The experiments done so far still need to be expanded towards different cytokine and carrier concentrations and towards a quantification of release efficiency.
In that sense we can be optimistic to have found a solid foundation which opens several ways for further research and at the same time still offers room for further development.

A. Microfluidics

A.1. Variation of crosslinker concentration

The following appendix presents selected bright field and fluorescent micrographs for the variation of crosslinker concentration from 0.3% to 3.0%, 4.0% and 5.0%. The instabilaty of most of these conditions are the reason for the decision against higher concentrations and to instead stay in the range of 1.5% crosslinker concentration which has been shown in the main part of this work.

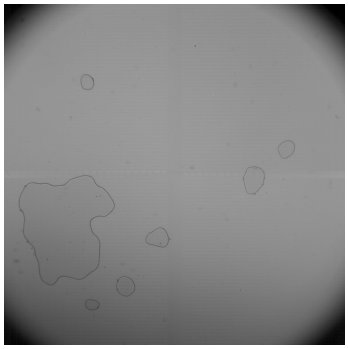

Figure A.1.: PNIPAm solution with 0.3% (v/w) crosslinker could not polymerise properly.

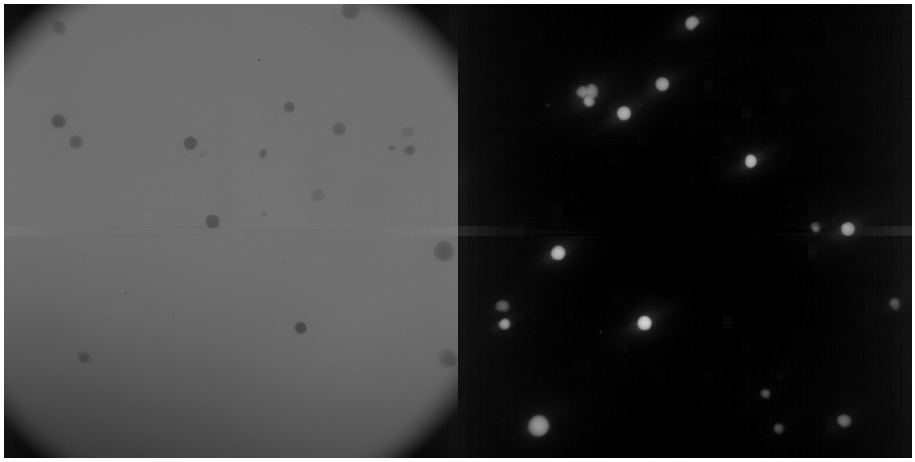

(a) Bright field micrograph (b) Fluorescent image

Figure A.2.: PNIPAm solution with 3% (v/w) solution is saturated and polymeric residue is increasing.

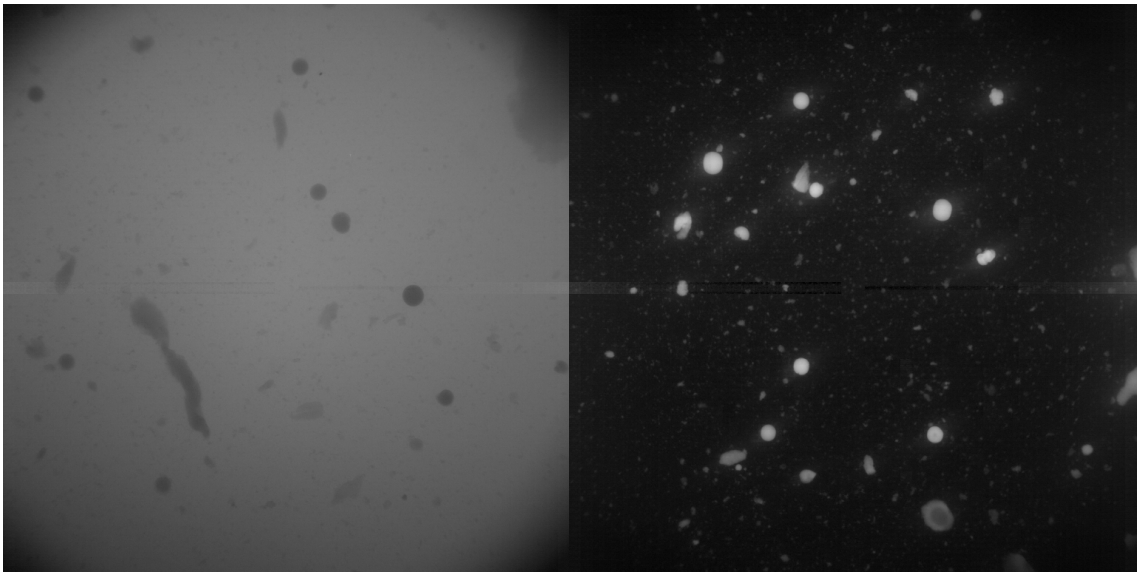

(a) Bright field micrograph (b) Fluorescent image

Figure A.3.: PNIPAm solution with 4% (v/w) solution is saturated and polymeric residue is increasing.

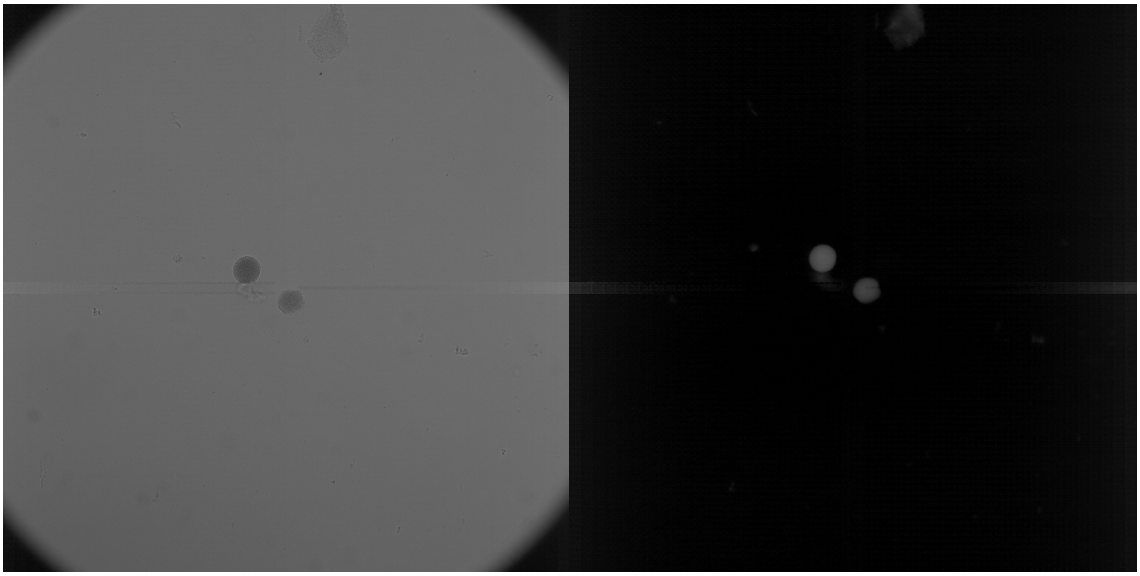

(a) Bright field micrograph (b) Fluorescent image

Figure A.4.: PNIPAm solution with 5% (v/w) solution is oversaturated and not stable.

A.2. PNIPAm Droplet sensitivity

The following appendix shows the remaining micrographs taken for the analysis of droplet shape recovery and their sensitivity to thermal cues.
For this we show one series of the measurment taken with a 10x objective in Figure A.5 and one with a 20x objective in Figure A.6.

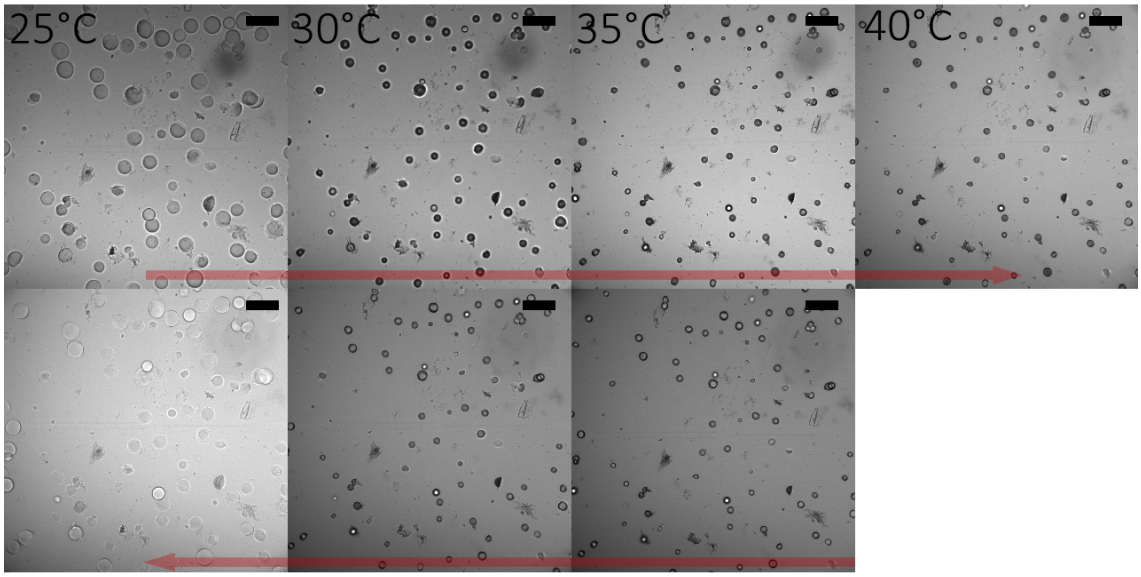

Figure A.5.: Droplets' thermal response and shape recovery for increasing temperature (top red arrow) from 25°C to 40°C, and decreasing temperature (bottom red arrow) in steps of 5â¦C. Micrograph taken with a 10x objective. Scale bars=200 µm.

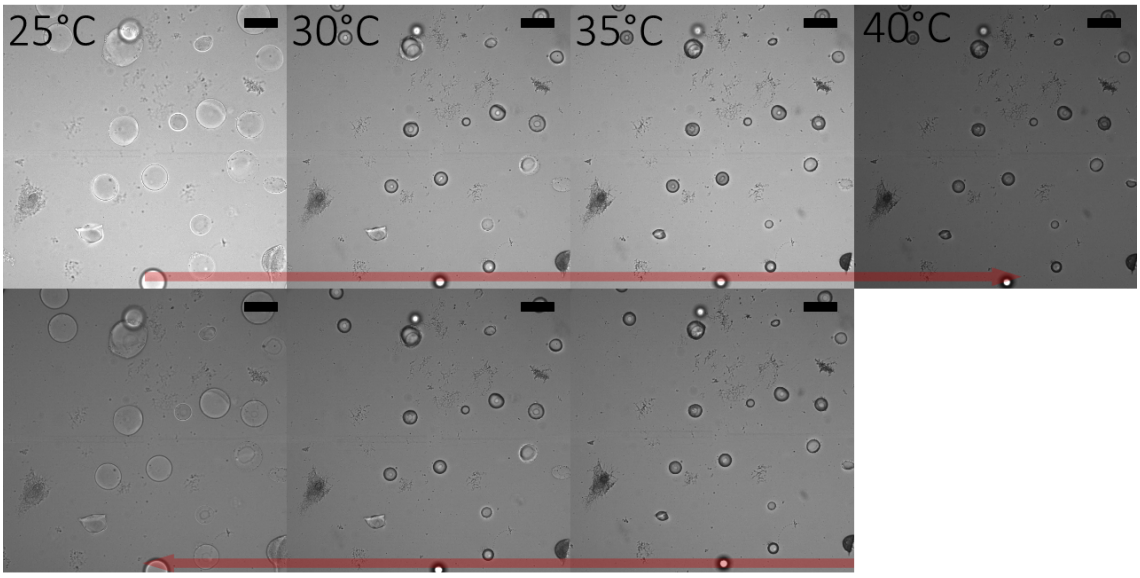

Figure A.6.: Droplets' thermal response and shape recovery for increasing temperature (top red arrow) from 25°C to 40°C, and decreasing temperature (bottom red arrow) in steps of 5â¦C. Micrograph taken with a 20x objective. Scale bars=100 µm.

B. ECIS Measurements

B.1. Formin-deleted cells on 50 µm electrodes

The following appendix shows the mean impedance for mDia-related formin 1-, 3- and both 1- and 3-deleted 3T3 fibroblasts on 50 µm electrodes, in analogy to the results presented for 250 µm electrodes.
R_b , α and C_m according to the Lo and Ferrier model are shown for the 50 µm electrode as well.

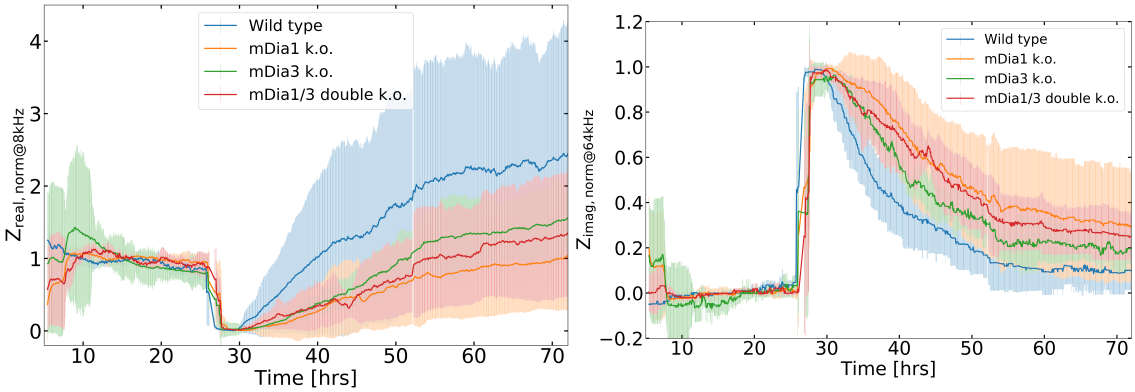

(a) Normalised mean resistance and standard deviation for wild type 3T3 fibroblasts, mDia1, mDia3 and mDia1/3 double k.o. cells on 50 µm electrodes.

(b) Normalised mean reactance and standard deviation for wild type 3T3 fibroblasts, mDia1, mDia3 and mDia1/3 double k.o. cells on 50 µm electrodes.

Figure B.1.: The statistic was taken over N electrodes with n_c cell cultures with N=3, n_c=3 for wild type, mDia1 k.o. and mDia1/3 double k.o. cells.

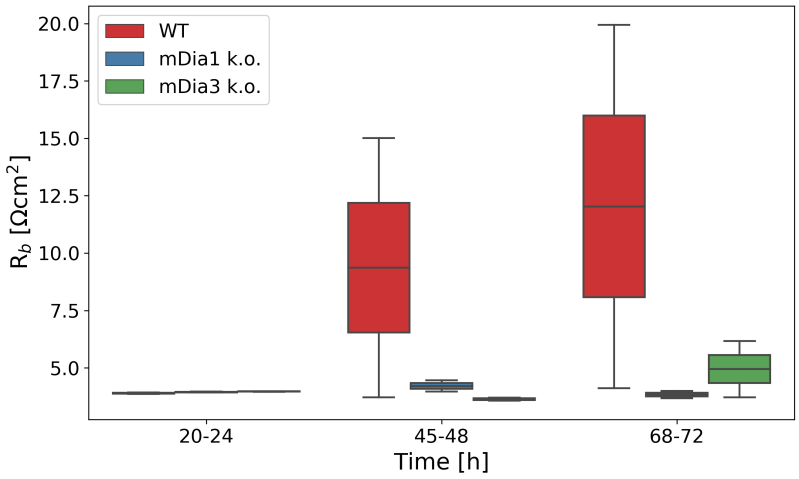

Figure B.2.: R_b distribution of wild type, mDia1, mDia3 and mDia1/3 double k.o. fibroblasts on 50 µm electrodes over time. With N, the total number of electrodes out of n experiments with n_c different cell cultures: N=3, n_c=3 for wild type cells, mDia1 and mDia1/3 double k.o. and mDia3 k.o. N=0. ♦ outliers.

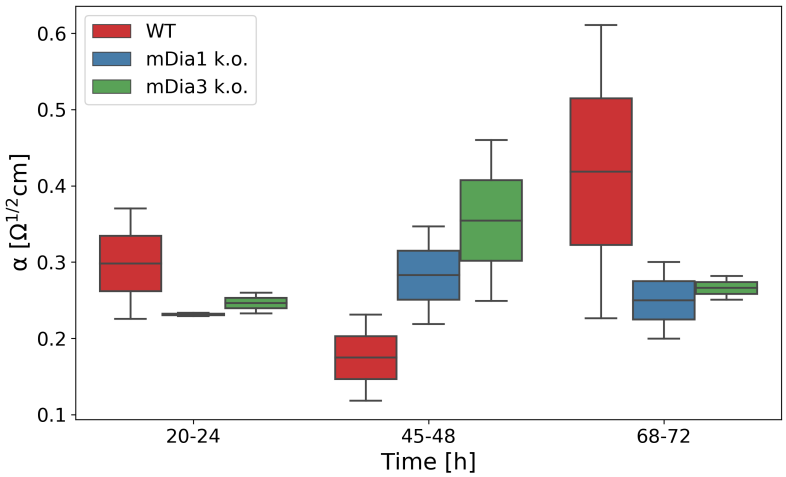

Figure B.3.: α distribution of wild type, mDia1, mDia3 and mDia1/3 double k.o. fibroblasts on 50 µm electrodes over time. With N, the total number of electrodes out of n experiments with n_c different cell cultures: N=3, n_c=3 for wild type cells, mDia1 and mDia1/3 double k.o. and mDia3 k.o. N=0. ♦ outliers.

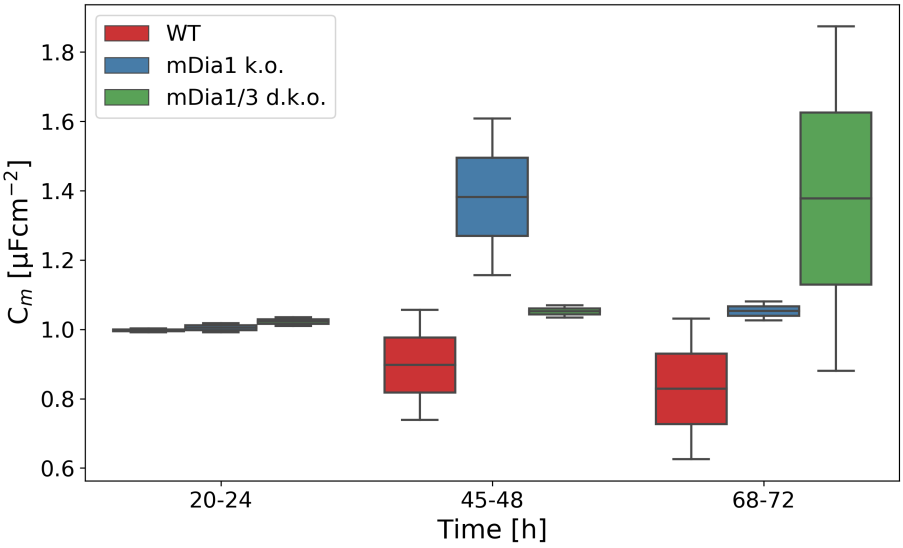

Figure B.4.: C_m distribution of wild type, mDia1, mDia3 and mDia1/3 double k.o. fibroblasts on 50 µm electrodes over time. With N, the total number of electrodes out of n experiments with n_c different cell cultures: N=3, n_c=3 for wild type cells, mDia1 and mDia1/3 double k.o. and mDia3 k.o. N=0. ♦ outliers.

B.2. Formin-deleted cells on 125 µm electrodes

The following appendix shows the mean impedance for mDia-related formin 1-, 3- and both 1- and 3-deleted 3T3 fibroblasts on 125 µm electrodes, in analogy to the results presented for 50 and 250 µm electrodes.
R_b , α and C_m according to the Lo and Ferrier model are shown for the 125 µm electrode as well.

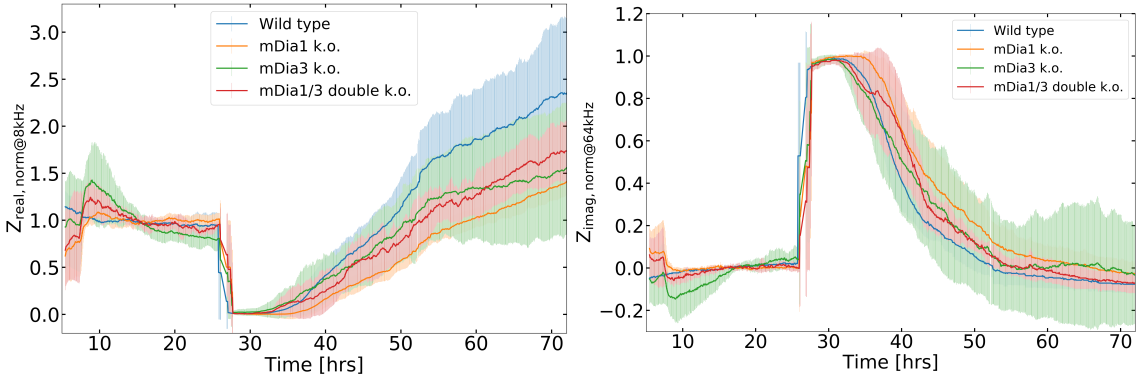

(a) Normalised mean resistance and standard deviation for wild type 3T3 fibroblasts, mDia1, mDia3 and mDia1/3 double k.o. cells on 125 µm electrodes.

(b) Normalised mean reactance and standard deviation for wild type 3T3 fibroblasts, mDia1, mDia3 and mDia1/3 double k.o. cells on 125 µm electrodes.

Figure B.5.: The statistic was taken over N electrodes with n_c cell cultures with N=5, n_c=4 for wild type, mDia1- and mDia3-deleted cells and N=5, n_c=5 for mDia 1/3 double k.o. cells.

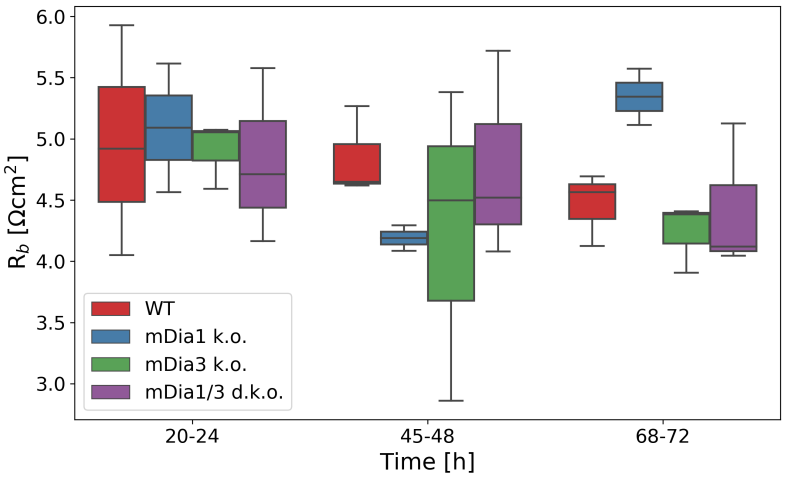

Figure B.6.: R_b distribution of wild type, mDia1, mDia3 and mDia1/3 double k.o. fibroblasts on 125 µm electrodes over time. With N, the total number of electrodes out of n experiments with n_c different cell cultures: N=4, n_c=4 for wild type cells, for mDia1, mDia3 k.o. and mDia1/3 double k.o. N=3, n_c=3. ♦ outliers.

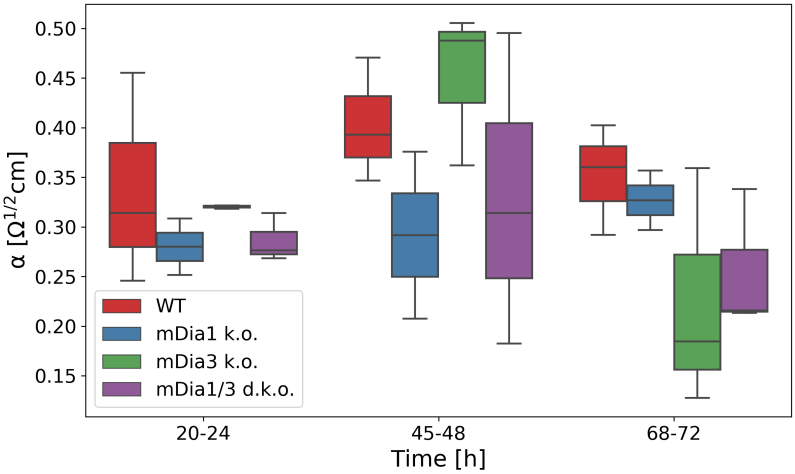

Figure B.7.: α distribution of wild type, mDia1, mDia3 and mDia1/3 double k.o. fibroblasts on 125 µm electrodes over time. With N, the total number of electrodes out of n experiments with n_c different cell cultures: N=4, n_c=4 for wild type cells, for mDia1, mDia3 k.o. and mDia1/3 double k.o. N=3, n_c=3. ♦ outliers.

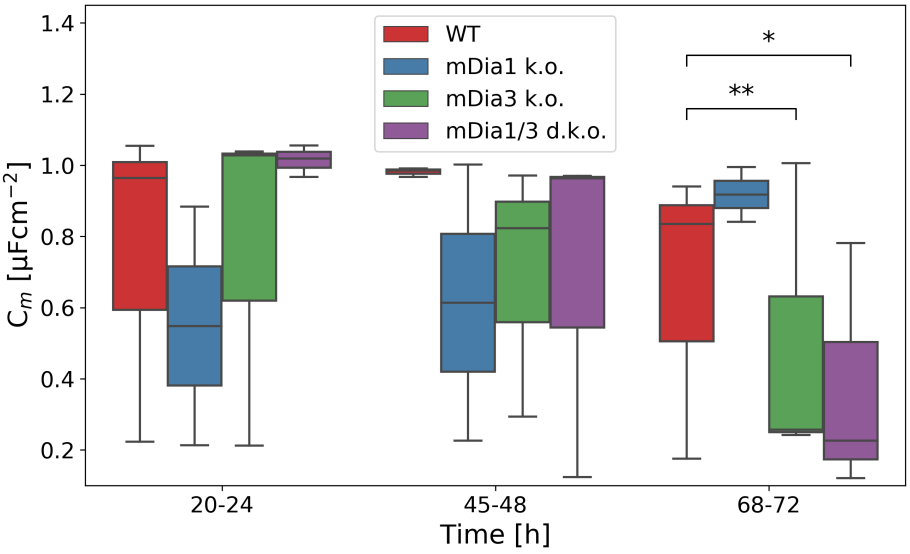

Figure B.8.: C_m distribution of wild type, mDia1, mDia3 and mDia1/3 double k.o. fibroblasts on 125 µm electrodes over time. With N, the total number of electrodes out of n experiments with n_c different cell cultures: N=4, n_c=4 for wild type cells, for mDia1, mDia3 k.o. and mDia1/3 double k.o. N=3, n_c=3. ♦ outliers.

B.3. Mean TGF-β 1 impedance

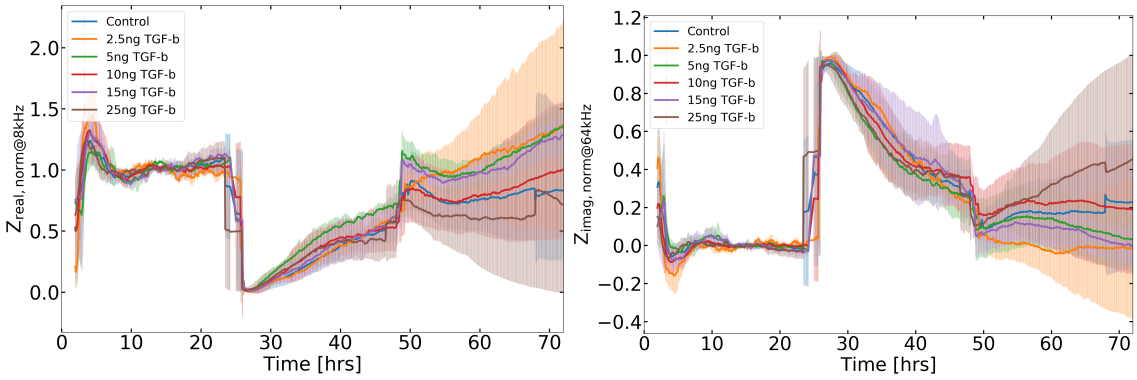

(a) Normalised mean resistance (real part) and standard deviation of measured impedance signals for treatment with additional TGF-β 1.

(b) Normalised mean reactance (real part) and standard deviation of measured impedance signals for treatment with additional TGF-β 1.

Figure B.9.: The mean was taken over N experiments and n_c cultures with N=17, n_c=8 for untreated cells, N=4, N=8, n_c=3 for 10ng, N=4, n_c=2 for 2.5ng, 5ng, 15ng and 25ng.

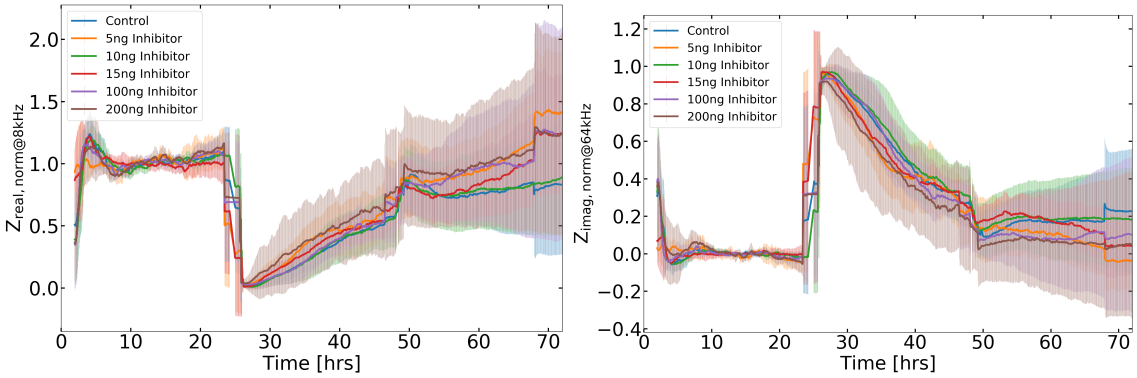

(a) Normalised mean resistance and standard deviation of measured impedance signals for treatment with TGF-β 1 inhibitor.

(b) Normalised mean reactance and standard deviation of measured impedance signals for treatment with TGF-β 1 inhibitor.

Figure B.10.: The mean was taken over N experiments and n_c cultures with N=17, n_c=8 for untreated cells, N=4, N=8, n_c=3 for 5ng, N=4, n_c=2 for 10ng, 15ng, 100ng and 200ng.

C. Significance tables

C.1. Formin k.o. parameters

		Rb	alpha	Cm
		WT	WT	WT
pre	WT	1	1	1
	mDia1 k.o.	0,3165	1	0,638
	mDia3 k.o.	x	x	x
	mDia1/3 d.k.o.	0,1484	0,5564	0,1998
45 h	WT	1	1	1
	mDia1 k.o.	0,4582	0,3329	0,2214
	mDia3 k.o.	x	x	x
	mDia1/3 d.k.o.	0,3333	0,2715	0,4356
72 h	WT	1	1	1
	mDia1 k.o.	0,3333	0,4858	0,3874
	mDia3 k.o.	x	x	x
	mDia1/3 d.k.o.	0,4698	0,5125	0,4138

Table C.1.: Table of p-values from t-test for significance for R_b , α and C_m for formin k.o. cells on 50 µm electrodes.

		Rb	alpha	Cm
		WT	WT	WT
pre	WT	1	1	1
	mDia1 k.o.	0,8869	0,5305	0,3065
	mDia3 k.o.	0,8	0,7	0,6594
	mDia1/3 d.k.o.	0,8383	0,4569	0,9278
45 h	WT	1	1	1
	mDia1 k.o.	0,0521	0,2483	1
	mDia3 k.o.	0,8	0,4507	0,2
	mDia1/3 d.k.o.	0,8	0,4966	0,2458
72 h	WT	1	1	1
	mDia1 k.o.	0,0514	0,6365	0,7769
	mDia3 k.o.	0,7877	0,1718	0,0069
	mDia1/3 d.k.o.	0,1886	0,2	0,0107

Table C.2.: Table of p-values from t-test for significance for R_b , α and C_m for formin k.o. cells on 125 µm electrodes.

		Rb	alpha	Cm
		WT	WT	WT
pre	WT	1	1	1
	mDia1 k.o.	0,5057	6,70E-03	4,23E-02
	mDia3 k.o.	1	6,70E-03	8,20E-03
	mDia1/3 d.k.o.	0,6617	7,50E-03	1,83E-01
45 h	WT	1	1	1
	mDia1 k.o.	0,0141	0,3103	0,0959
	mDia3 k.o.	1,67E-04	9,46E-05	0,007
	mDia1/3 d.k.o.	0,0337	0,4631	0,0511
72 h	WT	1	1	1
	mDia1 k.o.	0,6083	0,2826	0,2094
	mDia3 k.o.	0,0143	0,0714	0,2667
	mDia1/3 d.k.o.	0,148	0,2933	0,042

Table C.3.: Table of p-values from t-test for significance for R_b , α and C_m for formin k.o. cells on 250 µm electrodes.

thalf	recrate	50			
		WT	mDia1	mDia3	mDia1/3
50	WT	1	0,5942	0,4121	0,8246
	mDia1	0,2571	1	0,4452	0,7813
	mDia3	0,3868	0,1291	1	0,4121
	mDia1/3	0,0658	0,9662	0,0754	1

Table C.4.: Table of p-values from t-test for significance for $r_{1/2}$ and $t_{1/2}$ of formin k.o. cells on 50 µm electrodes.

thalf	recrate	125			
		WT	mDia1	mDia3	mDia1/3
125	WT	1	0,0205	0,432	0,2593
	mDia1	0,0175	1	0,0122	0,0544
	mDia3	0,6655	0,0325	1	0,343
	mDia1/3	0,9965	0,6209	0,7248	1

Table C.5.: Table of p-values from t-test for significance for $r_{1/2}$ and $t_{1/2}$ of formin k.o. cells on 125 µm electrodes.

thalf	recrate	250			
		WT	mDia1	mDia3	mDia1/3
250	WT	1	4,18E-06	0,4447	0,7348
	mDia1	0,0346	1	0,0836	1,88E-04
	mDia3	0,0293	0,3704	1	0,6058
	mDia1/3	0,0618	0,065	0,743	1

Table C.6.: Table of p-values from t-test for significance for $r_{1/2}$ and $t_{1/2}$ of formin k.o. cells on 250 µm electrodes.

C.2. TGF-β 1 treated cell parameters

42-45 h	Rb	alpha	Cm
	0	0	0
0	1	1	1
-200	1	0,0134	0,913
-100	0,6349	0,9629	0,4851
-15	0,8636	0,2519	0,3037
-10	0,998	0,9879	0,0519
-5	0,1461	0,3736	0,1419
2,5	0,3972	0,8046	0,4336
5	0,414	0,6519	0,991
10	0,6074	0,7333	0,348
15	0,6664	0,46	0,1789
25	0,0067	0,3492	2,21E-02

Table C.7.: Table of p-values from t-test for significance for R_b , α and C_m for fibroblasts treated with different concentrations of either TGF-β 1 or TGF-β 1 inhibitor 42-45 h after wounding.

68-72 h	Rb	alpha	Cm
	0	0	0
0	1	1	1
-15	0,7614	0,6095	0,6667
-10	0,3406	0,7619	0,759
-5	0,42	1,26E-05	0,2429
5	0,9619	0,8299	0,0538
10	0,3939	0,6693	0,3542
15	0,6846	0,8725	0,7987

Table C.8.: Table of p-values from t-test for significance for R_b , α and C_m for fibroblasts treated with different concentrations of either TGF-β 1 or TGF-β 1 inhibitor 68-72 h after wounding.

Bibliography

[1] Ian A. Darby et al. ?Fibroblasts and myofibroblasts in wound healing? In: *Clinical, Cosmetic and Investigational Dermatology* 7 (2014), pp. 301–311. ISSN: 11787015. DOI: 10.2147/CCID.S50046. URL: http://dx.doi.org/10.2147/CCID.S50046.

[2] Jie Li and Robert S Kirsner. ?Chapter 7 - Wound Healing? In: *Surgery of the Skin*. Ed. by June K Robinson et al. Edinburgh: Mosby, 2005, pp. 97–115. ISBN: 978-0-323-02752-6. DOI: https://doi.org/10.1016/B978-0-323-02752-6.50012-2. URL: http://www.sciencedirect.com/science/article/pii/B9780323027526500122.

[3] T. Schreier, E. Degen, and W. Baschong. ?Fibroblast migration and proliferation during in vitro wound healing? In: *Research in Experimental Medicine* 193.1 (Dec. 1993), pp. 195–205. ISSN: 1433-8580. DOI: 10.1007/BF02576227. URL: https://doi.org/10.1007/BF02576227.

[4] Wei Chen and Nikolaos G. Frangogiannis. ?Fibroblasts in post-infarction inflammation and cardiac repair? In: *Biochimica et Biophysica Acta (BBA) - Molecular Cell Research* 1833.4 (2013). Cardiomyocyte Biology: Cardiac Pathways of Differentiation, Metabolism and Contraction, pp. 945–953. ISSN: 0167-4889. DOI: https://doi.org/10.1016/j.bbamcr.2012.08.023. URL: http://www.sciencedirect.com/science/article/pii/S0167488912002571.

[5] Revathi Ananthakrishnan and Allen Ehrlicher. ?The forces behind cell movement? In: *International Journal of Biological Sciences* 3.5 (2007), pp. 303–317. ISSN: 14492288. DOI: 10.7150/ijbs.3.303.

[6] Christophe Le Clainche and Marie-France Carlier. ?Regulation of Actin Assembly Associated With Protrusion and Adhesion in Cell Migration? In: *Physiological Reviews* 88.2 (2008). PMID: 18391171, pp. 489–513. DOI: 10.1152/physrev.00021.2007. URL: https://doi.org/10.1152/physrev.00021.2007.

[7] *National Center for Biotechnology Information. PubChem Database. TGF-beta, CID=56842206.* https://pubchem.ncbi.nlm.nih.gov/compound/TGF-beta. Accessed: 2020-03-17.

[8] *Protein Data Bank in Europe.* https://www.ebi.ac.uk/pdbe/pdbe-kb/proteins/P01137. Accessed: 2020-04-15.

[9] Klemens Rottner et al. ?Actin assembly mechanisms at a glance? In: (2017). DOI: 10.1242/jcs.206433.

[10] Andrea Ravasio et al. ?Gap geometry dictates epithelial closure efficiency? In: *Nature Communications* 6.1 (2015), p. 7683. DOI: 10.1038/ncomms8683. URL: https://doi.org/10.1038/ncomms8683.

[11] M. Poujade et al. ?Collective migration of an epithelial monolayer in response to a model wound? In: *Proceedings of the National Academy of Sciences of the United States of America* 104.41 (2007), pp. 15988–15993. ISSN: 00278424. DOI: 10.1073/pnas.0705062104.

[12] Anne Stamm et al. ?In vitro wound healing assays â state of the art? In: *BioNanoMaterials* 17.1-2 (2016), pp. 79–87. URL: https://www.degruyter.com/view/journals/biomat/17/1-2/article-p79.xml.

[13] Markus Rimann and Ursula Graf-Hausner. ?Synthetic 3D multicellular systems for drug development? In: *Current Opinion in Biotechnology* 23.5 (2012). Tissue, cell and pathway engineering, pp. 803–809. ISSN: 0958-1669. DOI: https://doi.org/10.1016/j.copbio.2012.01.011. URL: http://www.sciencedirect.com/science/article/pii/S0958166912000237.

[14] Florian Groeber et al. ?Skin tissue engineering â In vivo and in vitro applications? In: *Advanced Drug Delivery Reviews* 63.4 (2011). FROM TISSUE ENGINEERING TO REGENERATIVE MEDICINE - THE POTENTIAL AND THE PITFALLS, pp. 352–366. ISSN: 0169-409X. DOI: https://doi.org/10.1016/j.addr.2011.01.005. URL: http://www.sciencedirect.com/science/article/pii/S0169409X11000093.

[15] Olivier Cochet-Escartin et al. ?Border forces and friction control epithelial closure dynamics? In: *Biophysical Journal* 106.1 (2014), pp. 65–73. ISSN: 00063495. DOI: 10.1016/j.bpj.2013.11.015. arXiv: 1402.5060. URL: http://dx.doi.org/10.1016/j.bpj.2013.11.015.

[16] F. Cavallini and M. Tarantola. ?ECIS based wounding and reorganization of cardiomyocytes and fibroblasts in co-cultures? In: *Progress in Biophysics and Molecular Biology* 144 (2019), pp. 116–127. ISSN: 00796107. DOI: 10.1016/j.pbiomolbio.2018.06.010. URL: https://doi.org/10.1016/j.pbiomolbio.2018.06.010.

[17] *Cell Biolabs, Inc.: Boyden Chamber Assays*. https://www.cellbiolabs.com/boyden-chamber-assays. Accessed: 2020-05-15.

[18] Tadashi Tsujino et al. ?Stromal myofibroblasts predict disease recurrence for colorectal cancer? In: *Clinical Cancer Research* 13.7 (2007), pp. 2082–2090. ISSN: 10780432. DOI: 10.1158/1078-0432.CCR-06-2191.

[19] Vincent Nier et al. ?Tissue fusion over nonadhering surfaces? In: *Proceedings of the National Academy of Sciences of the United States of America* 112.31 (2015), pp. 9546–9551. ISSN: 10916490. DOI: 10.1073/pnas.1501278112.

[20] I. Giaever and C. R. Keese. ?Micromotion of mammalian cells measured electrically? In: *Proceedings of the National Academy of Sciences of the United States of America* 88.17 (1991), pp. 7896–7900. ISSN: 00278424. DOI: 10.1073/pnas.88.17.7896.

[21] Youchun Xu et al. ?A review of impedance measurements of whole cells? In: *Biosensors and Bioelectronics* 77 (2016), pp. 824–836. ISSN: 0956-5663. DOI: https://doi.org/10.1016/j.bios.2015.10.027. URL: http://www.sciencedirect.com/science/article/pii/S0956566315304917.

[22] N. Bonanos et al. ?Applications of Impedance Spectroscopy: Theory, Experiment, and Applications? In: Mar. 2018, pp. 175–478. ISBN: 9781119074083. DOI: 10.1002/9781119381860.ch4.

[23] Pierre O. Bagnaninchi and Nicola Drummond. ?Real-time label-free monitoring of adipose-derived stem cell differentiation with electric cell-substrate impedance sensing? In: *Proceedings of the National Academy of Sciences* 108.16 (2011), pp. 6462–6467. ISSN: 0027-8424. DOI: 10.1073/pnas.1018260108. eprint: https://www.pnas.org/content/108/16/6462.full.pdf. URL: https://www.pnas.org/content/108/16/6462.

[24] Jongin Hong et al. ?Electrical cell-substrate impedance sensing as a non-invasive tool for cancer cell study? In: *Analyst* 136 (2 2011), pp. 237–245. DOI: 10.1039/C0AN00560F. URL: http://dx.doi.org/10.1039/C0AN00560F.

[25] Horst Pick et al. ?Monitoring proliferative activities of hormone-like odorants in human breast cancer cells by gene transcription profiling and electrical impedance spectroscopy? In: *Biosensors and Bioelectronics* 50 (2013), pp. 431–436. ISSN: 0956-5663. DOI: https://doi.org/10.1016/j.bios.2013.06.052. URL: http://www.sciencedirect.com/science/article/pii/S0956566313004491.

[26] L. Otero-González et al. ?Application and validation of an impedance-based real time cell analyzer to measure the toxicity of nanoparticles impacting human bronchial epithelial cells? In: *Environmental Science and Technology* 46.18 (2012). cited By 40, pp. 10271–10278. DOI: 10.1021/es301599f. URL: https://www.scopus.com/inward/record.uri?eid=2-s2.0-84866427377&doi=10.1021%2fes301599f&partnerID=40&md5=b8d76bb99f847792e7f77566c9c03621.

[27] Liju Yang and Rashid Bashir. ?Electrical/electrochemical impedance for rapid detection of foodborne pathogenic bacteria? In: *Biotechnology Advances* 26.2 (2008), pp. 135–150. ISSN: 0734-9750. DOI: https://doi.org/10.1016/j.biotechadv.2007.10.003. URL: http://www.sciencedirect.com/science/article/pii/S0734975007001176.

[28] I Giaever and C R Keese. ?Monitoring fibroblast behavior in tissue culture with an applied electric field? In: *Proceedings of the National Academy of Sciences* 81.12 (1984), pp. 3761–3764. ISSN: 0027-8424. DOI: 10.1073/pnas.81.12.3761. eprint: https://www.pnas.org/content/81/12/3761.full.pdf. URL: https://www.pnas.org/content/81/12/3761.

[29] ?Messung von elektrischen Impedanzen? In: *Elektrische Messtechnik: Analoge, digitale und computergestützte Verfahren*. Berlin, Heidelberg: Springer Berlin Heidelberg, 2007, pp. 219–243. ISBN: 978-3-540-75727-6. DOI: 10.1007/978-3-540-75727-6_9. URL: https://doi.org/10.1007/978-3-540-75727-6_9.

[30] Andreas Janshoff et al. ?Cell Adhesion Monitoring Using Substrate-Integrated Sensors? In: *Journal of Adhesion Science and Technology* 24.13-14 (2010), pp. 2079–2104. DOI: 10.1163/016942410X507939. eprint: https://doi.org/10.1163/016942410X507939. URL: https://doi.org/10.1163/016942410X507939.

[31] Marco Tarantola. **?**Dynamics of epithelial monolayers assessed by acoustic and impedimetric whole cell biosensors**?** In: ().

[32] Emil Warburg. **?**Ueber die Polarisationscapacität des Platins;**?** In: *Annalen der Physik* 311.9 (July 1901), pp. 125–135. DOI: https://doi.org/10.1002/andp.19013110910. URL: https://onlinelibrary.wiley.com/doi/abs/10.1002/andp.19013110910.

[33] Hermann Göhr. **?**Beitrage, Uber Elektrodenprozesse, Elektrochemie Reaktionskinetik, Impedanz**?** In: *Berichte der Bunsen-Gesellschaft* 85.4 (1981), pp. 274–280. DOI: https://doi.org/10.1002/bbpc.19810850405. URL: https://onlinelibrary.wiley.com/doi/abs/10.1002/bbpc.19810850405.

[34] Chun-min Lo and Jack Ferrier. **?**Impedance Sensing**?** In: 57.6 (1998), pp. 6982–6987.

[35] *Polymer Database*. http://www.polymerdatabase.com/polymer. Accessed: 2020-02-15.

[36] Andrew S. Utada et al. **?**Dripping to Jetting Transitions in Coflowing Liquid Streams**?** In: *Phys. Rev. Lett.* 99 (9 Aug. 2007), p. 094502. DOI: 10.1103/PhysRevLett.99.094502. URL: https://link.aps.org/doi/10.1103/PhysRevLett.99.094502.

[37] Wen Li et al. **?**Microfluidic fabrication of microparticles for biomedical applications**?** In: *Chemical Society Reviews* 47.15 (2018), pp. 5646–5683. ISSN: 14604744. DOI: 10.1039/c7cs00263g. URL: http://dx.doi.org/10.1039/C7CS00263G.

[38] George J. Todaro and Howard Green. **?**Quantitative studies of the growth of mouse embryo cells in culture and their development into established lines**?** In: *Journal of Cell Biology* 17.2 (May 1963), pp. 299–313. ISSN: 0021-9525. DOI: 10.1083/jcb.17.2.299. eprint: https://rupress.org/jcb/article-pdf/17/2/299/420282/299.pdf. URL: https://doi.org/10.1083/jcb.17.2.299.

[39] *Applied Biophysics*. https://www.biophysics.com/ztheta.php. Accessed: 2020-02-15.

[40] Julien Petit et al. **?**Vesicles-on-a-chip: A universal microfluidic platform for the assembly of liposomes and polymersomes**?** In: *European Physical Journal E* 39.6 (2016). ISSN: 1292895X. DOI: 10.1140/epje/i2016-16059-8.

[41] Douglas B. Weibel, Willow R. DiLuzio, and George M. Whitesides. *Microfabrication meets microbiology*. Mar. 2007. DOI: 10.1038/nrmicro1616.

[42] *Sigmar Aldrich*. https://www.sigmaaldrich.com/materials-science/polymer-science/nipam-polymers.html. Accessed: 2020-02-17.

[43] *Sigma Aldrich Official Website*. https://www.sigmaaldrich.com/materials-science/polymer-science/nipam-polymers.html. Accessed: 2020-04-15.

[44] Liang Yin Chu et al. **?**Monodisperse thermoresponsive microgels with tunable volume-phase transition kinetics**?** In: *Advanced Functional Materials* 17.17 (2007), pp. 3499–3504. ISSN: 1616301X. DOI: 10.1002/adfm.200700379.

[45] P. H. Mott and C. M. Roland. ?Limits to Poisson's ratio in isotropic materials? In: *Phys. Rev. B* 80 (13 Oct. 2009), p. 132104. DOI: 10.1103/PhysRevB.80.132104. URL: https://link.aps.org/doi/10.1103/PhysRevB.80.132104.

[46] Andrea Alessandrini and Paolo Facci. ?AFM: A versatile tool in biophysics? In: *Measurement Science and Technology* 16.6 (2005). ISSN: 09570233. DOI: 10.1088/0957-0233/16/6/R01.

[47] Massimiliano Galluzzi et al. ?Space-resolved quantitative mechanical measurements of soft and supersoft materials by atomic force microscopy? In: *NPG Asia Materials* 8.11 (2016), e327–e327. ISSN: 1884-4049. DOI: 10.1038/am.2016.170.

[48] Charles R. Keese et al. ?Electrical wound-healing assay for cells in vitro? In: *Proceedings of the National Academy of Sciences of the United States of America* 101.6 (Feb. 2004), pp. 1554–1559. ISSN: 00278424. DOI: 10.1073/pnas.0307588100. URL: www.pnas.orgcgidoi10.1073pnas.0307588100.

[49] David Schneider, Marco Tarantola, and Andreas Janshoff. ?Dynamics of TGF-β induced epithelial-to-mesenchymal transition monitored by Electric Cell-Substrate Impedance Sensing? In: *Biochimica et Biophysica Acta - Molecular Cell Research* 1813.12 (2011), pp. 2099–2107. ISSN: 01674889. DOI: 10.1016/j.bbamcr.2011.07.016.

[50] Masayoshi Tojo et al. ?The ALK-5 inhibitor A-83-01 inhibits Smad signaling and epithelial-to-mesenchymal transition by transforming growth factor-Î²? In: *Cancer Science* 96.11 (2005), pp. 791–800. DOI: 10.1111/j.1349-7006.2005.00103.x. eprint: https://onlinelibrary.wiley.com/doi/pdf/10.1111/j.1349-7006.2005.00103.x. URL: https://onlinelibrary.wiley.com/doi/abs/10.1111/j.1349-7006.2005.00103.x.

[51] Yangyang Jia et al. ?Inhibition of profibrotic signalling enhances the 5-azacytidine-induced reprogramming of fibroblasts into cardiomyocytes? In: *International Journal of Biochemistry and Cell Biology* 122.December 2019 (2020). ISSN: 18785875. DOI: 10.1016/j.biocel.2020.105733.

[52] Bryant L. Doss et al. ?Cell response to substrate rigidity is regulated by active and passive cytoskeletal stress? In: *Proceedings of the National Academy of Sciences of the United States of America* 117.23 (2020), pp. 12817–12825. ISSN: 10916490. DOI: 10.1073/pnas.1917555117.

[53] Francisco Javier Guevara-Pantoja et al. ?Microrheology and electrical conductivity of a dilute pnipam suspension? In: *Rheologica Acta* 53.8 (2014), pp. 159–164. ISSN: 00354511. DOI: 10.1007/s00397-013-0751-1.

[54] Naoki Watanabe et al. ?Cooperation between mDia1 and ROCK in Rho-induced actin reorganization? In: *Nature Cell Biology* 1.3 (1999), pp. 136–143. ISSN: 14657392. DOI: 10.1038/11056. URL: https://pubmed.ncbi.nlm.nih.gov/10559899/.

[55] Michael Lammers et al. **?**Specificity of interactions between mDia isoforms and Rho proteins**?** In: *Journal of Biological Chemistry* 283.50 (Dec. 2008), pp. 35236–35246. ISSN: 00219258. DOI: 10.1074/jbc.M805634200. URL: http://www.jbc.org/.

[56] Christof Litschko et al. **?**Functional integrity of the contractile actin cortex is safeguarded by multiple Diaphanous-related formins**?** In: *Proceedings of the National Academy of Sciences of the United States of America* 116.9 (Feb. 2019), pp. 3594–3603. ISSN: 10916490. DOI: 10.1073/pnas.1821638116. URL: https://www.pnas.org/content/116/9/3594%20https://www.pnas.org/content/116/9/3594.abstract.

[57] Avelino Dos et al. **?**Fibroblasts close a void in free space by a purse-string mechanism**?** In: *bioRxiv* (Aug. 2020), p. 2020.08.15.250811. DOI: 10.1101/2020.08.15.250811. URL: https://doi.org/10.1101/2020.08.15.250811.

[58] Megha Vaman Rao and Ronen Zaidel-Bar. **?**Formin-mediated actin polymerization at cell-cell junctions stabilizes E-cadherin and maintains monolayer integrity during wound repair**?** In: *Molecular Biology of the Cell* 27.18 (Sept. 2016), pp. 2844–2856. ISSN: 19394586. DOI: 10.1091/mbc.E16-06-0429. URL: https://www.molbiolcell.org/doi/abs/10.1091/mbc.E16-06-0429.

[59] J. Rother et al. **?**Crosstalk of cardiomyocytes and fibroblasts in co-cultures**?** In: *Open Biology* 5.6 (June 2015), p. 150038. ISSN: 2046-2441. DOI: 10.1098/rsob.150038. URL: https://royalsocietypublishing.org/doi/10.1098/rsob.150038.

[60] Xiaoyan Sun et al. **?**Topical application of ALK5 inhibitor A-83-01 reduces burn wound contraction in rats by suppressing myofibroblast population**?** In: *Bioscience, Biotechnology, and Biochemistry* 78.11 (Nov. 2014), pp. 1805–1812. ISSN: 0916-8451. DOI: 10.1080/09168451.2014.932666. URL: http://www.tandfonline.com/doi/abs/10.1080/09168451.2014.932666.

[61] Francisca Schultz et al. **?**Cardiomyocyteâmyofibroblast contact dynamism is modulated by connexin-43**?** In: *FASEB Journal* 33.9 (2019), pp. 10453–10468. ISSN: 15306860. DOI: 10.1096/fj.201802740RR.

[62] Susan A. Thompson et al. **?**Mechanical coupling between myofibroblasts and cardiomyocytes slows electric conduction in fibrotic cell monolayers**?** In: *Circulation* 123.19 (May 2011), pp. 2083–2093. ISSN: 00097322. DOI: 10.1161/CIRCULATIONAHA.110.015057. URL: https://www.ahajournals.org/doi/10.1161/CIRCULATIONAHA.110.015057.

[63] Janis Vogt, Ryan Traynor, and Gopal P. Sapkota. **?**The specificities of small molecule inhibitors of the TGFß and BMP pathways**?** In: *Cellular Signalling* 23.11 (2011), pp. 1831–1842. ISSN: 08986568. DOI: 10.1016/j.cellsig.2011.06.019. URL: http://dx.doi.org/10.1016/j.cellsig.2011.06.019.

[64] Teruya Tamaru et al. **?**Synchronization of Circadian Per2 Rhythms and HSF1-BMAL1:CLOCK Interaction in Mouse Fibroblasts after Short-Term Heat Shock Pulse**?** In: *PLoS ONE* 6.9 (Sept. 2011). Ed. by Shin Yamazaki, e24521. ISSN: 1932-6203. DOI: 10.1371/journal.pone.0024521. URL: https://dx.plos.org/10.1371/journal.pone.0024521.

[65] Akira Kitamura and Masataka Kinjo. **?**Determination of diffusion coefficients in live cells using fluorescence recovery after photobleaching with wide-field fluorescence microscopy**?** In: *Biophysics and Physicobiology* 15.0 (2018), pp. 1–7. ISSN: 2189-4779. DOI: 10.2142/biophysico.15.0_1. URL: https://www.jstage.jst.go.jp/article/biophysico/15/0/15%7B%5C_%7D1/%7B%5C_%7Darticle.

[66] Jianfeng Zhou et al. **?**Correlation between dielectric/electric properties and cross-linking/charge density distributions of thermally sensitive spherical PNIPAM microgels**?** In: *Macromolecules* 45.15 (2012), pp. 6158–6167. ISSN: 00249297. DOI: 10.1021/ma300454h.